



POLITECNICO
MILANO 1863

**SCUOLA DI INGEGNERIA INDUSTRIALE
E DELL'INFORMAZIONE**



Thermo-fluid dynamic characterization of an additive manufactured rough channel and development of an experimental PIV apparatus

TESI DI LAUREA MAGISTRALE IN
ENERGY ENGINEERING - INGEGNERIA ENERGETICA

**Carlotta Tamagnini, 220855,
Francesca Agostino, 102674**

Advisor:
Prof. Andrea Lucchini

Co-advisors:
Mats Kinell
Alessio Bonaldo

Academic year:
2023-2024

Abstract: In this thesis the thermal and flow properties of additively manufactured surfaces are examined, with a particular emphasis on surface roughness and how it affects fluid dynamics and heat transfer in cooling channels. The focus of the work is on Laser Powder Bed Fusion methods, which are commonly employed in the manufacturing of complex gas turbine cooling ducts. Although it increases design freedom, elevated surface roughness in these components generates difficulties such as early boundary layer transitions and greater momentum losses that compromise thermal and aerodynamic performance. In order to optimize cooling efficiency in gas turbine applications, this work uses experimental setups that combine infrared thermography and particle image velocimetry to examine how roughness affects heat transfer. As part of Siemens Energy AB's efforts to provide sustainable energy solutions, the results help to improve additive manufacturing procedures and the overall thermal efficiency of land-based gas turbines.

Key-words: Additive Manufacturing, Surface Roughness, Heat Transfer, Fluid Dynamics, Gas Turbines, Infrared Thermography, Particle Image Velocimetry, Nusselt number, Velocity Profile, Boundary Layer

Contents

1	Introduction	5
1.1	Motivation	5
1.2	Literature review	6
2	Theoretical background	9
2.1	Gas Turbines	9
2.2	Turbine cooling methods	10
2.2.1	Turbine blade internal cooling	11
2.2.2	Turbine blade film cooling	11
2.2.3	Thermal barrier coating	12
2.3	Additive manufacturing	12
2.3.1	Laser powder bed fusion	12
2.3.2	Surface roughness parameters	13
2.4	Wall bounded turbulent flows	14
2.4.1	Internal flows	15
2.4.2	Governing equations	15
2.4.3	Turbulent wall-bounded flows	16
2.4.4	Boundary layer theory	18
2.4.5	Pressure gradient	19
2.4.6	Heat transfer	19
2.4.7	Surface roughness effects	20
2.5	Infrared thermography	21
2.6	Particle Image Velocimetry velocity field calculation and correlation theory	22
3	Experimental Set-Up	25
3.1	Surface Roughness Heat Transfer rig	25
3.1.1	Working principle	25
3.1.2	Measurement devices	26
3.1.3	Analogue rough surface	28
3.1.4	Post processing	30
3.2	Particle Image Velocimetry rig	32
3.2.1	Working principle	32
3.2.2	Measurement devices	33
3.2.3	Post processing	36
4	Uncertainty analysis	37
4.1	Introduction to uncertainty analysis	37
4.2	Uncertainty results for the Surface Roughness Heat Transfer rig	38
4.2.1	Smooth surfaces uncertainty analysis	38
4.2.2	Rough surfaces uncertainty analysis	39
4.3	Uncertainty results for the Particle Image Velocimetry rig	42
5	Results	45
5.1	Surface Roughness Heat Transfer rig	45
5.1.1	Smooth surfaces	45
5.1.2	Validation of the rig	46
5.1.3	Rough surfaces	48
5.1.4	Comparison of the three rough surfaces	49
5.1.5	Modification of the Surface Roughness Heat Transfer rig	52
5.2	PIV rig	52
5.2.1	Cross-correlation coefficient	52
5.2.2	Turbulence intensity	53
5.2.3	Velocity profile at the center-line	54
5.2.4	Honeycomb solution	57
5.2.5	Reynolds stresses	61
5.2.6	Boundary layer velocity profile	62
5.2.7	Rough plates Particle Image Velocimetry tests	63
5.2.8	Modification of the test section	65

6	Conclusions and Future Works	65
7	Bibliography and citations	66
8	List of symbols	70
8.1	Latin symbols	70
8.2	Abbreviation	74
8.3	Greek symbols	75

List of Figures

1	Heat transfer curves for different pipes[1]	6
2	Comparisons of heat-transfer and friction coefficients vs. Reynolds number for $Pr = 1.20$ [2].	7
3	Comparisons of heat-transfer and friction coefficients vs. Reynolds number for $Pr = 5.94$ [2].	7
4	Main components of a gas turbine (SGT-800) [3]	9
5	Joule-Brayton cycle	9
6	Rotor Turbine Inlet Temperature. [4]	10
7	Variation of turbine inlet temperature during 1950-2010. [5]	10
8	Typical cooled aircraft gas turbine blade. [6]	11
9	AM process flow chart	12
10	Schematic representation of the printing process [7]	13
11	Surfaces with different wavelengths but the same amplitude. (a) and (b) Surface Forms; (c) and (d) Waviness; (e) and (f) Roughness. [8]	13
12	Schematic representation of some parameters [8]	14
13	Different roughness profile and their amplitude distribution curve along with (a) skewness and (b) Kurtosis ranges [8]	14
14	Laminar, hydrodynamic boundary layer development in a circular tube. [9]	15
15	Turbulent boundary layer division.	17
16	Velocity profile of a wall-bounded fully turbulent flow.	17
17	Friction factor for variable relative roughness circular tubes. [9]	20
18	Difference between equivalent sand-grain roughness and randomly distributed roughness [8]	20
19	Roughness regimes classification [8]	21
20	Electromagnetic spectrum	22
21	Comparison of blackbody and real surface emission [9]	22
22	Particle Image Velocimetry system scheme	23
23	Particle velocity disparity against surrounding fluid velocity	23
24	Image windowing and discrete cross-correlation map.	24
25	Sub-pixel interpolation of correlation peak.	24
26	Correlation map evaluation by Fourier transform.	25
27	Process flow diagram	25
28	IR camera	26
29	Heater	27
30	Heater controller	27
31	Three-way valve	27
32	Top plate	28
33	SRHT rig set-up with flow direction	28
34	Inconel939	30
35	Aluminium1	30
36	Aluminium2	30
37	CAD model of the up-scaled analog AM roughness plate	30
38	Captured frame.	30
39	ROI mask.	30
40	Variation in time of the mainflow temperature.	31
41	Variation in time of the wall temperature.	31
42	Laterally averaged Nu and globally averaged Nu comparison.	32
43	Nusselt plot in the ROI.	32
44	Scheme of the PIV measurement system	32
45	Light sheet formation optics.	32
46	Test section adapter version 1.	34
47	Test section test-bed version 1.	34

48	Chronos 2.1 sensor specifications.	34
49	High-speed camera Chronos 2.1-HD.	34
50	Nano PIV Laser Head Internal Components	35
51	Scheme of the Arduino connections.	36
52	Some samples of the velocity vector map files that were produced in MATLAB as a result of the OpenPIV analysis: (a) raw, (b) filtered, and (c) interpolated, in that order. Interpolated vectors are colored green, whereas outlier velocity vectors are colored red.[10]	36
53	OpenPIV preprocessed image with high-pass filter and background image subtraction.	37
54	OpenPIV post-processed image using FFT algorithm.	37
55	Flowchart of the uncertainty contributions	38
56	SEM image of the internal section of the Aluminium cooling channel.	40
57	Profilometer Mitutoyo Surftest SJ-410.	40
58	Measurements for each of the surface roughness parameters and average results.	40
59	Measured spheres diameters	41
60	Normal PDF for upscaled diameters	41
61	QQ plot Normal PDF	41
62	Cumulative density function	41
63	Statistical properties used to obtain the rough surface	41
64	Schematics of the primary PIV measurement chain elements and the most important sources of uncertainty.	42
65	Scheme of MI calculation [11].	43
66	Examples of good measurement (a) and outlier (b) for the half peak diameter criteria [11].	44
67	Histogram of uncertainty values obtained with RPC method.	44
68	Uncertainty values curve.	44
69	Contour plot over smooth surfaces	45
70	Laterally averaged Nusselt number along the streamwise coordinate	46
71	Fully developed flow correlation	47
72	Normalized values along the streamwise dimensionless coordinate	47
73	Local Nusselt distribution for different Reynolds number.	48
74	Laterally averaged Nusselt for all the tested flow conditions for the Aluminium2 rough surface model.	49
75	Three surfaces comparison for all the tested Reynolds.	50
76	Nusselt enhancement in the fully developed flow comparison for Reynolds 20000.	50
77	Nusselt enhancement in the fully developed flow comparison for Reynolds 10000.	51
78	Variation of the dimensionless mean velocity profile of the turbulent boundary layer with the logarithmic distance from the wall.	51
79	Roughness density classification.	52
80	NX model for the new rig	52
81	Honeycomb for the SRHT rig	52
82	Cross correlation coefficient in the center position.	53
83	Turbulence intensity of measurement cases.	54
84	Velocity profile test 4 compared to the modified power law	55
85	Velocity profile test 5 compared to the modified power law	55
86	Velocity profile test 9 compared to the modified power law	55
87	Velocity profile test 10 compared to the modified power law	55
88	Maximum Velocity displacement from the center-line	56
89	4th order polynomial function of the difference of the position of the maximum velocity and the center-line velocity and residual plot	56
90	Honeycomb design for PIV system.	58
91	Turbulence intensity downstream of am honeycomb varying the Reynolds numbers [12].	58
92	Honeycomb hexagonal structure geometry [13].	58
93	Pressure loss coefficient for different honeycomb designs [14].	59
94	Average velocity profile after the honeycomb installation.	60
95	Position displacement of the maximum velocity profile comparison.	60
96	Reynolds stresses comparison with DNS data at $Re_\tau = 180$	61
97	Reynolds stresses comparison with DNS data at $Re_\tau = 587$	61
98	Log law comparison between theoretical and experimental curve for test 1.	62
99	Error curve for Clauser Chart method log law results for test 1.	62
100	Log law comparison between theoretical and experimental curve for test 2.	63
101	Error curve for Clauser Chart method log law results for test 2.	63
102	Camera field of view of the rough plates tests IN939.	63

103	Velocity profiles in different distances from the rough plates.	63
104	Mean velocity profile of test 5 on rough plates.	64
105	Nu enhancement IN939 Re=20000 window 9.	65
106	New test section design.	65

List of Tables

1	Definition of the surface roughness parameters in the ISO 4287:1997 standard	14
2	IR camera technical parameters	26
3	Thermocouple technical parameters	27
4	Comparison of real and analogue surface roughness parameters.	29
5	Thermal properties of Accura Xtreme grey material at different temperatures.	29
6	PDF properties for paint and IRW	39
7	Uncertainty results for Reynolds 10000 and 15000	39
8	Uncertainty results for Reynolds 20000 and 25000	39
9	Roughness parameters of the real-size rough surface	39
10	Error, mean and standard deviation for the measured Roughness Parameters	41
11	Values of uncertainty for parallel measurements on smooth plates.	44
12	Values of uncertainty for perpendicular measurements on smooth plates.	45
13	Comparison between globally averaged Nusselt and Gnielinski correlation	47
14	Surface roughness parameters for different materials in the up-scaled configuration	49
15	Test parameters in the center position	53
16	Cross Correlation Coefficient Statistics	53
17	Turbulence Intensity Statistics	54
18	Quality of the polynomial function of the displacement	55
19	Honeycomb characteristics.	58
20	Test Index and Corresponding smallest lateral wavelength values.	59
21	Expected pressure drops due to the honeycomb structure.	60
22	Experimental Data after the honeycomb installation.	60
23	Experimental parameters of boundary layer tests.	62
24	Comparison of Shear Velocities calculated with moody diagram and Clauser-Chart method.	62
25	Experimental Data with rough plates with distance from plates.	63
26	sand-grain equivalent roughness constant and roughness reynolds number results.	64

1. Introduction

1.1. Motivation

One of the main problems facing humanity today is climate change, as a result of rising global energy production from non-renewable sources and annual increases in energy consumption that led to higher emissions of greenhouse gases. Fossil fuels continue to dominate the world's energy production, despite attempts to promote and develop renewable energy alternatives. According to projections by the International Energy Agency (IEA), the demand for energy is expected to double by 2030 due to factors such as population growth and the ongoing energy transition that affects energy-consuming industries. It is essential to switch from fossil fuels to sustainable energy sources in order to reduce carbon emissions and reach the Net Zero goal by 2050, but it is well known that problems will arise because of their unreliability and sporadic availability. Gas turbines are a very convenient way to produce energy because of their many benefits, such as their compact size, dependability, versatility, and low labor needs for continuous operation. Siemens Energy AB aims to increase turbine efficiency while lowering energy consumption by using alternative renewable fuels. Land-Based Gas Turbines (LBGT) have become an important part of the energy supply: they can be used to satisfy peak electricity demand or deliver a steady supply of power for baseload needs, among other uses. Over the last ten years, there has been a notable improvement in the performance of Industrial Gas Turbines (IGT). This may be attribute to the development of novel coatings, superior materials, and high-level cooling designs, which have increased thermal efficiency significantly. Since the efficiency is largely dependent on the Turbine Inlet Temperature (TIT), the development of more intricate cooling duct designs, made feasible by Additive Manufacturing (AM), has raised the TIT threshold and, consequently, the efficiency itself. While AM offers design flexibility and the potential to produce completely integrated products reducing the number of components, it also has drawbacks, including inferior mechanical properties and higher pressure drops due to early boundary layer transition, increased

momentum losses, and flow separation. Specifically for the Laser Powder Bed Fusion (L-PBF) process internal cooling channels and aerodynamic performance are impacted by the elevated Surface Roughness (SR). Although momentum transfer and friction factor associated to rough surfaces have been studied in Computational Fluid Dynamics (CFD), the impact that the SR could have on Heat Transfer (HT) has not been fully understood yet, which has prompted additional research in this area. This thesis focuses on additively manufactured surfaces to understand what happens locally and how the flow and the rough parts interact thermally.

1.2. Literature review

The fundamental understanding of fluid mechanics and the investigation of the factors which influences the pressure drops in pipe networks began with the contribute of Lewis F. Moody [15] whose work presents a comprehensive analysis of friction factors in pipe flow. The creation of the Moody Chart, a graphic representation of the Darcy-Weisbach friction factor [16] used to compute pressure loss in pipes, is Moody's most significant contribution. The chart makes pipe flow analysis easier by enabling engineers and researchers to easily compute the friction factor for a specific flow state, roughness, and Reynolds number. The Darcy-Weisbach friction factor was calculated thanks to Darcy's experimental study [16] conducted on a flow device with a porous material through which a fluid was flowing at a controlled flow rate. Darcy's studies established the groundwork for comprehending flow resistance and the factors that impact it. The formulation of a empirical correlation was achievable thanks to the work of Colebrook and White [17]. Their research aimed to provide a method for calculating the Darcy-Weisbach friction factor in rough pipes under turbulent regime. In order to assess the convective HT data and create correlations, a dimensionless parameter, the Nusselt number [18], was proposed to quantify the convective HT coefficient in fluid flow. The first studies on how to develop a relationship between friction factor and HT were performed by Churchill and Bernstein [19]. The aim of the experiment was to estimate the Nusselt as a correlation of Reynolds Number and Prandtl number. The study examined the intricate HT properties connected to flow across cylindrical surfaces, with the goal of providing scientists and engineers a useful tool for forecasting convective HT in such situations. Advancements in knowledge of the basic principles driving friction and heat transfer in turbulent flows with irregular physical characteristics were the objectives of Petukhov's research [20]. In "New Equations for Heat and Mass Transfer in Turbulent Pipe and Channel Flow" [21] Gnielinski presents new improved correlations and models to advance the understanding of convective heat and mass transfer by considering the turbulence effects, fluid properties and geometric factors. The equations were developed considering measurement results for large Reynolds and high Prandtl numbers to compute heat and mass transfer coefficients in pipes and channels through which flow occurs, including both the transition region and the region of fully developed turbulent flow. The proposed equation, which is based on extensive data analysis from numerous literature sources, is able to predict about 90% of over 800 experimental outcomes with variances of $\pm 20\%$. Many experiments focused on artificially roughened surfaces were conducted to investigate the behavior of the flow in such conditions. The work of Nikuradse [22] was fundamental to measure the resistance encountered by a turbulent fluid passing through a rough pipe. He investigated the connection between surface roughness and pressure loss using different sized sand grains. Thanks to his study, roughness regimes are now categorized according to dimensionless characteristic roughness.

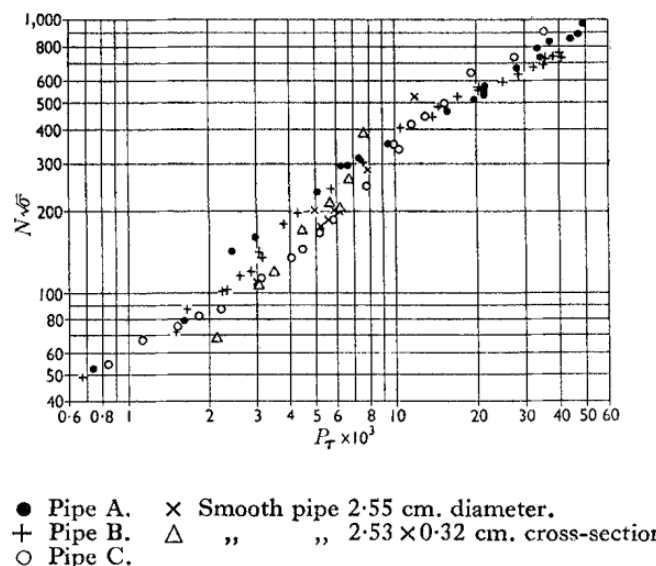


Figure 1: Heat transfer curves for different pipes[1]

Important insights into the onset of totally turbulent flow and the transition to turbulence in rough pipes were provided by Nikuradse's investigations. His research advanced our knowledge of how surface roughness affects the resistance and flow structure in the turbulent boundary layer. In the paper "The Friction and Heat Transmission Coefficients of Rough Pipes" by W. F. Cope [1], the results shown that roughness had no influence on heat transfer under totally turbulent conditions, but that roughness might greatly enhance the heat transfer coefficient compared to a smooth pipe in the transition region between laminar and fully turbulent flow. The internal surfaces of the three pipes tested were intentionally roughened using a unique knurling technique which resulted in approximate roughness ratios (pipe radius/pyramid height) of 8/1, 15/1, and 45/1. Water was the working fluid, and the Reynolds number varied from 2,000 to 60,000. The heat transfer curves and the Peclet number are compared in the Figure 1. The heat transfer coefficient at the upper end of the tested range is similar for all three pipes to the value found for a smooth pipe at the same Peclet number, but the friction coefficient is roughly six times higher. A rough pipe is just half as efficient as a smooth pipe for the same pressure drop. At the lower end of the range, the three pipes' respective roughness and heat transfer coefficients are in the same order. Even when the roughening parts are made of the same (high) thermal conductivity material as the pipe, the experiments demonstrate that the effect of surface roughness of the kind tested is positively adverse to the efficiency of a pipe as a medium for heat transfer. The work of D. F. Dipprey and Rolf Heinrich Sabersky [2] investigates the heat and momentum transfer in smooth and rough tubes. The heat-transfer coefficients (C_H) and friction coefficients (C_F) were measured using electrically heated tubes filled with distilled water.

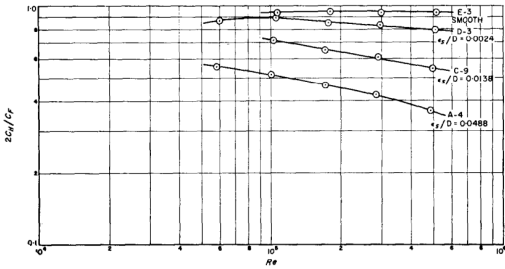


Figure 2: Comparisons of heat-transfer and friction coefficients vs. Reynolds number for $Pr = 1.20$ [2].

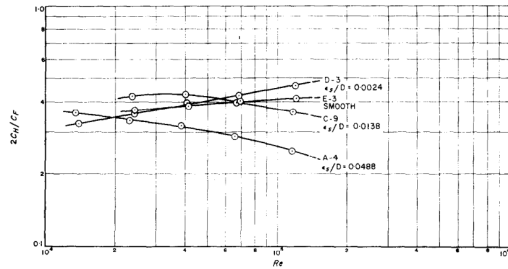


Figure 3: Comparisons of heat-transfer and friction coefficients vs. Reynolds number for $Pr = 5.94$ [2].

From the Figures 2 and 3 it is evident that C_H rises with increasing roughness values and, in turn, with larger friction coefficients at any given Re and Pr . When examining the curves' shapes at a given Pr , it can be observed the general trend for C_H to grow with Re at the transition region, which is the area where the friction coefficient behaves differently from what would be expected of a fully rough tube compared to a smooth tube. This area reaches a maximum close to the beginning of the totally harsh behavior. Unlike the friction coefficient, the heat-transfer coefficient drops monotonically in the hydraulically fully rough zone. The investigations focused on the enhancement of thermal performances due to artificial roughness in nuclear reactors. Mario Dalle Donne and Leonhard Meyer [23] performed their experiments testing a single rod contained in smooth tubes. The heat-transfer surface of this artificial roughness is composed of two-dimensional rectangular ribs spaced at regular intervals that serve as turbulence promoters, breaking up the viscous sublayer in the fluid region closest to the wall. The results show that both the heat-transfer and friction losses increase, but the thermal performance Sti/f_R , where f_R is the friction factor and St is a dimensionless number proportional to the heat-transfer coefficient, is typically greater for a rough surface than for a smooth one. Beyond only prototypes, AM opens up new possibilities for producing extremely effective industrial components. In this regard, an interesting study has been done by Rastan et al. [24] using both experimental and numerical methods to investigate the HT parameters of minichannel-based heat exchangers that contain longitudinal vortex generators. In addition to a smooth channel for comparison, improved prototypes with various vortex generator designs were created and tested as part of the research. The outcomes shown that vortex generators may greatly enhance convective HT, suggesting that minichannel heat exchangers could be improved using AM. Clemenson et al. [25] examined the effects of ice building on HT on an airfoil and assess HT on a simulated rough surface. In order to reproduce and scale up the surface, the ice's roughness patterns were analyzed in relation to the direction of airflow, and important characteristics were identified [26]. Using the Flack and Schultz correlation [27], the equivalent sand-grain was predicted by comparing the real and analogue surfaces. Hanson [28] used a similar strategy to produce an upgraded model of a cooling tube made via AM, and found out increased HT across the rough surface parts by analysis performed using an Infrared Camera (IR). This study focuses on how additively manufactured component roughness patterns affect HT and pressure losses. Through the creation and analysis of scaled roughness geometries, it offers a comprehensive understanding of the flow-field inside the

rough channel, highlighting that the analogue rough surface must be representative of the statistical properties of the real one. Kadivar et al. [8] provided an essential summary of turbulent flow over additively manufactured rough surfaces that includes an exhaustive understanding of flow behavior and CFD data are provided. Even if several studies have been made regarding HT on cooling channels, they mostly focus on nuclear reactors, while the scarcity of existing literature on the behavior of local HT regarding upscaled surface roughness emphasizes the necessity of more study in this field. One drawback of the IR approach is that it cannot provide information on the flow's velocity distribution or the patterns of the flow particles over the whole channel. In the field of fluid dynamics study, new techniques have been created, like PIV, which provides quantitative data regarding the velocity distribution in a fluid flow. This information is useful for studying complicated flow patterns, turbulence, boundary layers, and other phenomena in fluid dynamics. Particle image velocimetry (PIV) is an optical technique for visualizing flow and it is used to measure a fluid's instantaneous velocity and other relevant parameters. In the paper "Multi-point optical measurements of simultaneous vectors in unsteady flow—a review" [29], Adrian states that these non-intrusive techniques yield spatial data similar to that obtained by flow visualization, with an accuracy that is comparable to single-point techniques like hot wire and laser Doppler velocimetry. Particle Image Velocimetry (PIV) is being employed more and more to instantaneously examine unstable velocity fields. The extensive research conducted by Kompenhans J. et al. [30] stated how the PIV technique enables the recording of a comprehensive velocity field in a flow plane in a matter of microseconds. Both high speed flows ($U = 600m/s$) and very low speed flows ($U = 1$) have been effectively handled by this technology. It offers information on unstable flow fields that is challenging to find using conventional experimental methods. In the wind tunnel, it also helps to reduce operating time. Furthermore, PIV is a useful experimental instrument that offers high-resolution experimental data to validate numerical predictions of flow fields, allowing computational and experimental scientists to work closely together. High spatial resolution, high image density, and the use of small tracer particles that can accurately follow the flow are essential conditions for employing PIV in aerodynamics. Although it takes an extensive amount of time, the original PIV image analysis approach produces accurate results with a high spatial resolution. The major issue when using PIV is to analyze a large number of photos in order to explore the dynamics of coherent structures in turbulent flows. Westerweel J. [31] developed a digital implementation of the PIV method which results in a significant reduction in processing time but a little loss in measurement precision. This offers a workable method for processing a lot of PIV photos. Numerous research works concentrated on applying the PIV technique to wind tunnels in order to study the flow in less turbulent wind tunnels [32] and to apply it to larger wind tunnels [33]. An experimental PIV configuration that can function in transonic flows in the harsh environment (noise, vibrations) of a large high-speed wind tunnel has been created at DLR [34]. Application of this PIV-system to flow field measurements in the velocity range of $U = 10 - 500m/s$ has proven successful. In a blow-down wind tunnel, two distinct aerodynamic studies of instantaneous transonic flow fields around a bluff cylinder and around a NACA 0012 airfoil were conducted. Hinsch et al. [35] conducted several implementations of the PIV approach, including basic relations for the scenario where the velocity is not constant within the zone of inquiry. The analysis demonstrates that statistical properties of the flow can be easily obtained using large-field questioning. There is no need for numerous laborious small-area interrogations because the autocorrelation function will replicate the velocity's probability density function. Moreover, velocity variations impact on regular fringe analysis are explored. The local flow field and particle motion have a complex relationship. Particle size, size distribution, shape, and density all affect this connection. The characteristics of the scattering particles must be known by the researcher in order to quantify the uncertainty of the velocimeter observations of the flow field. Hunter et al. [36] tried to manage the particle characteristics and confirm those qualities at the measurement spot in order to get the best velocimeter measurements. The researcher also tried to manipulate the location and concentration of particles in the flow field in order to maximize measurement efficiency. A particle diameter of $1\mu m$ or less has been employed for seeding in gas flows in every scenario in the study "Tracer particles and seeding for particle image velocimetry" [37]. Due to the small particle size, a high laser pulse energy—typically $100mJ$ or more is required. Ceramic materials with a high refractive index, such Al_2O_3 , TiO_2 , and ZrO_2 , are preferred for starting fires and high-temperature flows. However, dispersing them in a gas flow can be challenging, just like with other powders. One proposed recording method for particle image velocimetry in wind tunnels is a high-speed digital camera that utilizes video technology. In the paper "Digital video camera for application of particle image velocimetry in high-speed flows" [38] the camera has two independently triggerable interline CCD sensors installed on two faces of a cube beam splitter. The camera can be programmed to trigger immediately off a pulsed laser with a repetition rate that is different from the typical 25 Hz CCIR video frame rate thanks to the asynchronous reset feature. The camera digitizes and stores captured images in RAM, which may be accessed by a computer via its parallel interface. The subsequent processing of photographic PIV recordings has been the object of several discussions. Numerous techniques are employed to determine the flow velocity starting from the capture of particle pictures [39]. One of these is the cross-correlation approach, a popular PIV methodology that calculates particle displacement by comparing particle pictures from successive frames. Measuring the flow velocity requires monitoring the change in particle locations. This technique is the core of OpenPIV [40], an open-source MATLAB software that uses a cross-correlation algorithm to correlate two

consecutive PIV images and produce a displacement vector map. The deformation of particle image patterns by strong velocity gradients and out-of-pattern motions is a major source of error for the PIV technique [41]. The academic community is beginning to adopt imagine deformation methods in particle image velocimetry, however certain aspects have not been adequately studied, neither theoretically nor with the use of simulations. This kind of algorithm's primary stage is the reconstruction of the distorted images, which calls for the application of an interpolation technique. Astarita and Cardone's [42] investigation aims to investigate this aspect's impact on the PIV algorithm's uncertainty. The findings of the performance evaluation, which was carried out with synthetic images, indicate that the interpolation method employed in the reconstruction of the deformed images has a significant impact on both the systematic and total errors. The aim of our study work is to employ the PIV technique to examine flow patterns and HT performance. In literature there are many examples of flow investigations such us Son and Kihm's [43] paper where in a two-pass square channel with a smooth wall and a 90° rib-roughened wall PIV tests have been conducted to investigate the relationship between the high-Reynolds number turbulent flow and wall HT characteristics. For an average Reynolds number (Re) of 30000, detailed averaged velocity distributions and turbulent kinetic energy are provided for both the main and secondary flows. The HT experimental data of Ekkad and Han [44] were compared with the PIV measurement results. As the result demonstrates, the flow impingement, not the flow turbulence level, is the main component responsible for the augmentation of the two-pass square channel HT. The wall HT increases for both smooth and ribbed wall two-pass square channels are directly associated with the properties of the secondary flow, such as the vortex's form, strength, rotating direction, and locations. Because of the increased local flow impingement close to the rib, the rib-induced flow turbulence increases the HT. The notion of combining PIV and IR to analyze heat transfer in fluidized beds was first forth by Tsuji et al. [45]. Process engineering research has widely employed infrared thermography for HT measurements and analyses. Through the application of this technology, it is possible to simultaneously analyze, without interfering with the flow field, the velocity and temperature of individual particles as well as their relationships with the distinctive flow structures created in fluidized beds. The PIV technology can be employed for the investigation of boundary layer behaviour in roughened surfaces as it is shown in the paper "PIV measurements of turbulent boundary layer over a rod-roughened wall" [46]. PIV measurements were used to examine how surface roughness affects a turbulent boundary layer (TBL). Based on the momentum thickness, the Reynolds number was around $Re_\theta = 1000 - 1500$. Two-dimensional spanwise rods organized regularly were the roughness elements employed; the roughness height to boundary layer thickness ratio was $k_s/\delta = 0.025$. In the area of $y < 4 - 5k_s$, where k_s is the effective sand roughness height, the introduction of the roughness elements increased turbulent stresses. The effects of surface roughness on the turbulence structure in the roughness sublayer were investigated and compared with the results of earlier direct numerical simulations (DNS) utilizing PIV data. The PIV-obtained iso-contours of the mean velocity and Reynolds stress in the roughness sublayer shown excellent agreement with the DNS results.

2. Theoretical background

2.1. Gas Turbines

Industrial gas turbines are thermal turbomachines with power outputs ranging from a few kilowatts to 200-300 MW.

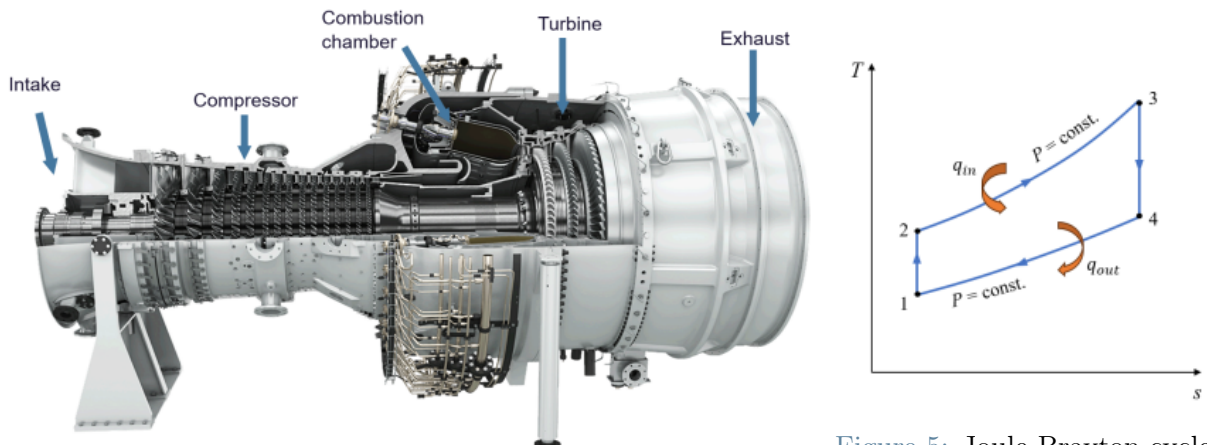


Figure 5: Joule-Brayton cycle

Figure 4: Main components of a gas turbine (SGT-800) [3]

Gas turbines typically operate with air as the working fluid, which flows constantly through the unit. Furthermore they are well known for their reliability, availability, and versatility over a variety of power generation ranges among other power generation methods. As shown in Figure 4, the compressor, combustion chamber, and turbine are the essential parts of a GT. The working fluid's temperature and pressure are raised by the turbocompressor as it passes through the intake. The additional fuel is then burned in the combustion chamber to provide heat, raising the temperature significantly. Power generation stems from the expansion of the hot working fluid in the turbine. Exhaust gases are either released into the atmosphere or used to generate steam or heat in Combined Cycle Power Plants. As seen in Figure 5, the ideal Joule-Brayton cycle, which consists of four sub-processes, can simplify the thermodynamic process inside a GT. A gas turbine's thermodynamic cycle is open since the machine's working fluid is not circulated. In actual gas turbine applications, the compressor can be driven by the expansion work, and the remaining work can be used to generate electricity. This is frequently made possible by adding of a second power turbine to provide rotational speed flexibility. Assumptions include a greater air mass flow than fuel mass flow, calorically and thermally perfect gas, components operating at 100% efficiency, and equal pressure ratios for the turbine and compressor.

$$\eta_{th} = 1 - \left(\frac{T_4}{T_3} \right) = 1 - \left(\frac{P_2}{P_1} \right)^{(\gamma-1)/\gamma}. \quad (1)$$

The efficiency of the cycle is positively correlated with increasing TIT, while the pressure ratio has a significant early positive impact before progressively declining. Thus, the objective of this work is to highlight the importance of the rise in heat transfer made possible by AM techniques, which opens the prospect of reaching higher and higher TIT, optimizing the whole cycle and providing improvements in the cooling of the initial stages turbine blades.

2.2. Turbine cooling methods

Gas turbines are employed in industrial settings, land-based power generation, and aviation propulsion. As turbine rotor inlet temperatures (RIT) rise, gas turbines' thermal efficiency and power production proportionally rise. The Figure 6 provides an illustration of this by plotting particular core power generation (which is associated with specific thrust) against turbine RIT. The ideal performance line, which represents a cycle power output with 100% efficient turbines with no leakage or cooling flows, is generally very close to where aircraft engines travel. Increasing RIT is definitely one of the essential technologies for improving the performance of gas turbine engines. Turbine blades require cooling because, as Figure 1.2 demonstrates, the RIT in modern gas turbines is significantly greater than the softening point of the blade material. The RIT should rise from the current 2500°F to 3500°F maintaining the same volume of cooling air (3%–5% of compressor bleed air) in order to double the engine output in aircraft gas turbines. The compressor pressure ratio should rise from its current level of 20 times the compression ratio to 40 times the ratio, or possibly higher. This implies that with the same volume of hotter cooling air from high-pressure compressor bleed, future aviation gas turbines would have a greater turbine inlet temperature.

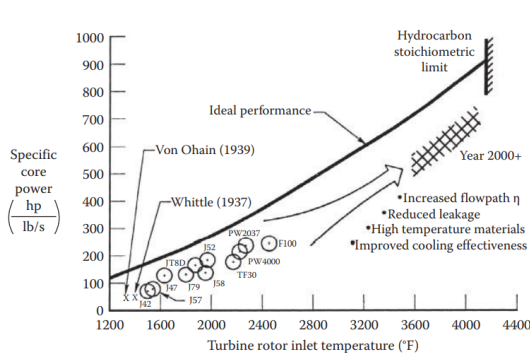


Figure 6: Rotor Turbine Inlet Temperature. [4]

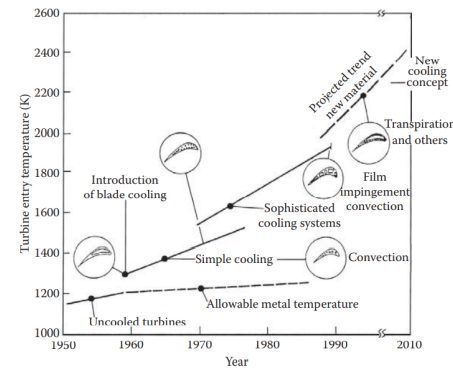


Figure 7: Variation of turbine inlet temperature during 1950-2010. [5]

Due to the limitation of the NO_x pollution, the RIT should maintain the current level of 1371.1°C–1426.7°C [47] for land-based gas turbines, including power generation (300MW combined cycles), marine propulsion, and industrial uses such as pumping and cogeneration (less than 30MW). Thus, the primary concern for land-based gas turbines is how to increase thermal efficiency even further at the current RIT level. For example, how to raise the efficiency of the large gas turbine combined cycle from today's 55% to 60% and the stand-alone gas turbine

from today's 35% to 40%. Heat is transferred to the turbine blades at a rate that increases with the turbine input temperature. In order to satisfy suitable durability requirements, the amount of fluctuation in temperature and level within the blade material, which creates thermal stresses, must be controlled. The operating temperatures are significantly higher than the metal's allowable temperature. As a result, cooling the blades is necessary for safe operation. Air extracted from the engine's compressor cools the blades. The thermal efficiency is penalized by this extraction, therefore the cooling method, operating environment, and turbine blade shape must all be evaluated and optimized. Blades of gas turbines are cooled both externally and internally. For the life span of the design, the engine cooling system must be built to guarantee that the maximum blade thermal stress and temperature gradients at which the blades can be exposed while in operation are compatible with one another. Higher blade temperatures and shorter component life are the results of insufficient coolant flow. In the same manner, excessive coolant flow lowers engine performance. In order to maximize the full benefits of the high inlet gas temperature, the engine cooling system must be designed to reduce the need for compressor bleed air. Advanced gas turbine engines use advanced cooling methods such as augmented convective cooling, film cooling, and impingement cooling.

2.2.1 Turbine blade internal cooling

First stage vanes are typically cooled using a simple, very effective method that involves jet impinging on the inner surfaces of the airfoil through microscopic holes in the impingement insert. A portion of the expended air passes through rows of distributed film holes at the precise points where film-cooling surface protection is required. The rest of the waste air travels in the direction of the trailing-edge region and escapes through small holes to allow cooling of the trailing-edge zone. Because cooling air may be guided to impinge on the heated area, impingement cooling is incredibly effective. The impingement cooling effect, however, can be reduced by a spent-air cross-flow effect. The cooling principles of a contemporary multipass turbine rotor blade are illustrated in Figure 8. Currently, due to space constraints and structural integration, the blade trailing-edge region uses short pins, whereas the blade midchord region uses serpentine coolant channels with rib turbulators on the inner walls of the rotor blades. The flow and temperature profiles in the rotor coolant channels, as well as the distributions of their surface heat-transfer coefficients, can be changed by both rotational buoyancy forces and Coriolis forces. Determining the local heat transfer distributions under normal engine cooling flow, coolant-to-blade temperature difference (buoyancy effect), and rotating conditions in the rotor coolant passageways with impingement cooling, rib-turbulated cooling, or pinned cooling is crucial. Finding out about the related coolant passage pressure losses for a particular internal cooling system is also essential. This can assist in the design of an effective cooling system and prevent the rotor blade from overheating in a localized hot zone.

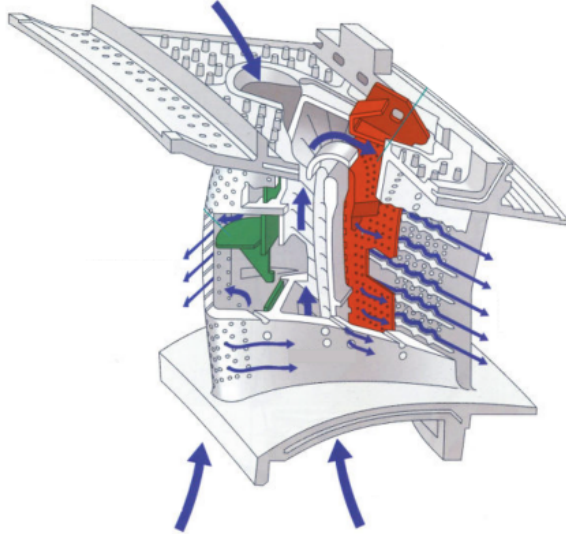


Figure 8: Typical cooled aircraft gas turbine blade. [6]

2.2.2 Turbine blade film cooling

By injecting cooling air to the boundary layer above the blade surface, turbine film cooling efficiently reduces the temperature of the gas that heats the surface. By creating a shield, this cooling air keeps the blade from absorbing too much heat. The temperature ratio (T_c/T_g), coolant-to-hot-mainstream pressure ratio (p_c/p_t), and the position, structure, and distribution of film cooling holes on a film-cooled airfoil are among the primary

factors of film cooling. While the coolant-to-mainstream temperature ratio and the coolant-to-mainstream density ratio can be correlated, the coolant-to-mainstream pressure ratio can be related to the coolant-to-mainstream mass flux ratio (blowing ratio). Since the temperature (T_c/T_g) and pressure (p_c/p_t) ratios effectively indicate the ratio of the coolant-to-hot-mainstream thermal capacitance, they are likely the most helpful metrics for assessing the efficacy of film cooling. In general, at a specific temperature ratio, the better the film-cooling protection (i.e., lower heat transfer to the airfoil) the higher the pressure ratio, while the better the film-cooling protection the lower temperature ratio at a set pressure ratio. However, jet penetration into the mainstream (jet liftoff from the surface) may result in a reduction of the film-cooling protection if the pressure ratio is sufficiently high (i.e., excessive blowing). Therefore, it's critical to maximize coolant flow for airfoil film cooling under engine operating conditions (Reynolds number 10^6 ; Mach number around 0.9 upon exit). Understanding the impact of unstable wakes and free-stream turbulence on the heat-transfer coefficient distributions and film-cooling effectiveness of airfoils is also significant.

2.2.3 Thermal barrier coating

Single crystal blades with TBC coating and directionally solidified blades have been suggested as advanced casting procedures for higher RIT. TBC coating improves turbine efficiency by insulating the turbine airfoils and enabling a 93.33°C – 148.89°C higher RIT. Two categories of coating methods exist:

1. Using air plasma spray with plate structure/porosity/low thermal conductivity;
2. electron beam physical vapor deposition with column structure/dense/high thermal conductivity.

The coating thickness and previously discussed coating procedures determine the performance of TBC coatings, the zirconia-based ceramics.

2.3. Additive manufacturing

Additive manufacturing (AM) is a transforming manufacturing method that turns 3D CAD models into physical products. The process, outlined in Figure 9, starts with the production of the CAD model, which is subsequently transformed into an STL file that contains surface geometry information that has been broken up into triangles. The model is then divided into thin layers, each measuring between $20\ \mu\text{m}$ and $1\ \text{mm}$ in thickness. The details of each layer, such as its thickness and resolution, are then fed into a printing device. Afterwards, the component is assembled layer by layer by using a heat source, like a laser, to melt or sinter the material locally. The component is usually surface treated once the repetitive buildup process is finished, before it is put to use, because of the AM induced surface roughness.

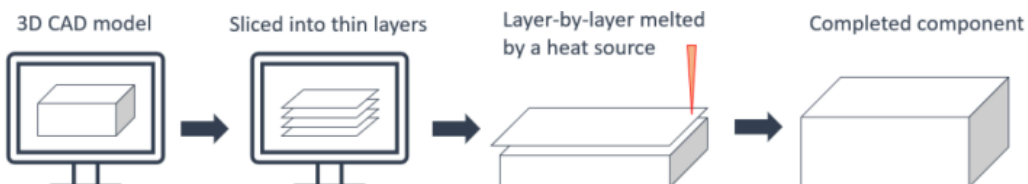


Figure 9: AM process flow chart

This technique requires the usage of material in the form of powder, wire, or liquid droplets, as well as a machine capable of creating cross-section layers, all of which are controlled by a complex system. AM's adaptability has gained widespread attention in a variety of industries, including automotive, aerospace, medical, sports, and construction. While traditional manufacturing processes such as forging and machining remain important, AM has opened up new possibilities, particularly in the field of land-based gas turbines. Notably, AM allows for the fabrication of sophisticated designs for internal turbine blade cooling, which improves overall cycle efficiency, reduces fuel consumption, and increases power generating capacity. A wide range of AM technologies are available, each adapted to a specific application, with a key distinction between polymer-based and metal-based AM processes. But because Laser Powder Bed Fusion (L-PBF) is so important to the production of gas turbine components and turbine blades, it is going to be presented here in detail.

2.3.1 Laser powder bed fusion

Laser Powder Bed Fusion (L-PBF) (Figure 10) is the most widely used manufacturing process in the production of GT components, including turbine blades. First, a 3D CAD model is created. After the steps described above, this method then uses a powdered material, which is deposited onto a substrate plate or an already-processed layer. The powdered particles are then precisely melted using the focused energy of a powerful laser beam that

follows the outlines of the layer that is now in place. Once a layer of powder has been applied, the base plate is carefully lowered. This process is continued layer by layer until the entire item is constructed. Once the printing is complete, there is some detailed clean-up work to be done, such as smoothing out the surface and eliminating any superfluous supports. The key advantages of L-PBF over other metal 3D printing techniques are its ability to create supports from the powder itself, its compatibility with a wide range of materials, and its generally lower cost. However, there are several drawbacks, such as the strength of the parts, size limitations, long print times, and the surface polish may not be as smooth as desired. This overview provides a thorough analysis of the significant role that L-PBF plays in manufacturing today, but it also highlights areas for improvement in order to address those weaknesses.

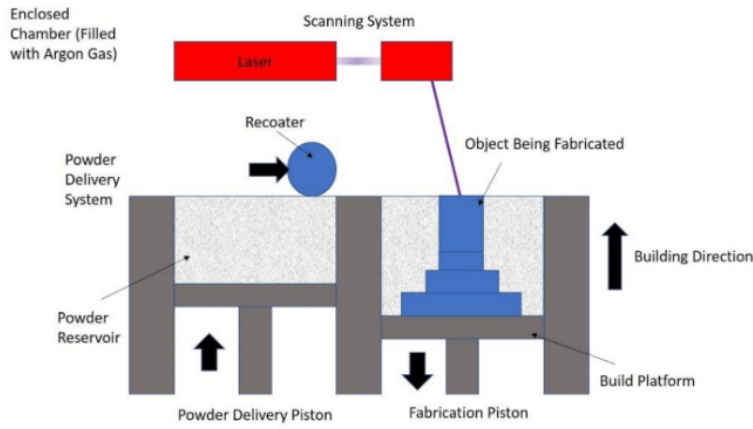


Figure 10: Schematic representation of the printing process [7]

2.3.2 Surface roughness parameters

When it comes to additive manufacturing, printed products usually have a significant degree of roughness (11). But also due to natural geometric imperfections, even the smoothest surfaces have some roughness to them. The frequency of these imperfections might change, indicating the type of surface roughness. Low frequency differences are referred to as "*Waviness*", and high frequency variations as "*Roughness*". "*Surface form*" refers to the rare geometric errors that have a major effect on the contour of the object. In addition to being a qualitative characteristic, surface roughness can be precisely measured using the parameters found in the ISO 4287:1997 standard, reported in Table 1 and Figure 12 shows a more detailed explanation.

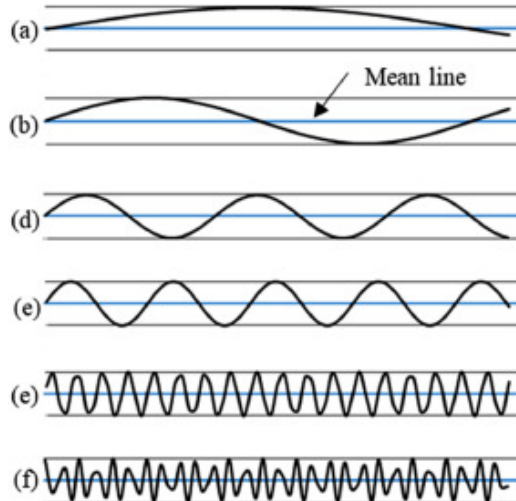


Figure 11: Surfaces with different wavelengths but the same amplitude. (a) and (b) Surface Forms; (c) and (d) Waviness; (e) and (f) Roughness. [8]

The most interesting of these are skewness (R_{sk}) and kurtosis (R_{ku}), of which the physical meaning is represented in Figure 13. Skewness indicates whether peaks or valleys predominate in the surface profile by capturing the asymmetry in the height distribution. Peaks predominate on a surface indicated by a positive R_{sk} value; valleys

Parameter	Description
$R_a = \frac{1}{l_r} \int_0^{l_r} z(x) dx$	Arithmetic average of profile height deviation from the mean line
$R_q = \sqrt{\frac{1}{l_r} \int_0^{l_r} z(x)^2 dx}$	Root-mean-square roughness
$R_p = \sum_{i=1}^5 \frac{m_{n_i}(z(x))}{5}$	Maximum peak height above the mean line, within a single sampling length
$R_v = \sum_{i=1}^5 \frac{m_{n_i}(z(x))}{5}$	Maximum valley depth under the mean line, within a single sampling length
$R_z = \sum_{i=1}^5 \frac{R_{p_i} + R_{v_i}}{5}$	Average of the five maximum peak to valley height of the profile
$R_{sk} = \frac{1}{R_q^3} \left[\frac{1}{l_r} \int_0^{l_r} Z(x)^3 dx \right]$	Skewness
$R_{ku} = \frac{1}{R_q^4} \left[\frac{1}{l_r} \int_0^{l_r} Z(x)^4 dx \right]$	Kurtosis

Table 1: Definition of the surface roughness parameters in the ISO 4287:1997 standard

are more common on a negative value. Conversely, kurtosis quantifies the height distribution's sharpness, with a Gaussian distribution benchmarked at R_{ku} equals 3. The frequency of steep peaks or flatter regions is indicated by values above or below 3.

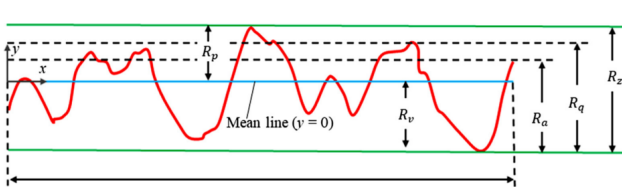


Figure 12: Schematic representation of some parameters [8]

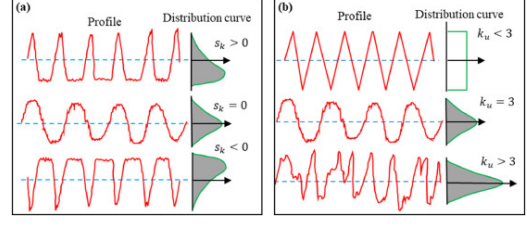


Figure 13: Different roughness profile and their amplitude distribution curve along with (a) skewness and (b) Kurtosis ranges [8]

In contrast to traditional surface roughness, AM topographies exhibit significant variation based on processing parameters and material selections, requiring an extensive range of parameters for precise surface roughness measurement and comparison. These factors are essential for comprehending how surface textures affect heat transport and fluid dynamics, and they go beyond just describing the surface. Differences in other roughness factors like R_q , R_{sk} , and R_{ku} can cause surfaces with the same R_a to have a different thermal and fluid dynamic behavior.

2.4. Wall bounded turbulent flows

Our research focuses on wall-bounded flows, an extensive group that encompasses drag reduction and boundary layer formation. We consider a steady state continuous incompressible fluid flow as mathematical model so we can state that:

$$\rho = \text{constant} \quad (2)$$

The model accounts for the non-slip condition, the fluid's constant chemical composition, and the absence of power generation within the volume. The velocity of the internal, monophase fluid flow is low. We can ignore viscosity dissipation since the enthalpy changes brought on by the wall presence have a greater influence. Solid boundaries have a major impact on the flow behavior in turbomachinery, resulting in phenomena including boundary layer separation, the development of secondary flows, and the creation of intricate three-dimensional flow structures. It is crucial to comprehend and manage these wall-bounded flows in order to maximize aerodynamic efficiency, reduce losses, and raise turbomachinery's overall efficiency. Furthermore, the study of wall-bounded flows is essential for the design and operation of efficient systems because the interaction between the wall-bounded flows and the rotating blades or vanes in turbomachinery directly affects variables like aerodynamic loading, flow stability, and the occurrence of phenomena like boundary layer transition and

turbulence.

2.4.1 Internal flows

We focus our attention on forced convection challenges at low speeds where the fluid does not undergo phase transition for the time being. Furthermore, we won't take into account any possible effects on the fluid's micro- or nanoscale. When forced convection occurs, buoyant forces from temperature differences in the fluid do not sustain the relative motion between the fluid and the surface; instead, external devices like fans or pumps do it. Internal flow requires analysis of more than just the flow's laminar or turbulent characteristics; entrance and fully developed areas must also be taken into account. Analyze a laminar flow in a circular tube with radius r_o , where fluid flows into the tube at a constant speed. We know that viscous effects become significant and a boundary layer forms with increasing x when the fluid comes in contact with the surface. Close to the expense of a shrinking inviscid flow area, this development results in boundary layer merging near the center line. After this merging, the velocity profile no longer varies with increasing x and viscous effects are present throughout the whole cross section. When this criterion is met, the flow is considered to be completely developed; this distance from the entrance is known as the hydrodynamic entry length, or $x_{fd,h}$. For laminar flow in a circular tube, the fully developed velocity profile is parabolic, as Figure 14 displays, instead due to radial turbulent mixing, the profile of turbulent flow is flatter.

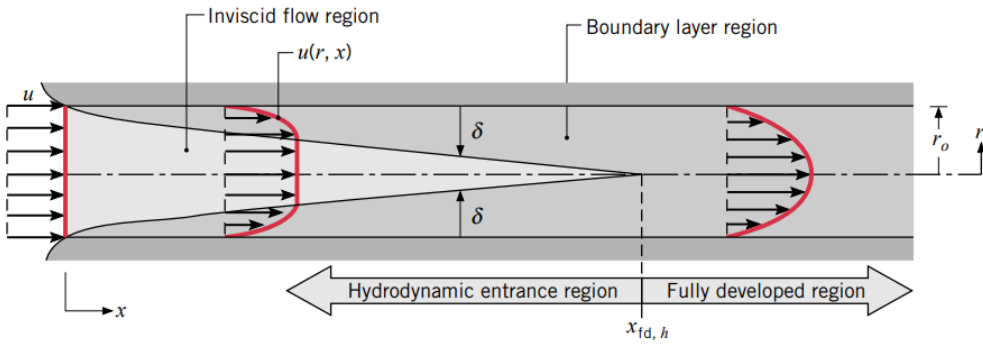


Figure 14: Laminar, hydrodynamic boundary layer development in a circular tube. [9]

The extent of the entry region must be evaluated when dealing with internal flows, since this depends on whether the flow is turbulent or laminar. The definition of the Reynolds number for flow in a circular tube is:

$$Re = \frac{u_m D}{\nu} \quad (3)$$

where u_m is the mean fluid velocity over the tube cross section and D is the tube diameter. The critical Reynolds number in a fully developed flow that marks the beginning of turbulence is 2300. In the entrance region's developing boundary layer, turbulence is most likely starting to develop. The equation 4 can be used to determine the hydrodynamic entrance length for laminar flow ($Re_D \leq 2300$). The entry length in turbulent flow requires an adequate general formulation; however, we do know that, as a first approximation, it is roughly independent of Reynolds number so we shall assume fully developed turbulent flow for $(x/D) > 10$.

$$\left(\frac{x_{fd,h}}{D} \right)_{lam} \approx 0.05 Re_D \quad (4)$$

2.4.2 Governing equations

In case of incompressible single phase fluid with constant thermal properties and considering gravity as the only body force we can state that no tangential tension is acting. There is simply the normal stress, or pressure $-p\delta_{ij}$, which is sustained by molecular collisions and has thermodynamic origins. δ_{ij} is defined as the Kronecker δ . The viscous stress shown by τ_{ij} is a result of the relative motion on a continuum and depends on velocity gradients.

$$\sigma_{ij} = -p\delta_{ij} + \tau_{ij} \quad (5)$$

For Newtonian fluids as the case examined the dependency of the the viscous stress and the velocity gradients are linear as shown in the equation 6, where v_i and v_j are the velocity components.

$$\sigma_{ij} = -p\delta_{ij} + \mu \left(\frac{\partial v_i}{\partial x_j} + \frac{\partial v_j}{\partial x_i} \right) \quad (6)$$

The value μ is the dynamic viscosity and is constant for Newtonian fluids. The relation between the velocity and the temperature is given by the Fourier's Law:

$$q = -k\nabla T \quad (7)$$

The last constitutive equation of a Newtonian fluid is the bond of the temperature with the internal energy is shown in the Equation 8.

$$du = c_v dT \quad (8)$$

A collection of basic partial differential equations, known as the Navier-Stokes equations, are derived from the three laws of conservation of mass, momentum, and energy. The Navier-Stokes equations for incompressible flow have the following main form:

$$\frac{\partial v_1}{\partial z_1} + \frac{\partial v_2}{\partial z_2} = 0 \quad (9)$$

$$v_1 \frac{\partial v_1}{\partial z_1} + v_2 \frac{\partial v_1}{\partial z_2} = \nu \left[\frac{\partial^2 v_1}{\partial^2 z_1} + \frac{\partial^2 v_1}{\partial^2 z_2} \right] + g_1 - \frac{1}{\rho} \frac{\partial P}{\partial z_1} \quad (10)$$

$$v_1 \frac{\partial v_2}{\partial z_1} + v_2 \frac{\partial v_2}{\partial z_2} = \nu \left[\frac{\partial^2 v_2}{\partial^2 z_1} + \frac{\partial^2 v_2}{\partial^2 z_2} \right] + g_2 - \frac{1}{\rho} \frac{\partial P}{\partial z_2} \quad (11)$$

$$v_1 \frac{\partial T}{\partial z_1} + v_2 \frac{\partial T}{\partial z_2} = \alpha \left[\frac{\partial^2 T}{\partial^2 z_1} + \frac{\partial^2 T}{\partial^2 z_2} \right] + \frac{\mu}{\rho c_p} \phi + \frac{G}{\rho c_p} \quad (12)$$

2.4.3 Turbulent wall-bounded flows

Our research focuses on both laminar and turbulent internal flows, in this section we will address the latter. From now we call the three components of the velocities u , v and w for convenience. It is not possible to describe the motion of every fluid particle efficiently due to the random character of a turbulent flow. Rather, in equation 13 properties have been simplified down into a constant mean value and a fluctuating component:

$$\begin{aligned} v &= \bar{v} + v' \\ u &= \bar{u} + u' \\ w &= \bar{w} + w' \\ p &= \bar{p} + p' \\ \theta &= \bar{\theta} + \theta' \end{aligned} \quad (13)$$

Thanks to this operations we can model the turbulent flow using the Reynolds- averaged Navier Stokes(RANS) equations. The RANS equations are a system of partial differential equations employed to describe time-averaged flow of a fluid. Since the RANS equations cannot directly resolve the entire range of turbulent scales, turbulence models are employed to simulate the effects of turbulence on the mean flow field. The continuity equation is shown in the equation 14.

$$\frac{\partial \bar{\rho}}{\partial t} + \operatorname{div}(\bar{\rho} \tilde{\mathbf{U}}) = 0 \quad (14)$$

The Reynolds equations are shown below:

$$\frac{\partial(\bar{\rho}\tilde{U})}{\partial t} + \operatorname{div}(\bar{\rho}\tilde{U}\tilde{\mathbf{U}}) = -\frac{\partial \bar{P}}{\partial x} + \operatorname{div}(\mu \operatorname{grad} \tilde{U}) + \left[-\frac{\partial(\bar{\rho}u'^2)}{\partial x} - \frac{\partial(\bar{\rho}u'v')}{\partial y} - \frac{\partial(\bar{\rho}u'w')}{\partial z} \right] + S_{Mx} \quad (15)$$

$$\frac{\partial(\bar{\rho}\tilde{V})}{\partial t} + \operatorname{div}(\bar{\rho}\tilde{V}\tilde{\mathbf{U}}) = -\frac{\partial \bar{P}}{\partial y} + \operatorname{div}(\mu \operatorname{grad} \tilde{V}) + \left[-\frac{\partial(\bar{\rho}u'v')}{\partial x} - \frac{\partial(\bar{\rho}v'^2)}{\partial y} - \frac{\partial(\bar{\rho}v'w')}{\partial z} \right] + S_{My}w \quad (16)$$

$$\frac{\partial(\bar{\rho}\tilde{W})}{\partial t} + \operatorname{div}(\bar{\rho}\tilde{W}\tilde{\mathbf{U}}) = -\frac{\partial \bar{P}}{\partial z} + \operatorname{div}(\mu \operatorname{grad} \tilde{W}) + \left[-\frac{\partial(\bar{\rho}u'w')}{\partial x} - \frac{\partial(\bar{\rho}v'w')}{\partial y} - \frac{\partial(\bar{\rho}w'^2)}{\partial z} \right] + S_{Mz} \quad (17)$$

The scalar transport equation is described by the equation18:

$$\frac{\partial(\bar{\rho}\tilde{\Phi})}{\partial t} + \operatorname{div}(\bar{\rho}\tilde{\Phi}\tilde{\mathbf{U}}) = \operatorname{div}\left(\Gamma_\Phi \operatorname{grad} \tilde{\Phi}\right) + \left[-\frac{\partial(\bar{\rho}u'\varphi')}{\partial x} - \frac{\partial(\bar{\rho}v'\varphi')}{\partial y} - \frac{\partial(\bar{\rho}w'\varphi')}{\partial z}\right] + S_\Phi \quad (18)$$

where the overbar indicates a time-averaged variable and the \sim indicates a density-weighted or Favre-averaged variable. For free stream turbulent flows large velocity fluctuations in these flows are confined to thin zones. Formally speaking, the rates of change of flow variables in the flow's (x)direction are minor in comparison to the rates of change in the flow's cross-stream (y)direction ($\partial\varphi/\partial x \ll \partial\varphi/\partial y$). Additionally, the region where changes occur always has a smaller cross-stream width (δ) in the flow direction ($\delta/L \approx 1$) than any length scale L . We examine the features of a few basic two-dimensional incompressible turbulent flows with constant applied pressure.

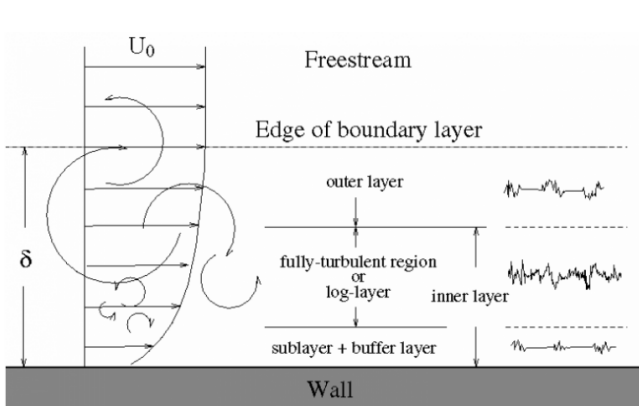


Figure 15: Turbulent boundary layer division.

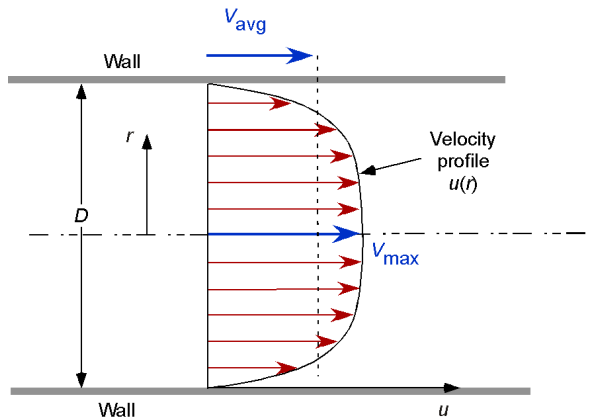


Figure 16: Velocity profile of a wall-bounded fully turbulent flow.

Many of these turbulent flows have been observed experimentally to demonstrate that, at a given distance, the precise type of the flow source has little effect on the flow's structure. It seems that the flow's turbulence is solely controlled by the surrounding environment. Similar to the mean velocity, the turbulence structure likewise achieves a self-preserving condition, but at a greater distance from the flow source. We will subsequently examine the properties of turbulent flows close to solid walls. The solid boundary causes a significant difference in the turbulent structure and flow behavior compared to unconstrained turbulent flows. Correlating the experimental data has been made easier with the help of dimensional analysis. Re_L , the Reynolds number depending on the length scale L in the flow direction (or pipe radius) in turbulent thin shear layer flows, is usually quite big. This suggests that, at these scales, inertial forces are much stronger than viscous forces. There is typically a tiny layer where viscous effects are significant and a large region of inertia-dominated flow far from the wall in flows along solid boundaries. The flow is affected by viscous effects and is independent of free stream parameters close to the wall. The distance y from the wall, the fluid density ρ and viscosity μ , and the wall shear stress τ_w are the only factors that affect the mean flow velocity. When compared to laminar flow, the velocity profile across a pipe or channel in turbulent flow has unique properties. A more consistent fluid velocity across the cross-section is shown by the profile's general flat part near the pipe's center. The improved mixing and momentum transfer that are features of turbulent flow are what cause this homogeneity. The velocity falls off quickly as it approaches the pipe walls, maintaining the no-slip condition where the fluid velocity is zero at the boundary. This sharp decrease in velocity in close proximity of the walls is caused by the turbulent flow's unpredictable and chaotic behavior. The velocity profile in laminar-type flows in pipes has been analytically found to follow a parabolic function. On the other hand, the typical experimentally fitted velocity profile for turbulent-type flows has the form provided by Equation 19.

$$\frac{u}{u_{\max}} = \left[1 - \left(\frac{r}{D}\right)^m\right]^{\frac{1}{n}} \quad (19)$$

in which n and m are exponents that allow the generated profile to coincide with the profiles found through experimentation. The exponent n correlates with Re and in the case of laminar flows is equal to 1.0 with $m=2$. Turbulent fluctuations always have a three-dimensional spatial behavior, even in flows where the mean velocities and pressures change in only one or two space dimensions. Moreover, rotational flow structures with a range of length scales—known as turbulent eddies—are visible in turbulent flow visualizations. During vortex

stretching, angular momentum is preserved and large eddies are effectively inviscid. As a result, their cross-sectional radius decrease and their rotation rate rises. As a consequence, the process produces motions at both shorter time-based and transverse length scales. The energy that keeps the turbulence flowing is generated during these occurrences by the stretching work that the mean flow performs on the large eddies. Smaller eddies are more weakly stretched by the mean flow and more strongly stretched by larger eddies. This process, known as the "energy cascade," transfers kinetic energy from large eddies to successively smaller and smaller eddies. The scales at which the strength of the viscous and inertia effects is equal are the smallest scales in a turbulent flow. These scales are known as the Kolmogorov microscales, and at these scales, work occurs in opposition to viscous stresses, resulting in the dissipation and conversion of small-scale eddy motion energy into internal energy. More energy is lost as a result of this dissipation in turbulent flows. Strong mixing is produced when vortical eddy movements are present. Fluid is transported across the boundaries of the control volume by erratic currents connected to eddies passing close to the boundaries. Although mass cannot be created or destroyed by these recirculating fluid motions, the fluid parcels carried by the eddies will move momentum and energy in and out of the control volume. Variations with a negative y -velocity will typically bring fluid parcels with a higher x -momentum into the control volume across its top boundary and transport control volume fluid to a region of slower moving fluid across its bottom boundary due to the existence of the velocity gradient. Similar to this, fluid moving more slowly will generally be transported into areas of higher velocity by positive y -velocity variations. Convective transport by the eddies results in a net result of momentum exchange, which accelerates the slower-moving fluid layers and decelerates the faster-moving layers. As a result, additional turbulent shear stresses—also referred to as Reynolds stresses—are experienced by the fluid layers. In RANS momentum equations we can identify 2 types of stresses named as Reynolds stresses:

normal stresses

$$\tau_{xx} = -\rho \overline{u'^2} \quad \tau_{yy} = -\rho \overline{v'^2} \quad \tau_{zz} = -\rho \overline{w'^2} \quad (20)$$

and shear stresses

$$\tau_{xy} = \tau_{yx} = -\rho \overline{u'v'} \quad \tau_{xz} = \tau_{zx} = -\rho \overline{u'w'} \quad \tau_{yz} = \tau_{zy} = -\rho \overline{v'w'} \quad (21)$$

2.4.4 Boundary layer theory

The turbulent flow close to the wall will be examined in this section. If it is estimate the Reynolds number ($Re_y = Uy/\nu$) employing a distance y from the wall as a basis, we can observe that inertia forces predominate in the flow far from the wall if y is of the order of L . However, a Reynolds number based on y will likewise decline to zero as y is reduced to zero. There will exist a range of values of y for which Re_y is of order one, just prior to y reaching zero. The viscous forces will be at least as great as the inertia forces at this distance and closer to the wall. When it is close to the wall the mean flow velocity depends entirely on the wall shear stress τ_w , fluid density ρ , viscosity μ , and distance y from the wall. The law of the wall shown in the equation 22 is derived from dimensional analysis.

$$u^+ = \frac{U}{u_\tau} = f \left(\frac{\rho u_\tau y}{\mu} \right) = f(y^+) \quad (22)$$

where u^+ and y^+ are dimensionless parameters calculated using the friction velocity:

$$u_\tau = \sqrt{\frac{\tau_w}{\rho}} \quad (23)$$

the fluid layer adjacent to the wall is known as the linear or viscous sub-layer where the fluid is stationary at the solid surface. Additionally, extremely near to the wall, turbulent eddies motions must stop, and viscous factors dominate the behavior of the fluid closest to the wall. Because of the extreme thinness of this viscous sub-layer ($y^+ < 5$), we can presume that the shear stress is roughly constant and equal to the wall shear stress τ_w across the layer. Between velocity and distance from the wall there is a the linear correlation:

$$u^+ = y^+ \quad (24)$$

The Buffer sub-layer($5 < y^+ < 30$) is the intermediate layer where the velocity profile transitions from linear to logarithmic and no clear law can be observed.

It can be assumed that the turbulent kinematic viscosity, v_t may be stated as a product of a turbulent length scale ℓ and a turbulent velocity scale θ on dimensional scale. It is possible to relate the distinctive velocity scale of the eddies with the mean flow features because there is a substantial correlation between the mean flow and the behavior of the greatest eddies. This has proven to be effective in basic two-dimensional turbulent flows where $\partial U / \partial y$ is the only significant mean velocity gradient and $\tau_{xy} = \tau_{yx}$ is the only relevant Reynolds stress. The following equation can be stated about Prandtl's mixing length model:

$$v_t = \ell_m^2 \left| \frac{\partial U}{\partial y} \right| \quad (25)$$

where a new length scale, ℓ_m , is used. The turbulence structure is sufficiently simple for a significant class of simple turbulent flows, such as wall boundary layers and free turbulent flows, to be described by basic algebraic formulas. It exists a region outside the viscous sublayer ($30 < y^+ < 500$), called log-law layer, where both turbulent and viscous effects are significant. The shear stress is believed to be constant and equal to the wall shear stress within this inner region, and it varies slowly with distance from the wall. With one more assumption on the length scale of turbulence (mixing length $\ell_m = \kappa y$ according to Prandtl's mixing length model), we can obtain a dimensionally valid functional link between u^+ and y^+ :

$$u^+ = \frac{1}{\kappa} \ln(y^+) + B \quad (26)$$

The equation 26 is the log law and the values for the constants are found from measurements. In case of smooth walls von Karman's constant $\kappa \approx 0.4$ and the additive constant $B \approx 5.5$. However, wall roughness causes a decrease in the value of B.

2.4.5 Pressure gradient

In the context of internal flow systems, properly measuring the pressure drop along a specific pipe length is critical and this is even more significant in turbine cooling channels. One measure that is frequently used to assess the pressure drop in these kinds of systems is the Darcy friction factor [9].

$$f = \frac{\Delta p D}{L \rho u_m^2 / 2} \quad (27)$$

Calculating the friction factor for fully developed laminar flow is simple because it reduces to a constant value. The calculation is more difficult in fully developed turbulent flow, though, because it depends on the Re and the relative surface roughness. This dependency results from the various hydraulic regimes in turbulent flow. Viscous forces predominate in laminar flow, and surface characteristics have little effect on pressure losses. Turbulent flow, on the other hand, behaves differently between rough and smooth hydraulic pipes. In turbulent flow, a laminar sub-layer is present close to the wall. Surface deviations in hydraulically smooth pipes are completely encapsulated by this sub-layer, which keeps them out of the turbulent layer. On the other hand, surface irregularities in hydraulically rough pipes cause the turbulent layer to get disturbed by penetrating the laminar sub-layer. The Colebrook-White equation is the most well-known of several formulas that can be used to calculate the Darcy friction factor for turbulent flow.

$$\frac{1}{\sqrt{f}} = -2 \cdot \log \left(\frac{k/D}{3.7} + \frac{2.51}{Re \sqrt{f}} \right) \quad (28)$$

The implicit nature of the problem necessitates iterative solutions. Furthermore, to graphically compute the friction factor for both laminar and turbulent flow the Moody diagram (Figure 17) can be used and it will be presented more in detail in Section 2.4.7.

2.4.6 Heat transfer

Heat transfer refers to the energy flow between a system and its surroundings, which is predominantly caused by a spatial temperature difference. **Conduction** is the term used to describe the movement of heat caused by a temperature difference within a material through a solid body or stationary fluid, or when bodies with different temperatures come into physical touch. The Fourier's law, which was developed by Joseph Fourier in 1822, states that

$$q = -k \nabla T \quad (29)$$

where the negative sign indicates that heat flows from regions of higher to lower temperature [48].

Under the influence of the temperature differential between the fluid (T_∞) and the wall surface (T_w), **convection** is the process by which heat is transferred from one surface to a fluid in motion, or vice versa. There are two forms of convection: natural convection and forced convection. Natural convection is the outcome of internal buoyant forces brought on by density changes brought on by temperature variations in the fluid. On the other hand, forced convection is driven by outside mechanisms like fans or pumps. The flow over a heated plate is a popular example of convective heat transfer. In this case, energy diffuses at the surface and the moving fluid sweeps the heat downstream. In high-speed flows, forced convection is often present as the main heat exchange mechanism. In both cases, convective heat transfer can be expressed by Newton's law of cooling:

$$q = h(T_w - T_\infty) \quad (30)$$

The heat flux is therefore positive if the HT occurs from the surface to the fluid ($T_w > T_\infty$) and negative if it occurs the other way around ($T_w < T_\infty$). The convective heat transfer coefficient h is dependent on the boundary layer, which is impacted by the fluid characteristics and surface structure.

2.4.7 Surface roughness effects

The so-called Moody diagram, which shows the friction factor as a function of the Reynolds number and a relative roughness parameter, is frequently used in applications related to engineering. In this regard, finding appropriate correlations between these two parameters in channel flows is of primary concern. The three regimes in smooth circular pipes are as follows:

- Laminar regime: $\lambda = \frac{64}{Re}$
- Low turbulence regime: $\lambda = \frac{0.32}{Re^{1/4}}$
- Fully turbulence regime: $\lambda = \frac{0.12}{Re^{1/6}}$

A key tool in hydraulics and fluid mechanics, the Moody diagram, often called the Moody chart, is frequently used to calculate the friction factor for fluid flow in pipes. Lewis F. Moody created this graphical model in 1944, which offers a thorough way to relate the internal surface roughness, Reynolds number, and Darcy-Weisbach friction factor of a pipe. Moody's work created a single graphic that could be applied to a variety of cases by combining experimental data from other sources, including Nikuradse's groundbreaking experiments on turbulent flow in rough pipes. Laminar flow and turbulent flow are the two main zones that compose the Moody diagram. The flow is classified as laminar for Reynolds numbers less than or equal to 2300, and the friction factor can be computed immediately using the formula $f = \frac{64}{Re}$. The flow becomes turbulent at Reynolds numbers higher than approximately 4000, and the friction factor is influenced by both the Reynolds number and the relative roughness. There is a range of flow regimes in the transition zone between laminar and turbulent flow, where the Reynolds number falls between 2300 and 4000. This zone needs to be carefully interpreted.

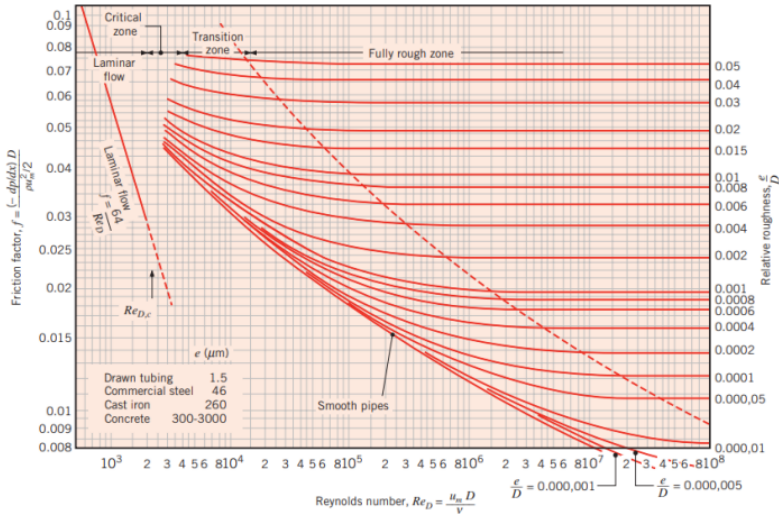


Figure 17: Friction factor for variable relative roughness circular tubes. [9]

A roughness scale that represents the impact of roughness features on the flow should be defined in order to take the influence of roughness on the flow into account. When defining roughness in rough-wall flows, the equivalent sand-grain roughness height is frequently employed in the literature. The original research by Nikuradse [22] and Schlichting [49] is where the equivalent sand-grain method derives. This method's genesis comes from Nikuradse's sand-grain investigations, which yielded information on the scaling laws. This approach's concept relies on the definition of a single length scale that may be used to describe roughness. There are several scaling laws for the velocity field and friction factors that can use this length scale.

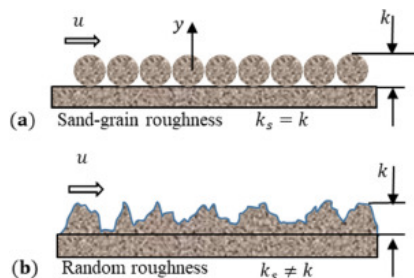


Figure 18: Difference between equivalent sand-grain roughness and randomly distributed roughness [8]

As illustrated in the Figure 18, assume that a uniform layer of densely packed spheres covers the surface. In order to preserve the case comparable to that of sandpaper, the diameter of the sphere is referred to as the sand-grain roughness height, or k . The sand-grain roughness height can be used to characterize the length scale for surfaces that are physically similar to the sand-grain in Nikuradse's experiment. One parameter, however, is no longer sufficient to characterize the sand-grain roughness when the roughness form diverges from the sand-grain. In this instance, these kinds of surfaces can be characterized using geometrical parameters. Colebrook and White [17] consequently developed an analogous length scale known as an equivalent sand-grain roughness k_s , as seen in Figure 18.

For non-uniform and irregular rough surfaces, the equivalent sand-grain roughness height yields the same outcomes as the uniform sand-grain of the Nikuradse for a completely rough flow regime. The viscous sublayer's law-of-the-wall is affected by the roughness. The definition of "roughness Reynolds number" in relation to the law of the wall is defined as:

$$k_s^+ = \frac{k_s u_\tau}{\nu} \quad (31)$$

The flow above rough surfaces regimes can be classified into three primary types based on the three wall areas that impact the turbulent boundary layer. [8] Take into consideration the two crucial values of the roughness Reynolds number, k_{smooth}^+ and k_{rough}^+ . Afterwards, based on three distinct roughness regimes and varying values for the roughness Reynolds number:

- Hydraulically smooth regime($k_s < k_{\text{smooth}}^+$): Skin friction and drag coefficient remain unchanged and all of the roughness elements are totally submerged in the viscous sublayer.
- Transitionally rough regime($k_{\text{smooth}}^+ < k_s < k_{\text{rough}}^+$): the skin friction and drag coefficients are affected by the Reynolds number and also by the relative roughness in this regime. This indicates that the skin friction and drag coefficient are influenced by both pressure and viscous forces. The wall damping effect's influence is lessened in the transitionally rough regime, which is linked to a reduced sublayer thickness.
- Fully rough regime($k_s > k_{\text{rough}}^+$): the logarithmic profile is shifted downward when the rough parts extend into the fully turbulent zone. In this flow regime, the massive turbulence mixing generated by roughness elements completely destroys the viscous sublayer. Pressure force on the roughness causes a large increase in friction drag, which is independent of the viscous effect (Reynolds number). When roughness elements penetrate the viscous sublayer, the pressure loss becomes independent of the fluid's molecular viscosity and velocity.

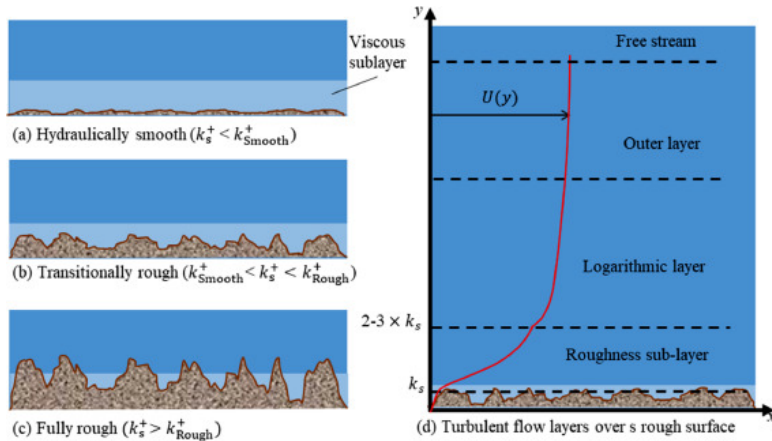


Figure 19: Roughness regimes classification [8]

"Roughness sublayer" refers to the complete layer that is dynamically modified by the length scale associated with roughness elements. The roughness outer, logarithmic, and sublayers are indicated in the velocity profile schematic over roughness that is depicted in the Figure 19. The roughness sublayer is the viscous sublayer's roughness mitigate and is located beneath the inertial or logarithmic layer. With k representing the roughness height in relation to the wall, the roughness sublayer is stretched to approximately $\approx 2k - 5k$. Schultz and Flack [50] suggest using k_s rather than k to define the roughness sublayer extension since k_s offers a common measurement of the impact of surface roughness on mean flow. As demonstrated, the roughness sublayer extends to around $\approx 3k_s - 5k_s$.

2.5. Infrared thermography

Understanding the temperature distribution on a surface is essential for studying thermal behavior in many HT applications. This is especially relevant in convective heat transfer investigations, like the ones carried

out in this study, where possible problems from measurement instruments make the direct measure of surface temperature extremely difficult. It turns out that IR thermography is a useful method that provides two-dimensional, contactless temperature readings. This method finds the electromagnetic energy that an object of interest emits by employing an IR scanning radiometer within an IR camera. It is crucial to have a basic understanding of electromagnetic waves and thermal radiation in order to appreciate the concepts underlying IR thermography. The electromagnetic spectrum is composed of multiple sections, each having unique wavelengths, as Figure 20 shows.

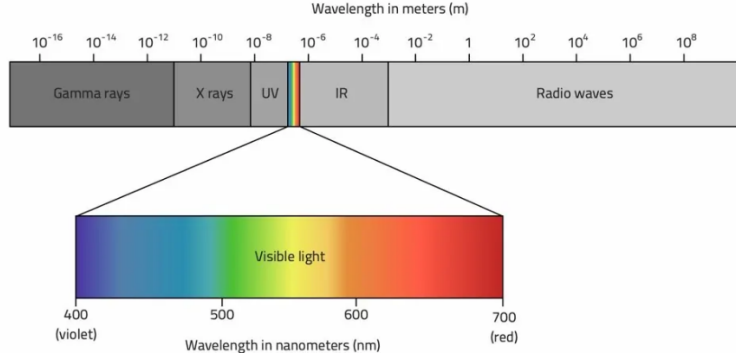


Figure 20: Electromagnetic spectrum

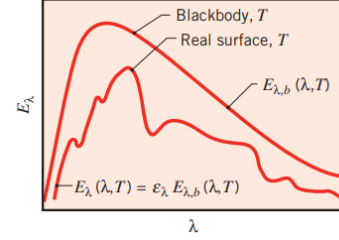


Figure 21: Comparison of blackbody and real surface emission [9]

This vast bandwidth is just partially made up of the visible light spectrum. The IR spectral band is commonly separated into three parts: the long-wave region, which spans from 7 to $14 \mu m$; the mid-wave region, which spans from 3 to $5 \mu m$; and the short-wave region, which spans from 0.9 to $1.7 \mu m$. Every object that has a temperature higher than absolute zero releases thermal radiation; a blackbody, also known as a perfect emitter, emits the most radiation from a body at a given temperature. Planck's law of radiation provides a thorough description of the spectrum distribution of a blackbody's monochromatic radiation intensity.

$$E_{\lambda b} = \frac{C_1}{\lambda^5 (e^{C_2/\lambda T} - 1)} \quad (32)$$

The IR detector, which determines the spectral range in conjunction with the optical system, is the central component of the infrared imaging system. By absorbing the thermal radiation released by the surface and translating it into an electrical signal, such as voltage or current, this detector acts as a transducer. The detector material facilitates this conversion, in which photon absorption results in the direct emission of electrons. Indium antimonide (InSb) sensors are used in the majority of infrared cameras available today. The fact that Planck's law defines radiation from a BB must be taken into account when relating the electrical signal from a real object to temperature readings. The spectral emissivity

$$\epsilon_\lambda = \frac{E_\lambda}{E_{\lambda b}} \quad (33)$$

which expresses the ratio of radiation emitted by a real body to that released by a BB, must be included since real objects produce less radiation than a BB (Figure 21). Determining the surface emissivity of an object is necessary for accurate temperature measurement using infrared thermography, as it plays a major role in the measuring process. Furthermore, warm things close to the infrared camera may have an impact on the results since the detector may absorb radiation from nearby objects, possibly producing inaccurate results. How the experiments will be conducted in this work will be presented more in detail in Chapter 3.1.1.

2.6. Particle Image Velocimetry velocity field calculation and correlation theory

The measurement of the displacement of small tracking particles carried by the fluid over just a short amount of time is the basis of the PIV principle. The test system of PIV is shown in Figure 22 A digital imaging device, usually a high-speed camera positioned perpendicular to the measurement plane, records the light scattered by the tracer particles onto two consecutive image frames. The tracer particles are illuminated within a thin light sheet generated by a pulsed light source (typically a double-head pulsed laser system). This method then involves analyzing the particle-image patterns in small sub-domains, or interrogation zones, between the first and second image frame using cross correlation. The local fluid velocity is obtained by dividing the displacement of the particle-image pattern by the image magnification and the interval between laser light pulses. This procedure generates the instantaneous velocity in a plane cross-section of the observed flow and is repeated for the whole

picture domain. The quasi-steady viscous term (Stokes drag) dominates the particle dynamics for very small particle tracers, such as those used for PIV. Therefore, the following estimate can be used to calculate the difference between the particle velocity \mathbf{V} and the fluid's surrounding velocity \mathbf{U} as:

$$\mathbf{V} - \mathbf{U} = \frac{2}{9} \frac{a^2 (\rho_p - \rho_f)}{\mu} \frac{d\mathbf{V}}{dt} \quad (34)$$

where $a = \frac{1}{2}d_p$ is the tracer particle radius and ρ_p and ρ_f are the density of seeding particles and fluid respectively.

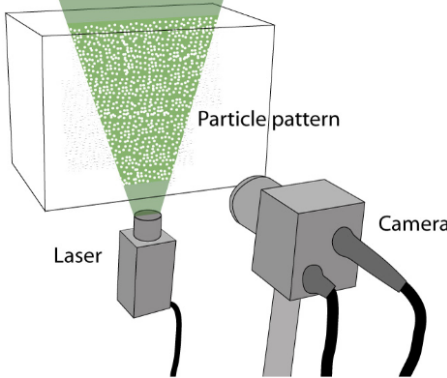


Figure 22: Particle Image Velocimetry system scheme

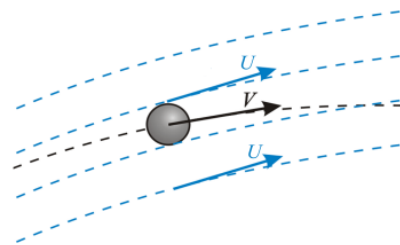


Figure 23: Particle velocity disparity against surrounding fluid velocity

Equation 34 makes it clearly evident that particles tracers that precisely follow the flow can be generated as long as buoyancy neutral particles $(\rho_p - \rho_f)/\rho_f \ll 1$. The particle velocity disparity against the flow velocity is shown in Figure 23. Although this requirement is easily met for liquid flows, it is not met for gas flows, when smaller diameter particles ($0.5\mu\text{m} < d_p < 5\mu\text{m}$) are used and the density ratio often has a value of $\rho_p/\rho_f = O(10^3)$. In the event in which $\rho_p/\rho_f \gg 1$ (gas flows), let's examine the equation 34 and such relation is a first-order ordinary differential equation (ODE). The solution is expressed as particle time response τ_p which is the time after which the particle velocity changes of $1 - e^{-1} = 63\%\Delta U_{1-2}$:

$$\tau_p = d_p^2 \frac{\rho_p}{18\mu} \quad (35)$$

Consequently, the particle time response must to be kept smaller than the flow's smallest time scale in order to enable the tracer particle to accurately track the flow. The particles Stokes number S_k , which is the ratio of τ_p to the characteristic flow time scale τ_f , is employed to quantify the accuracy of the flow tracers in turbulent flows.

$$S_k \equiv \frac{\tau_p}{\tau_f} \quad (36)$$

The most critical circumstances arise when particle tracers are submerged in high Reynolds number turbulent flows that reveal an extensive spectrum of turbulent scales. Practically speaking, the requirement $S_k < 0.1$ yields a flow tracing accuracy that is acceptable with errors under 1%. The operations shown in Figure 24 are combined to assess the particle tracers' motion field. The process of partitioning an image into small cells, each containing a statistically significant number of tracers (at least 10), is known as image windowing. The local velocity vector is obtained in each individual measurement volume, which is an interrogation cell or window. Applying a statistical tracking operator to the respective windows derived from the two exposures, a cross-correlation analysis function is employed. The two-dimensional array that is produced as a result of this procedure is called discrete cross-correlation map, and its peak locus relative to the origin represents the average displacement of particle images. The particle motion is represented by the greatest peak in the correlation map, whose location can be inferred from the nearest integer pixel shift. The particle velocity in terms of pixel shift between the relevant windows is yielded by the result obtained at point. The velocity is calculated by multiplying by the pixel size, dividing by the imaging magnification, and dividing by the known time interval between laser pulses. Let us examine two interrogation windows, denoted as $I(x, y, t)$ and $I'(x, y, t + \Delta t)$, which are defined at time instants t and $t + \Delta t$, respectively.

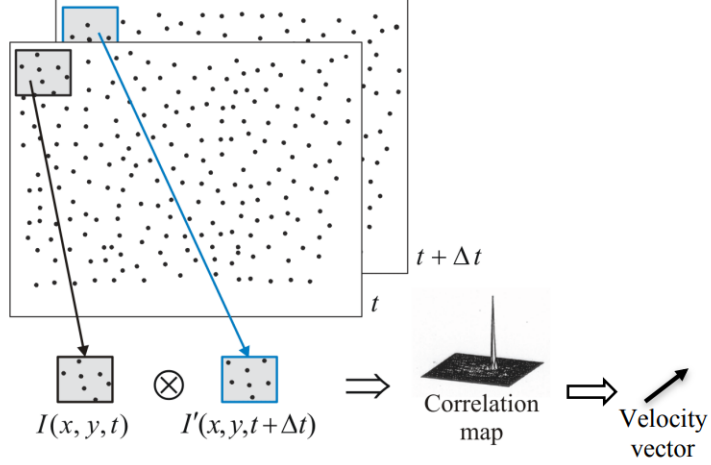


Figure 24: Image windowing and discrete cross-correlation map.

The cross-correlation function ϕ is computed in order to extract the particle image displacement that is most likely to have occurred in the time interval Δt :

$$\phi(m, n) = \frac{\sum_{i=1}^I \sum_{j=1}^J I(i, j) \cdot I'(i + m, j + n)}{\sqrt{\sum_{i=1}^I \sum_{j=1}^J I^2(i, j) \cdot \sum_{i=1}^I \sum_{j=1}^J I'^2(i, j)}} \quad (37)$$

In equation 37, I and I' have been previously subtracted of their respective mean value to remove the DC component of the signal. The correlation function is a discrete function that is only defined at discrete pixel positions, whereas the displacement of particle pictures is typically not an integer number of pixels. Therefore, the correlation peak, shown in the Figure 25, is interpolated around its maximum in order to extract the particle image displacement with sub-pixel precision.

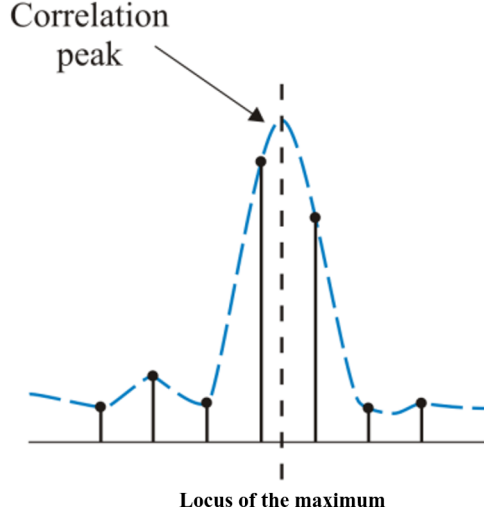


Figure 25: Sub-pixel interpolation of correlation peak.

For this application, a number of peak interpolation algorithms may be used; however, the gaussian has demonstrated the best performance among them since it can more correctly resemble the particle picture shape as Gaussian than a parabola.

$$f(x) = \phi_0 e^{-\frac{(x-x_0)^2}{\sigma^2}} \quad (38)$$

where y_0 and x_0 can be defined as:

$$\begin{aligned} x_0 &= i + \frac{\ln \phi(i - l, j) - \ln \phi(i + l, j)}{2 \ln \phi(i - l, j) - 4 \ln \phi(i, j) + 2 \ln \phi(i + l, j)} \\ y_0 &= j + \frac{\ln \phi(i, j - l) - \ln \phi(i, j + l)}{2 \ln \phi(i, j - l) - 4 \ln \phi(i, j) + 2 \ln \phi(i, j + l)} \end{aligned} \quad (39)$$

The Wiener-Khintchine theorem-based Fourier Transform (FT) is utilized in an effective version of the cross-correlation operator:

$$f \otimes g = FT^{-l}[FT(f) \times FT(g)] \quad (40)$$

As a result, Figure 26 provides a revised schematic representation of the motion evaluation which utilizes the use of the Fourier transform operator.

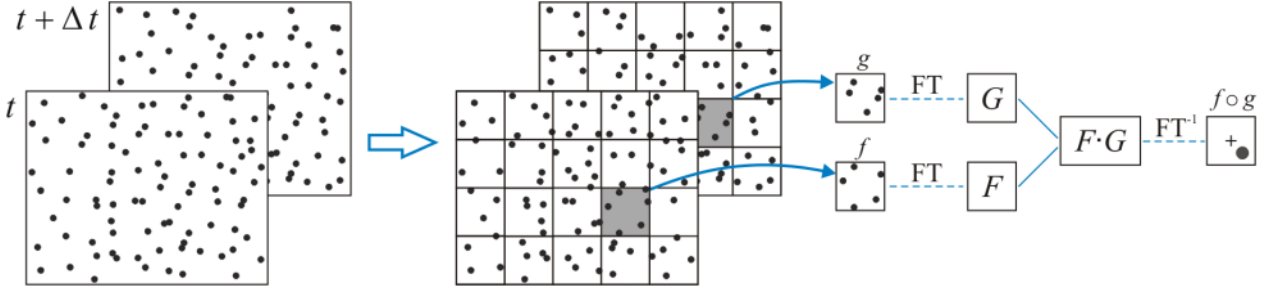


Figure 26: Correlation map evaluation by Fourier transform.

The Fast Fourier Transform (FFT) technique must be used in conjunction with the Discrete Fourier Transform (DFT) in order to achieve an increase in computational performance.

3. Experimental Set-Up

3.1. Surface Roughness Heat Transfer rig

3.1.1 Working principle

The experimental part in the SRHT rig starts with the set up of the IR camera by the *FLIR's ResearchIR* software and the opening of the valves that permit the air to flow inside the flow straightener channel and reach the test section. The process flow diagram is reported in Figure 27. The cross-section of the hatch is slightly larger than the test section. There is a step approximately 5 mm tall when the air enters the test section from the hatch, which will disturb the boundary layer. The air supply system has a pressure of 8 bar, valve 1 is linked

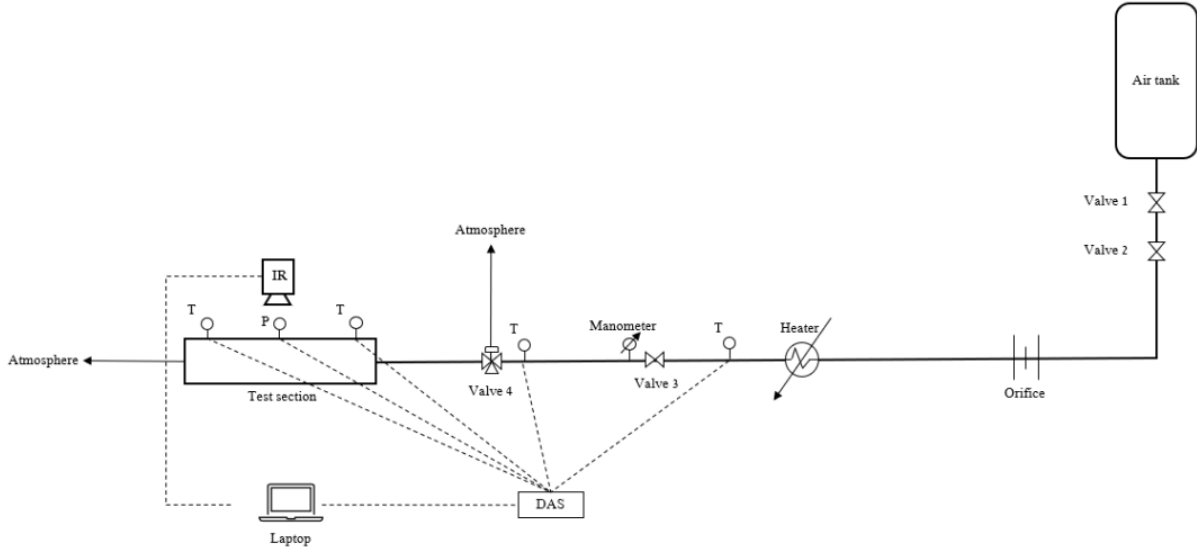


Figure 27: Process flow diagram

to a pneumatic actuator to open the hatch, while valve 2 is the one sending the air to the orifice meter where the pressure difference is used to calculate the mass flow, which can be controlled by a manual valve regulator positioned upstream of the flow straightener in order to reach the required Reynolds number. The mass flow is calculated as

$$\dot{m} = \rho \mu_\infty A \quad (41)$$

where μ is the dynamic viscosity calculated using Sutherland's law:

$$\frac{\mu}{\mu_0} = \left(\frac{T}{T_0}\right)^{\frac{3}{2}} \frac{T_0 + S_\mu}{T + S_\mu} \quad (42)$$

S_μ is the Sutherland's constant in Kelvin and it varies based on the gas. For air, $S_\mu = 111K$, $T_0 = 273K$, and $\mu_0 = 1.716 \times 10^{-5} kg \cdot m^{-1} \cdot s^{-1}$. T during the tests is kept constant at 70°C.

$$Re = \frac{\dot{m}D_h}{\mu_{air}A} \quad (43)$$

The main flow is heated up and a pressure valve regulator (valve 3) lowers the pressure to 1.5 bar. The mainflow proceeds in the direction of a three-way valve (valve 4), which is situated upstream of the test section and is composed of a bypass, a hatch, and a pneumatic actuator. The temperature before the fourth valve is measured by a thermocouple and the value is only used for safety reasons to check if there are any anomalies in the heating process. From the formula above the temperature is a known value depending on which Re is going to be tested and it can be reached controlling the heater power through an Arduino code, the hatch will be opened by a switch only when the flow straightener has stabilized (Temperature changes < 1 degrees/minute). It seals the bypass allowing the mass flow into the test area after the main flow achieves the required temperature, which is determined by measuring it with a Pt100 thermocouple upstream of the three-way valve. On the other hand, when the temperature is not at the acceptable level and the hatch is closed, the bypass is directing the mass flow out of the test section and into the atmosphere. However during the test, the time variation of the wall temperature T_w given by the air passing over the rough surfaces is recorded for 110 s by the IR camera that is placed over one of the openings and a maximum number of 1500 frames is acquired. Each run of the experiment could only be conducted for one window of the top plates. This means that in order to capture the whole length of the test section for one Reynolds number, nine separate runs had to be performed including a change of top plates in the meantime. During the tests in fact only one of these openings is closed with a peculiar window, made by a high-transmissivity material Calcium Fluoride specific for IR imaging, while the others are sealed with lids. Two thermocouples at the test section's inlet and outlet, in the middle of the cross-section measure the bulk temperature, which is used to compute the mass flow temperature T_∞ via linear interpolation.

3.1.2 Measurement devices

Here are presented the components of the SRHT setup that allow the experiments to be conducted.

- **Data Acquisition System DAS:** the Data Acquisition Systems employed in this study is composed by sensors for measuring physical quantities, signal conditioners for amplifying and filtering signals, and analog-to-digital converters for turning analog signals to digital format. A laptop running a customized software for data storage, to visualize the parameters and keep them under control. A Netscanner 9116, a 16-channel piezoresistive transducer with a pressure range of -5860 to 5860 kPa and an uncertainty of ±0.05% F S, is used to monitor pressure. The measured readings are connected to an Agilent 34972A data logger, which acts as the main interface with the laptop, and calibrated using a precision measuring tool called the Rosemount 2088 Absolute and Gauge Pressure Transmitter. An internal program called RigView, which is comparable to LabView, makes it easier to collect data by allowing temperature and pressure readings to be recorded in.txt files. Moreover, a Datascan 7220 Measurement Processor with 16-bit resolution is used for mainflow temperature measurement. Data are acquired with a frequency of 1Hz and for a duration of 110s, giving a number of samples of 110.
- **IR Titanium 560M camera:** this model is made by Cedip Infrared Systems (Figure 28).



Figure 28: IR camera

IR Camera Type	Titanium 560M
Sensor Type	InSb
Waveband	3 – 5 μm or 8 – 12 μm
Pixel Resolution	640 × 512
Integration Time	1200 μs
Frame Per Second (FPS)	10 Hz
Calibration Temperature Range	-15 ÷ 110°C
Calibration Device	Dias CS110

Table 2: IR camera technical parameters

The camera is connected to the FLIR ResearchIR program, which provides a user-friendly interface for obtaining infrared data and adjusting settings. The camera settings are reported in Table 2.

- **Heater:** the primary duct is heated by the heater (Figure 29), which is connected to resistors coupled to the power supply system. A thermal relay, a power control system, and the electronics required to run the air heater are all housed inside the heater controller, as shown in Figure 30. This system makes it possible to achieve variable Reynolds numbers in the test section by reaching the corresponding temperature linked to a specific Re.

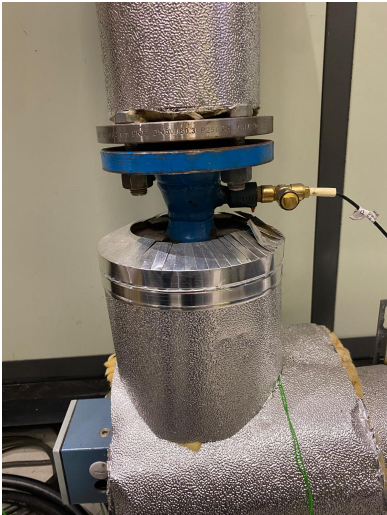


Figure 29: Heater



Figure 30: Heater controller



Figure 31: Three-way valve

- **Flow straightener:** is located upstream of the test section (Figure 33) and its function is to give the precise direction to the flow so that it is correctly aligned with the test section. It is 190 cm long, 17 cm wide, 12 cm high.
- **Three-way valve:** is made of aluminium and has the purpose of sealing the inlet of the test section by releasing air into the atmosphere until the temperature is high enough, or vice versa sealing the bypass during experiments when air is inside the test section. This movement occurs because it is connected to a shaft, which is opened by a pneumatic actuator that applies torque. The hatch itself is not visible from the outside, but it is located in the connection part between the flow straightener and the test section, as shown in Figure 31.
- **Thermocouples:** the thermocouples used for this experiment are type K with technical features reported in Table 3.

Temperature range	
Thermocouple grade wire	-270÷1260°C
Extension wire	0÷200°C
Accuracy	
Standard	± 2.2°C
Special limits of error	± 1.1°C

Table 3: Thermocouple technical parameters

- **Test section:** The test section consists of a rectangular duct with a bottom carrier and top plate that houses five plates with 3D printed rough surfaces on them. The top plate comes with five windows (Figure 32), where the opening is aligned with the center portion of the plate. By taking off a few allen screws, one can manually swap out the test objects on the bottom plate, whether they have smooth or rough surfaces. The hatch's cross-section is notably slightly larger than the test section, which causes the boundary layer to be disrupted as air enters in a 5 mm step. Likewise, the outlet bend causes the boundary layer to be disturbed, causing the mixing of the air and the center temperature to approximate quite well the bulk temperature. The test section is 815 mm long, the rectangular cross-section has an hydraulic diameter of 96.7 mm, with an internal width of 100 mm and an internal height of 90 mm. The direction of the flow is shown by the red arrows in Figure 33.

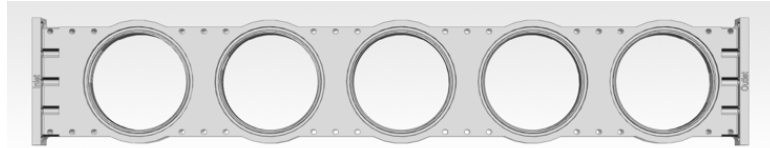


Figure 32: Top plate

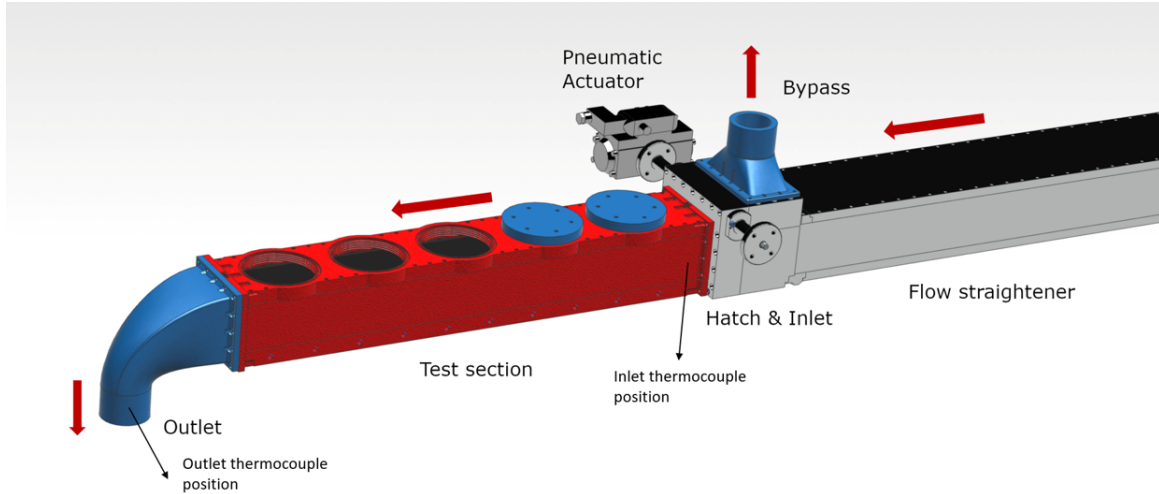


Figure 33: SRHT rig set-up with flow direction

3.1.3 Analogue rough surface

The test objects for the experiments carried out in this thesis are rough surfaces plates, of 90 mm width, 150 mm length and 15 mm height. They have been modelled by previous student based on the roughness characteristics of the materials that are commonly used in cooling channels by Siemens Energy. The test objects are going to be named Analogue surfaces, because they have been obtained by upscaling the rough surface of Inconel939 and Aluminium microchannel, printed in L-PBF. The upscaling factor is calculated using the duct's dimensions and accounting for the rounded corners, which have a radius of 5 mm. The ratio between the hydraulic diameters of the upgraded test rig and the hydraulic diameter of the channel itself yields this factor.

$$s = \frac{D_{\text{upscaled}}}{D_{\text{real-size}}} = \frac{96.7}{1.53} = 63.15 \quad (44)$$

MATLAB was used to compute the hydraulic diameter of the real channel by manually tracing the perimeter of the duct. To get the main roughness parameters as mentioned in Section 2.3.2, profilometer measurements were made in an effort to simulate actual surface roughness for thermal analysis. Though with certain adjustments and simplifications, the techniques of Clemenson et al. [25] and Hanson [28] serve as inspiration for the process of developing an analogue surface model. This chapter describes the procedures used to create the analogue rough surface models and the study that was done on their thermal properties afterward. There are several crucial steps in the process of creating the analog surface model:

1. **Profilometer Measurements:** this is to compile the average SR parameters. The upscaling factor for the rough elements is determined by these parameters.
2. **Diameter Selection from SEM Images:** diameters are selected manually from SEM pictures using a MATLAB algorithm. The optimal statistical distribution for the upscaled diameters is identified, and the sphere density per square millimeter is computed. Although the rough elements are not always exactly spherical, their deviation from the spherical shape is negligible to the point that they have been treated as spheres. The spheroids on the real surface can be observed in Figure 56.
3. **3D Model Creation:** using the offset statistical distribution and the diameter statistical distribution as inputs, NX software generates a 3D representation of the analog rough surface.
4. **Adjustment of Sphere Positions:** the output roughness parameters of the analogue SR model are computed by moving spheres that lie outside the edges or over the reference points. For the rough surface of the real-size channel to be accurately simulated, the sphere densities must be maintained. The surface area of the manually chosen diameters can be used to calculate this parameter.

$$\rho_s = \frac{\text{number of spheres}}{A \cdot s^2} = 0.06 \quad (45)$$

In the previous works, Wen's [51] analogue SR for Inconel939 was obtained optimizing three out of five rough parameters, as shown in Table 4.

	R_a [mm]	R_q [mm]	R_z [mm]	R_{sk}	R_{ku}
Inconel939					
Real SR parameters (upscaled)	1.077	1.325	5.689	0.46	2.79
Analogue SR parameters	1.103	1.304	5.741	0.944	3.157
Percent Error	2.41%	1.58%	0.91%	105.2%	13.62%
Aluminium1					
Real SR parameters (upscaled)	0.37	0.47	2.32	0.22	3.47
Analogue SR parameters	0.37	0.49	2.35	2.00	5.80
Percent Error	0%	4.25%	0.8%	814%	67.27%
Aluminium2					
Real SR parameters (upscaled)	0.37	0.47	2.32	0.22	3.47
Analogue SR parameters	0.62	0.69	2.48	0.29	3.50
Percent Error	66.7%	44.81%	7.27%	1.36%	0.94%

Table 4: Comparison of real and analogue surface roughness parameters.

Brogliato [52] instead modelled two different analogue RS for aluminium, the first one matching the R_a , R_q , and R_z parameters (Al1), while the second one matching the R_{sk} and the R_{ku} ones (Al2).

The goal would be to create a rough surface that is as similar as possible to the real one. This thesis focuses on the third surface, Al2, whose behavior differs from the previous two and will be explained and further analyzed in section 5. The plate was created using Accura Xtreme gray material and stereolithography (SLA). A fine surface finish was guaranteed by setting the layer thickness to 0.1 mm. Table 5 provides specifics on the thermal characteristics of the material: thermal conductivity k and heat capacity C_p . It is significant to remember that k_{rad} relates to conductivity along the layers, but k_{ax} indicates the conductivity through the layers, which determines the heat transfer through the plate. The emissivity ε and reflectivity ρ must be found in order to compute the surface temperature using IR camera data. The ability of an item to emit infrared energy is measured by its emissivity, where a perfect black body has $\varepsilon = 1$. The ability of an object to reflect infrared energy is measured by its reflectivity, and for an opaque body is true that $\varepsilon + \rho = 1$. For the test objects

T [°C]	k_{ax} [W/mK]	k_{rad} [W/mK]	C_p [J/kgK]
23	0.224	0.211	1442.4
50	0.227	0.237	1735.9

Table 5: Thermal properties of Accura Xtreme grey material at different temperatures.

to behave as close as possible as a BB and for the accuracy of the measurements to be high enough, a black paint resistant to high temperatures from *Senotherm* was applied to the surface, its parameters were calibrated by Lehmann [53], producing the following results: $\varepsilon_{\text{paint}} = 0.9072 \pm 0.0274$ and $\rho_{\text{paint}} = 0.0540 \pm 0.0062$. This whole process of generation of an analogue rough surface comes with some limitations:

- Despite being measured at six distinct points, the stylus-profilometer data were obtained along a straight line, which limits their representativeness of the 3D surface roughness characteristics.
- Although spheres were chosen as the SR elements in this investigation, other forms can also be taken into account for examination.
- It's also critical to remember that the direction and velocity of the printing process have an impact on the roughness characteristics of a particular material. This limits this investigation narrowing our field of interest.

The three analogue surfaces used as test objects are presented in Figure 37. They differ a lot from each other, for spheres' size, roughness height and density. The purpose of this modellization is not only to try to represent the material as more similar as possible to the real one, but also to understand, given the evident variations in SR parameters, what are the differences in the impact on local heat transfer. More in details for the aluminium, how the different parameters can have a different impact on the overall heat exchange.



Figure 34: Inconel939



Figure 35: Aluminium1

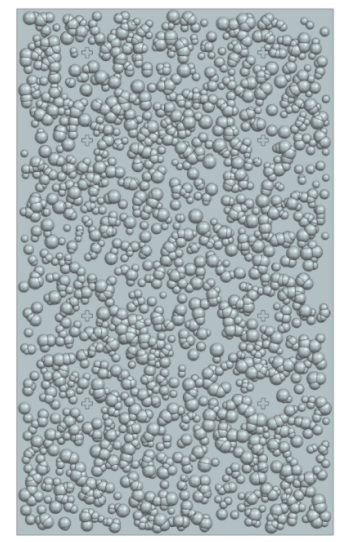


Figure 36: Aluminium2

Figure 37: CAD model of the up-scaled analog AM roughness plate

3.1.4 Post processing

A thorough post-processing approach needs to be described in order to comprehend how the heat transfer coefficient is obtained from raw data for 1D and 3D solvers. Both bulk temperature processing and video processing are involved in this process. In particular, there are differences in the method for calculating HTC between smooth and rough plates, but the basic principle on which the post process stands is the same, which is finding the convective HTC by measuring the distribution of T_w over the plates in a transient experiment. For this specific test the Nusselt number can only be determined indirectly through heat conduction at the wall.

$$Nu = \frac{hD_h}{k_{air}} \quad (46)$$

A thermal boundary layer is formed when a mass flow with T_∞ crosses a surface with T_w . The product of the convective HTC and the temperature differential between the wall and the flow yields the convective heat flux, in accordance with Newton's law of cooling, from which the HTC can be derived. In addition, Fourier's law can be used to define the quantity of convective heat flux near the surface, where only conduction occurs, in this way it is valid to assume that the two heat transfer expressions gives exactly the same value of heat exchanged on the surface. By solving a transient conductive problem to find the convective HTC, the Nusselt number may be computed knowing the fluid's thermal conductivity k_{air} , a property that can be found in standard tables.

$$h = \frac{\dot{q}_w}{T_w - T_\infty} \quad \longrightarrow Nu = \frac{-\nabla T|_w}{(T_w - T_\infty)/D_h} \quad (47)$$

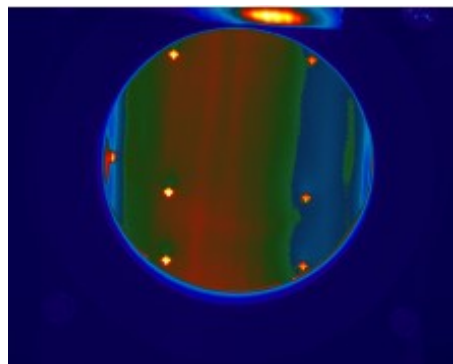


Figure 38: Captured frame.

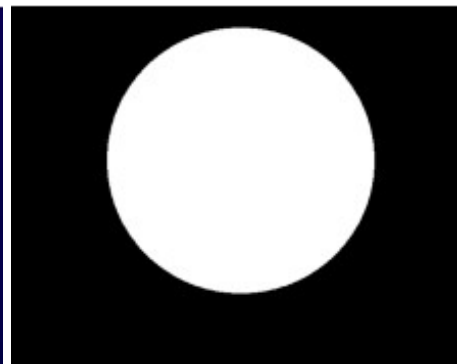


Figure 39: ROI mask.

This basic idea is used by the SRHT rig to calculate the local HTC for both smooth and rough surfaces. The post processing of the tests start from the data acquired from the IR camera, and the program utilized for

IR video processing *FLIR's ResearchIR* saves and shows videos in the form of .PTW files. Establishing the experiment's start frame is the first step. This is accomplished by synchronizing the placement of a light bulb next to the infrared window with the switch controlling the pneumatic actuator. The flashing light signifies the experiment's activation in the recording. The region of interest (ROI) will be chosen in the next phase. With a pixel resolution of 640x512, every frame captured the surrounding region of the infrared window and the test section's lower plate. Only a particular area of the picture is important for precise HTC computations. An ellipse is manually drawn over the ROI to identify this region as in Figure 38, and then the binary mask containing the ROI is exported to produce a black-and-white picture, as Figure 39 is showing. Using the calibration function $F_{S \rightarrow T}$, the digital level of the radiometric signal within this ROI is transformed into wall temperature data. The inlet and outlet bulk temperatures T_∞ of the channel were previously saved in a .txt file for bulk temperature processing. The heat conduction equation

$$\frac{T(z, t) - T_i}{T_\infty - T_i} = \operatorname{erfc}\left(\frac{z}{2\sqrt{\alpha t}}\right) - \left[\exp\left(\frac{hz}{k} + \frac{h^2\alpha t}{k^2}\right)\right] \left[\operatorname{erfc}\left(\frac{z}{2\sqrt{\alpha t}} + \frac{h\sqrt{\alpha t}}{k}\right)\right] \quad (48)$$

is utilized by the 1D solver inside the ROI chosen in the video to determine the one unknown variable, which is the HTC, in the case of smooth surfaces. Figure 41 shows how the local wall temperature changes over time for each pixel. Simultaneously, there is temporal and spatial fluctuation in the bulk temperature, which is the main flow temperature, shown in Figure 40.

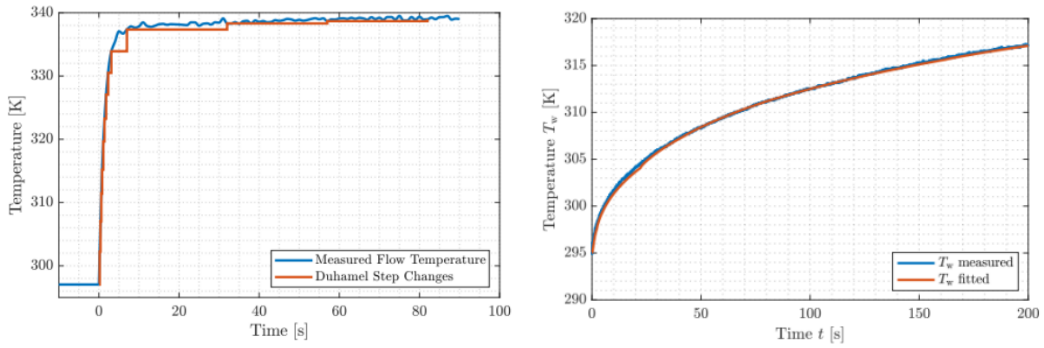


Figure 40: Variation in time of the mainflow temperature.

Figure 41: Variation in time of the wall temperature.

With discrete temperature step changes $\Delta T_{\infty,j-1}$ approximating the main flow temperature throughout each window, the Duhamel solver can be used, assuming finite time-steps, as described by Metzger and Larson [54]. The main solver equation is

$$T_w - T_i = \sum_{j=1}^N \left[1 - \exp\left(\frac{h^2}{k^2\alpha(t - \tau_j)}\right) \operatorname{erfc}\left(\frac{h}{k}\sqrt{\alpha(t - \tau_j)}\right) \right] \Delta T_{\infty,j-1} \quad (49)$$

Furthermore, the HTC and Nusselt number must be laterally averaged along each streamwise position (Equation 50). For each line of pixels perpendicular to the streamwise direction within the area indicated by the red square in Figure 43, the HTC and Nusselt numbers are averaged. The reason why not the whole area is taken into account is to avoid the lateral walls effect and therefore acquired values that could not be accurate. From those values are then calculated the global average for each window (Equation 51). A comparison is presented in Figure 42.

$$\bar{h}_i = \frac{\sum_{j=1}^N h(x_i, y_j)}{N}, \quad \bar{Nu}_i = \frac{\sum_{j=1}^N Nu(x_i, y_j)}{N} \quad (50)$$

$$\bar{h}_0 = \frac{\sum_{i=1}^M \bar{h}_i}{M}, \quad \bar{Nu}_0 = \frac{\sum_{i=1}^M \bar{Nu}_i}{M} \quad (51)$$

For the rough surfaces the process is different since the 3D effects need to be taken into consideration, while Equation 49 does not. The IR videos are first processed to translate the radiometric signal from the IR camera into the wall temperature, which is then entered into the C3D solver, a custom in-house solver of Siemens Energy. These data are utilized in conjunction with the bulk temperature, which is obtained via linear interpolation, to solve the adjoint problem. C3D allows the computed surface temperature and the measured surface temperature for every node to be compared and the local HTC to be calculated using a numerical

method. What the calibration solver does, for the 3D rough surface post processing, is resolving a heat transfer problem, defined like this:

$$\begin{cases} \rho c \frac{\partial T}{\partial t} = \nabla \cdot (k \nabla T) & \text{in } \Omega, \quad 0 \leq t \leq t_f, \\ k \frac{\partial T}{\partial n} = h(T - T_\infty) & \text{on } \Gamma, \quad 0 \leq t \leq t_f, \\ T(x, t=0) = T_0(x) & \text{in } \Omega. \end{cases} \quad (52)$$

For every time step ($t = 0, 10, 20, 40, 70, 100$ [s]), calibration data are imported to the C3D and the simulation stops when the residual is under a certain tolerance. From the HTC, the Nusselt number is obtained: Figure 43 is the plot of local Nussel obtained for Reynolds 25000 in the last window of the channel. Lastly, for each window, the global and lateral averages of the HTC and Nusselt numbers are calculated in the same way as for the smooth surfaces.

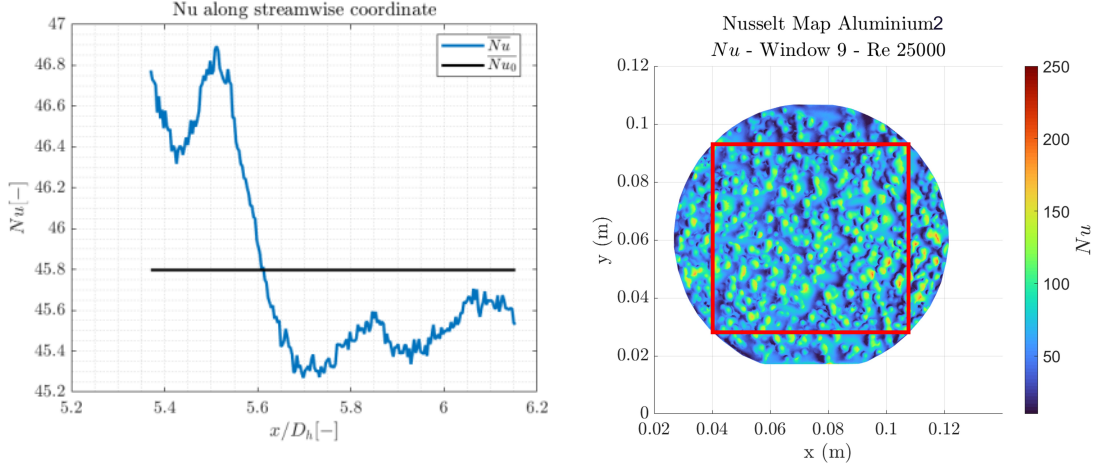


Figure 42: Laterally averaged Nu and globally averaged Nu comparison.

Figure 43: Nusselt plot in the ROI.

3.2. Particle Image Velocimetry rig

3.2.1 Working principle

The measurement of the displacement of small tracer particles carried by the fluid during a short interval of time is the core of the PIV principle. A digital imaging device, usually a high-speed camera positioned perpendicular to the measurement plane, records the light scattered by the tracer particles onto two consecutive image frames. The tracer particles are illuminated within a thin light sheet created by a pulsed light source (a double-head pulsed laser system). A common setup for PIV experiments is shown in Figure 44.

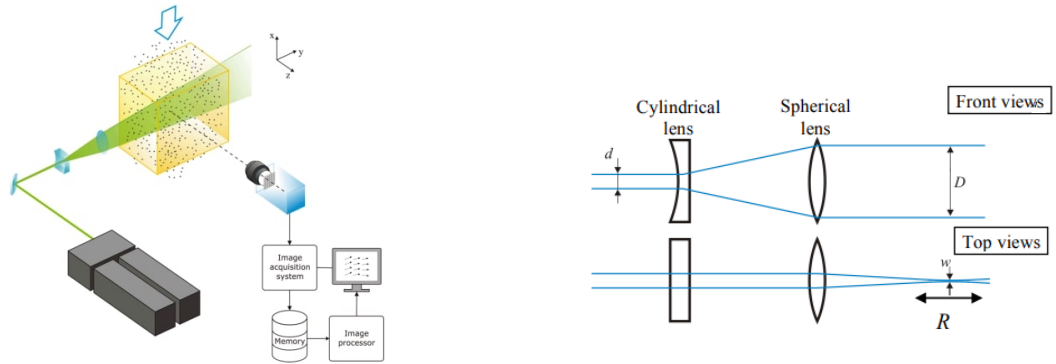


Figure 45: Light sheet formation optics.

Figure 44: Scheme of the PIV measurement system

As shown in the Figure 45, the light source's circular cross section beam is formed into a thin sheet with a constant width employing spherical and cylindrical lenses. In this particular case, a spherical lens with a focal length of $f_2 = 500\text{mm}$ follows a cylindrical lens with a focal length of $f_1 = -40\text{mm}$, expanding the beam vertically and balancing the previous lens's effect. As a result, the system can be described as a vertical beam expander with an expansion ratio of $D/d = f_2/f_1$, where d and D represent the original and final beam

dimensions, respectively. The spherical lens will focus the beam at a distance equal to the focal length, while the cylindrical lens has no influence on it in the horizontal direction. This configuration is especially well-suited for achieving constant light along the path of propagation. The laser sheet waist, which is the minimum thickness of the sheet, is inversely proportional to the initial laser beam diameter and proportionate to the focal length of the second lens:

$$w = 2 \frac{2.44\lambda f_2}{d} \quad (53)$$

It is convenient to build the light sheet optics such that the beam waist does not fall inside the measurement region in order to reduce the fluctuation of the light sheet features within the area of interest. A lens on the surface of an image sensor creates an image of the tracer particles in the light sheet. The thin lens formula defines the imaging system's focal length (f), f-number (or f-stop), which is defined as $f\# = f/D$ (where D is the lens aperture diameter), and image magnification (M), which is the ratio of the image distance (d_i) to the object distance (d_o):

$$\frac{1}{f} = \frac{1}{d_i} + \frac{1}{d_o} \quad (54)$$

$$M = \frac{d_i}{d_o} \quad (55)$$

The ratio of the photographed object size (field of view, or FOV) to the sensor size, which is determined by the number of pixels in the sensor, may also be used to estimate the magnification factor. If the small tracer particles were captured as "spots" according to the geometric optics, the particle images would have a diameter equal to $d_{\text{geom}} = M d_p$. Diffraction effects restrict the smallest diameter of a particle picture to $d_{\text{diff}} = 2.44\lambda(1 + M)f\#$ which allows to calculate an acceptable approximation of the resulting particle image diameter with the Euclidean sum:

$$d_\tau = \sqrt{(M d_p)^2 + (d_{\text{diff}})^2} \quad (56)$$

The objective captures light from a point source ($d_p \rightarrow 0$) or distant object ($M \rightarrow 0$), which is distributed across a tiny area known as the Airy disc. The diameter of the disc is d_{diff} , and it is enclosed by diffraction rings that decrease in brightness. For common optical parameters in PIV, $d_{\text{diff}} \gg M d_p$ and, consequently, $d_\tau \approx d_{\text{diff}}$ and this is true also for our case. The particle image generated by PIV systems is often dominated by the diffraction limit, and despite fluctuations in d_p , the particle image diameter is very consistent. The goal is to achieve a magnification factor near to 4 which allows to have a particle size of 3 pixels. In order to achieve optimal results for each measurement, the $f\#$ is adjusted to provide the desired magnification factor for the required FOV. The $f\#$ is computed using the d_τ formula, which takes into account the particle size and sets the number of pixels per particle at 3. The two components of the flow velocity within the planar field defined by the light sheet can be determined through two simultaneous images. Furthermore, a high tracer particle density and uniform distribution within the observed flow zone are necessary for accurate readings. MATLAB-based particle image velocimetry (PIV) analysis program open-PIV is used to examine the captured images on a digital computer. In simple terms, this is a cross-correlation analysis of the particle-image patterns in the interrogation regions—small sub-domains present between the first and second image frames. The local fluid velocity is obtained by dividing the displacement of the particle-image pattern by the image magnification and the interval between laser light pulses. This procedure generates the instantaneous velocity in a plane cross-section of the observed flow and is repeated for the whole picture domain. The synchronisation between the camera and the laser is possible thanks to an Arduino system which detects the signal of the laser 1 trigger and the laser 1 Q-switch and activate the camera. The whole system is controlled by the laser1 which internally trigger the laser 2 with a delay set by the experiment parameters. This delay is the flashlamps delay time, which is the time between the lamps flashing of the two lasers, and is calculated by the formula:

$$\Delta t = \frac{H_w d_{px}}{4WM} - 5 \quad (57)$$

where H_w is the height of the interrogation window, d_{px} is the pixel pitch, W is the flow velocity in the wind tunnel and M is the magnification factor. The reason of subtracting $5\mu s$ is due to the Q-switches interval time between each other. The interrogation window height is usually 16, but in case of the smaller FOV we need to use higher values due to the limit of the Arduino system, which delay don't permit to go lower than $15\mu s$.

3.2.2 Measurement devices

The parts of the PIV apparatus that make it possible to carry out the tests are shown below.

Wind tunnel: The wind tunnel section used for this PIV system is 90 x 110 millimeters in size, square shaped, and is ventilated with a fan to provide airflow, model CK AC Ostberg. The fan model employs a Micatrone

measurement probe to estimate volume flow which before the fan measure the pressure difference and compare it with the ambient pressure. The parameters applied are for 20°C and 10113 Pa atmospheric air. The calculation of the volume flow rate and velocity is as follows:

$$v = K_m \sqrt{\Delta p} \quad (58)$$

$$Q_v = A K_m \sqrt{\Delta p} \quad (59)$$

where the probe flow rate constant is $K_m = 7.93$. The measurement error is $\pm 3\%$.

Test section: In order to provide visual access to the particle, a portion of the wind tunnel section was removed. The new test section is composed of three main components: the Plexiglas structure that allows the particles to be seen from the outside, the test bed, shown in the Figure 47, that holds five plates, and the two adapters in the Figure 46 that are required to attach the new test section to the wind tunnel structure. The test section design can be observed in the image. All three components of Plexiglas facilitate the rotation of the vertical axis to get full FOV and boundary layer measurements. Epoxy glue was used to join the three pieces of Plexiglas, which obscures the view when measuring the boundary layer. Additionally, the Plexiglas causes a lot of reflections on the laser sheet, which lowers the results' resolution.

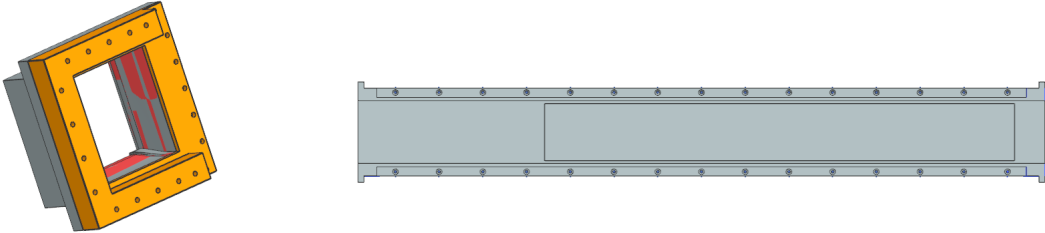


Figure 47: Test section test-bed version 1.

Figure 46: Test section adapter version 1.

Smoke machine: A small smoke generator is utilized to inject reflecting tracking particles into the wind tunnel. The smoke machine produces particles with a diameter ranging from 0.3 to 0.5 μm using a glycol solution. Before the fan, a hole in the wind tunnel frame allows the machine to inject the particles.

High-speed camera Chronos 2.1: The Chronos 2.1-HD can capture video at 1000 frames per second in 1080p and up to 100,000 frames per second at lower resolutions. The camera is shown in Figure 49. Accurate analysis of even the most intricate movements or activities is ensured by its high-resolution sensor and sophisticated image processing algorithms. The sensor type is a CMOS image sensor with 1920 x 1080 pixels and 1000 frames per second, and its specifications are displayed in the Figure 48:

IMAGE SENSOR	
Resolution	1920x1080 @ 1000FPS maximum
Speed	2.1Gpx/s
Dimensions	19.2 x 10.8mm (4/3" format, 2.1-Megapixel, 2x Crop Factor)
Pixel Pitch	10um
Sensitivity (ISO)	Color - ISO 500 to 8000 Mono - ISO 1000 to 16000
Shutter	Electronic global shutter, 1/fps to 10us (1/100,000 s)
Dynamic Range	10.3 stops (62.4 dB)
Bit Depth	12-bit



Figure 49: High-speed camera Chronos 2.1-HD.

Figure 48: Chronos 2.1 sensor specifications.

The shatter gating mode is used to record, and it uses signals from the Arduino to begin recording and open the shutter as required.

Optical lenses: One spherical and one cylindrical lens developed specifically for the system by THORlab. The

minimum focus distance from the test rig is 21,74 mm, which is determined using the following formula:

$$d_m = f_1 f_2 \left(\frac{1}{f_1} + \frac{1}{f_2} - \frac{1}{f_{eq}} \right) \quad (60)$$

f_{eq} is the equivalent focal length of the combined lens system. The distance between each lens is calculate knowing that $f_1=40$ mm and $f_2=500$ mm, which means that the total of the lens focal lengths is 460 mm. Although the first lens may be positioned at any distance, it is actually 7 mm from the laser shutter due to the restricted area of the lenses' support structure.

Laser Nano S 65-15 PIV: The Nano PIV series lasers are specifically designed to be used as Particle Imaging Velocimetry (PIV) illumination sources. Two pulsed and Q-switched Nd:YAG laser resonators in the system produce infrared laser light at 1064 nm, which is transformed by a Harmonic Generation Assembly (HGA) into visible 532 nm laser light. The 1064nm laser beams are merged using polarisers before to the HGA in order to guarantee that both laser outputs may be used with a single set of external optics. The laser structure is shown in the Figure 50. Two separately powered and triggered resonators are used to provide a double pulse output, with complete control over the intervals between pulses. The interface and control electronics for the two laser resonators, the harmonics, and the cooling system are located in the laser system control section. Through the use of an RS232 serial interface, the laser's operating is monitored using the Litron Universal Control interface (LUCi), a touchscreen remote. The laser head features two independent laser oscillators and optics for 1064nm and 532nm light, mounted on an aluminum base plate. It includes a single-rod stable oscillator for uniform light sheets, essential for particle measurement applications. The Nd:YAG rod is pumped by a flashlamp with a stabilized power supply and Q-switching via a KD*P Pockels cell. Safety is ensured by a monitored mechanical shutter linked to interlock circuits. The system uses polarization-based optics to align beams through a thermally stabilized 532nm harmonic generation assembly. A motorized attenuator allows precise energy adjustment without affecting other settings.

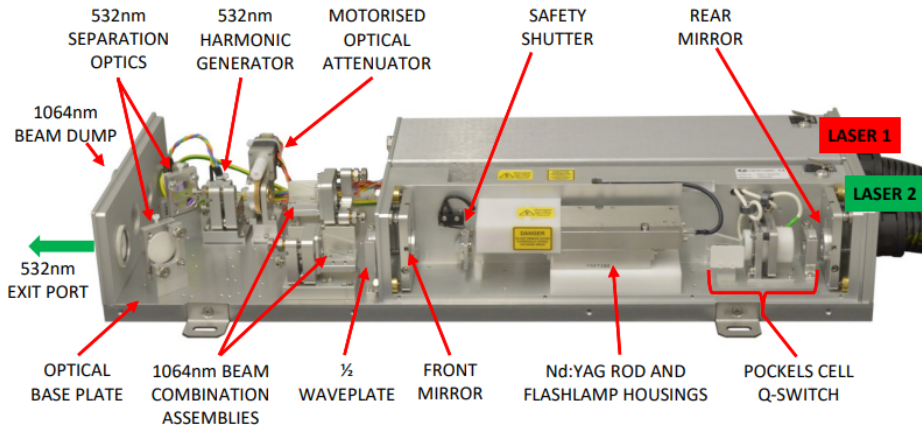


Figure 50: Nano PIV Laser Head Internal Components

The Nano PIV series use an integrated PIV power supply (LPU450), which provides all control, power, and cooling needs for the two laser oscillators and 532nm generation within a standalone unit.

Synchronizer: Arduino board is employed to synchronize of the camera and the laser system. The Arduino Uno is a widely utilized microcontroller board which is based on the ATmega328P microcontroller and offers 14 digital input/output pins, six of which can be used as Pulse Width Modulation (PWM) outputs, and six analog input pins. The Arduino board is connected with 2 pins to the camera to control the shutter and the recording signal and with 2 pins to read the signals of the trigger and Q-switch of laser 1. So the camera start recording when the Arduino code is computed and when the Arduino detects the laser 1 trigger the camera shutter open and again when the laser 1 Q-switch is detected the shutter closes. Then we apply a 2 seconds delay to open the shutter again to get the second frame and 10 seconds to close it again and after 1000 loops it stops recording. This system has limits due to the delay of the signals reading and writing of the Arduino, for this reason the Δt cannot go below 15 μ s. A flow diagram of the system connection is shown in the Figure 51.

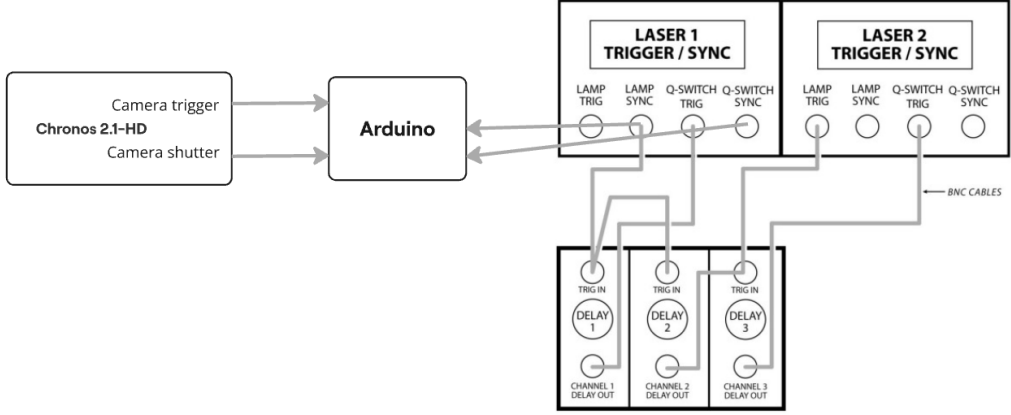


Figure 51: Scheme of the Arduino connections.

3.2.3 Post processing

After the capture of 2000 frames, the images are post-processed employing the OpenPIV-MATLAB open-source MATLAB package for particle image velocimetry (PIV) data analysis. The images are filtered before visually to see if some of the frames were skipped due to the Arduino delay. The PIV raw images acquired are imported into MATLAB, where the user specifies the main PIV parameters. These parameters include:

- Scale (i.e., pixels/meter) for magnification
- Time interval (Δt) between laser pulses
- ROI for the PIV analysis
- Interrogation window size and spacing/overlap size (pixels)
- Filters (i.e., signal-to-noise ratio (S/N) type and threshold, and an outlier velocity threshold)

The images are pre-processed creating a background image to delete the reflections and noises due to the plates and Plexiglas. Using a cross-correlation method, the OpenPIV correlates two successive PIV pictures to produce a displacement vector map. Using the Δt and magnification (scale), the output data in displacement pixels is translated to physical units (meters/second). Square or rectangular sub-image interrogation windows are subjected to the cross-correlation method. OpenPIV processes pairs of PIV pictures using an FFT-based cross-correlation technique to produce velocity field maps, thus sizes are usually $2n \times 2n$. The spatial resolution of the grid x, y at which we estimate the horizontal and vertical velocity components (u, v) is controlled by the spacing/overlap value. Greater resolution is achieved at the expense of decreased background noise when the interrogation window is larger. The optimized interrogation window size is usually 16 bit in case of boundary layer measurements, where the velocities are very low near the wall we need to use higher interrogation windows. The interpolation method chosen is the 2D Gaussian interpolation which is proven to be the most efficient [55]. Some examples of the velocity map are shown in Figure 52.

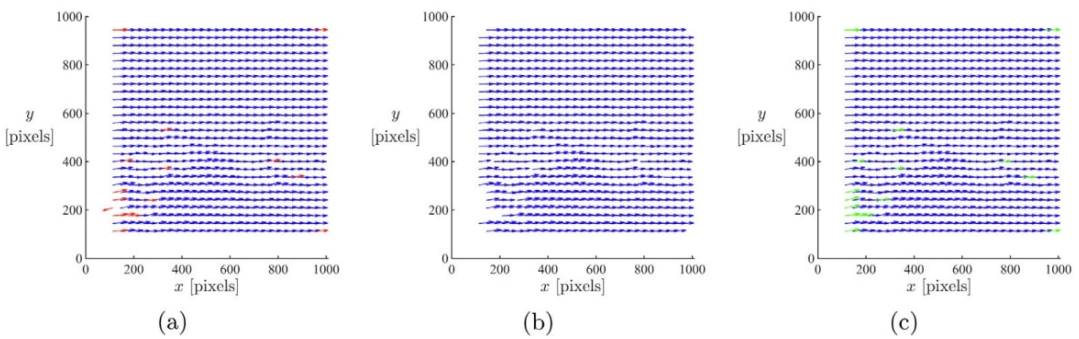


Figure 52: Some samples of the velocity vector map files that were produced in MATLAB as a result of the OpenPIV analysis: (a) raw, (b) filtered, and (c) interpolated, in that order. Interpolated vectors are colored green, whereas outlier velocity vectors are colored red.[10]

The calibration image is taken before the test start positioning a ruler on the outer Plexiglas layer which is previously aligned with the laser sheet. The delta T used in the calibration step is equal to the flashlamp delay adding the Q-switch interval time. A velocity validation is used to apply a local filter on small neighborhoods

of vectors, eliminating vectors that are more than three times the local standard deviation away from the local mean of the eight nearest neighbor vectors to get less than 5–10% incorrect vectors. Following the removal of the outliers, iterative interpolation is used to fill in the missing values using the legitimate neighborhood vectors. The last step of the post processing is the calculation of the cross-correlation coefficient which which establishes if two successive PIV velocity maps match. The two velocity maps are identical (completely matched) if $C_s = 1$, but $C_s < 1$ if the two pictures differ. For each interrogation window, the cross-correlation coefficient is calculated using the following formula:

$$C_s(x, y) = \frac{\sum_{i,j} I_1(x + i, y + j) \cdot I_2(x + i, y + j)}{\sqrt{\sum_{i,j} I_1(x + i, y + j)^2} \cdot \sqrt{\sum_{i,j} I_2(x + i, y + j)^2}} \quad (61)$$

where the intensity levels in the first and second photographs are denoted by (I_1) and (I_2) , respectively. The window location is represented by (x) and (y) and the summation is over the window pixels. The displacement vector is provided by the best match, which is indicated by the cross-correlation function's peak. The cross-correlation coefficients with regard to the velocity vector components (C_u, C_v) or the cross-correlation coefficients with respect to the velocity fluctuations vector components ($C_{u'}, C_{v'}$) should be computed here by substituting (u', v') for s . Any instantaneous PIV velocity map's spatial shift (X, Y) is calculated using overlap to provide the highest correlation coefficient. We can see the difference from a preprocessed image and a postprocessed image comparing the Figure 53 and 54.

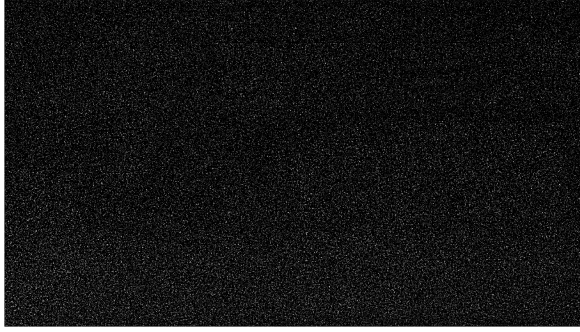


Figure 53: OpenPIV preprocessed image with high-pass filter and background image subtraction.

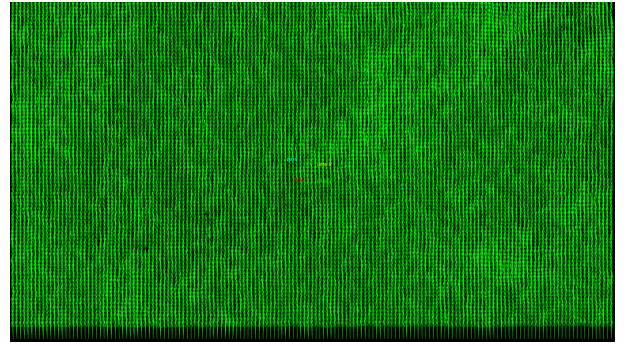


Figure 54: OpenPIV post-processed image using FFT algorithm.

4. Uncertainty analysis

4.1. Introduction to uncertainty analysis

Because physical quantities are inherently inaccurate, it is impossible to obtain exact measurements in experimental study, for this reason uncertainty analysis offers the experimenter a logical means of assessing the importance of the scatter on repeated trials [56]. The Monte Carlo Method (MCM) and the Taylor Series Method (TSM) are the main techniques used to assess these errors. The MCM is the process of assuming several inputs variable distributions in order to obtain an output distribution and its associated uncertainty. As an alternative, the TSM ignores higher-order terms and instead depends on computing the derivatives of the measured physical quantity about the influencing variables [57].

$$X = X_{\text{best}} \pm \delta_x \quad (62)$$

It is frequently unknown what the true value X_{real} is when measuring a physical quantity X . Even more errors arise from the measurement attempts. Consequently, the most precise value that can be given is the best estimate, X_{best} , together with an accompanying error δ_x that indicates the likely interval of the measurements, where the X_{real} is certainly included, even if that itself remains unknown, despite the number of measurements taken. For several measurements, the best estimate is represented by the average of the measurements:

$$X_{\text{best}} = \bar{X} = \frac{\sum_{i=1}^N X_i}{N}, \quad X_{\text{real}} \neq X_{\text{best}} \quad (63)$$

When only a single measurement is available, the instrument's uncertainty dictates the error, and the most accurate estimate corresponds to the measured value. The two main categories of errors are systematic and

random.

Systematic errors: The inaccuracies are inherent in measurement tools and cause a persistent bias in estimating the physical amount. The more accurate the device, the smaller the error.

Random errors: These mistakes are related to either the measurement instrument's intrinsic uncertainty or how the operator carried out the experimental investigation. To assess random mistakes, statistical techniques are usually used, particularly in cases when there are a lot of measurements.

$$X = X(\alpha_1, \alpha_2, \dots, \alpha_N) \quad (64)$$

The complexity of error calculation grows with the number of affecting variables, and each of these comes with an error and therefore have an impact on the results.

4.2. Uncertainty results for the Surface Roughness Heat Transfer rig

4.2.1 Smooth surfaces uncertainty analysis

For smooth surfaces, since so many factors affect the outcome the MCM was chosen. Figure 55 shows the overall contributions to HTC uncertainty, as well as the individual uncertainties' propagation throughout the

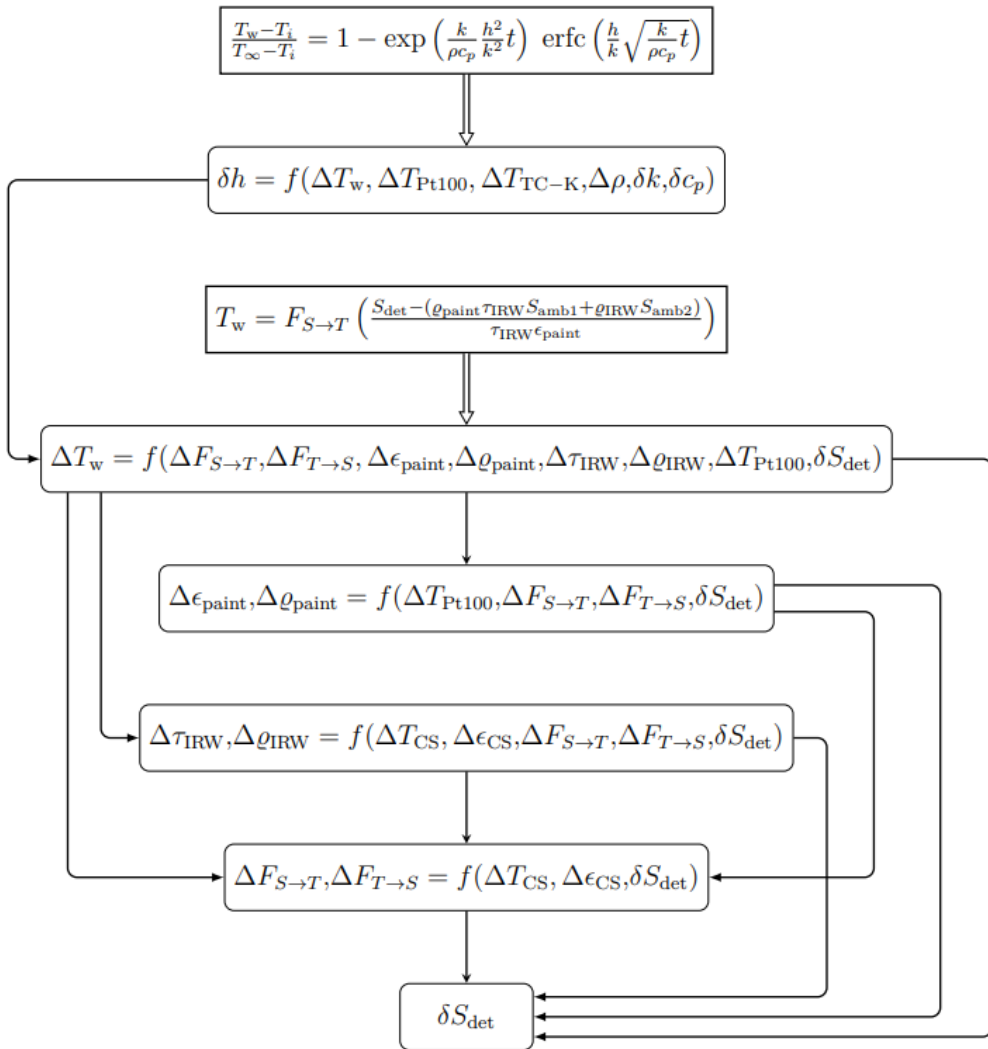


Figure 55: Flowchart of the uncertainty contributions

intermediate steps. To do this, a representative PDF of the physical quantity is obtained by performing M iterations from each of the N distributions, from which statistical quantities like mean, standard deviation, and confidence intervals can be obtained. The confidence interval, which covers 95% of the measured values, is often calculated as twice the standard deviation. The final result is presented with the output distribution's standard deviation as the error.

$$h = \bar{h} \pm \sigma \quad (65)$$

One important quantity that has an impact on the final HTC derivation, as seen from the flowchart, is the wall temperature and the uncertainty concerning it. Lehmann [53] provided the paint and window optical property distributions, which are utilized as inputs to calculate the wall temperature uncertainty, here reportend in Table 6.

Property	μ [-]	2σ [-]	Rel. Uncertainty [%]
$\varepsilon_{\text{paint}}$	0.9072	0.0274	3.020
ρ_{paint}	0.0540	0.0094	11.48
τ_{IRW}	0.9489	0.0334	3.412
ρ_{IRW}	0.0501	0.0068	13.57

Table 6: PDF properties for paint and IRW

Furthermore, according to the IR camera manufacturer, the observed radiometric signal S_{det} has an error of $\delta S_{\text{det}} = 1\%$. Each position along the test section undergoes $M = 10^5$ iterations during the process, where only a single pixel's time history of the digital level at the centre of each region of interest is captured, for each Reynolds. The output distributions' resultant uncertainty δh , mean μ , and confidence level 2σ are given.

Position	Re=10000			Re=15000		
	$\mu \left[\frac{W}{m^2 K} \right]$	$2\sigma \left[\frac{W}{m^2 K} \right]$	$\delta h \left[\% \right]$	$\mu \left[\frac{W}{m^2 K} \right]$	$2\sigma \left[\frac{W}{m^2 K} \right]$	$\delta h \left[\% \right]$
1	12.18	1.69	6.95	17.83	2.34	6.56
3	10.74	1.58	7.35	16.63	2.42	7.29
5	10.34	1.51	7.29	14.28	1.94	6.85
7	10.90	1.51	6.90	15.34	2.12	6.91
9	9.51	1.24	6.64	15.10	2.13	6.97

Table 7: Uncertainty results for Reynolds 10000 and 15000

Position	Re=20000			Re=25000		
	$\mu \left[\frac{W}{m^2 K} \right]$	$2\sigma \left[\frac{W}{m^2 K} \right]$	$\delta h \left[\% \right]$	$\mu \left[\frac{W}{m^2 K} \right]$	$2\sigma \left[\frac{W}{m^2 K} \right]$	$\delta h \left[\% \right]$
1	21.58	2.92	6.94			
3	21.46	3.09	7.17	21.93	2.92	6.68
5	20.51	2.93	7.22	19.85	2.69	6.72
7	17.42	2.52	7.42	20.24	2.81	6.93
9	17.83	2.42	6.81	19.45	2.89	7.39

Table 8: Uncertainty results for Reynolds 20000 and 25000

4.2.2 Rough surfaces uncertainty analysis

The uncertainty for rough surfaces depends on multiple parameters, making a single method like the MCM insufficient. A way to approach this could be applying both methods together, however, due to the extent that that process would have, it would require separate research. Hence, for the purposes of this thesis, this chapter will provide a brief report on the measurement uncertainties related to rough plates. The test object has been obtained by measuring the real material surface roughness parameters with a Stylus-Profilometer, visible in Figure 57.

R_a [μm]	R_q [μm]	R_z [μm]	R_p [μm]	R_v [μm]	R_{sk}	R_{ku}
5.89 ± 0.28	7.44 ± 0.28	36.62 ± 1.05	20.20 ± 0.54	16.42 ± 0.60	0.218 ± 0.08	3.47 ± 0.36

Table 9: Roughness parameters of the real-size rough surface

In stylus profilometry, the surface profile of a sample is recorded by drawing a fine-tipped stylus, typically composed of diamond or another hard material, across a straight line on the sample's rough surface. A controlled force is applied to the stylus in order to keep it in consistent contact with the surface. The stylus travels vertically along the sample's surface as a result of the shapes it touches. A transducer, often using piezoelectric technology,

transforms this vertical movement into an electrical signal. The signal contains comprehensive topographical data about the surface, such as ridges, valleys, peaks, grooves, and overall roughness. An aluminum channel was split to reveal the inside surface as seen in Figure 56, and one half was used for profiling. The measurements were taken in six distinct lines, each measuring 4 mm.

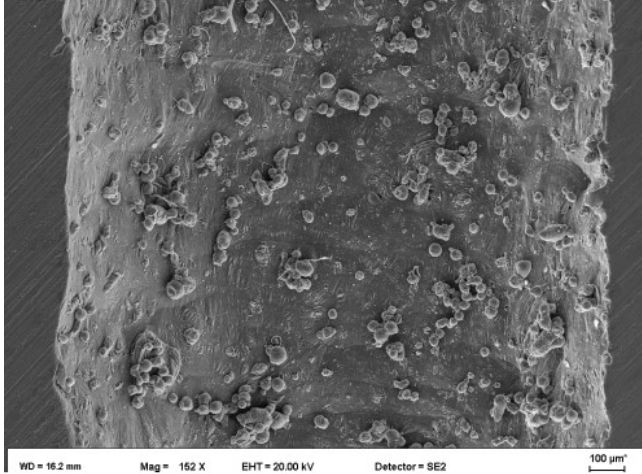


Figure 56: SEM image of the internal section of the Aluminium cooling channel.

Table 9 displays the computed mean values together with the related errors. The error values were estimated using the standard deviation of the mean, as shown in Equation 66. Figure 58 shows the uncertainty elated to the measurements and the average value used to get the analogue correspondent parameter, their error, mean and standard deviation are displayed in Table 10.

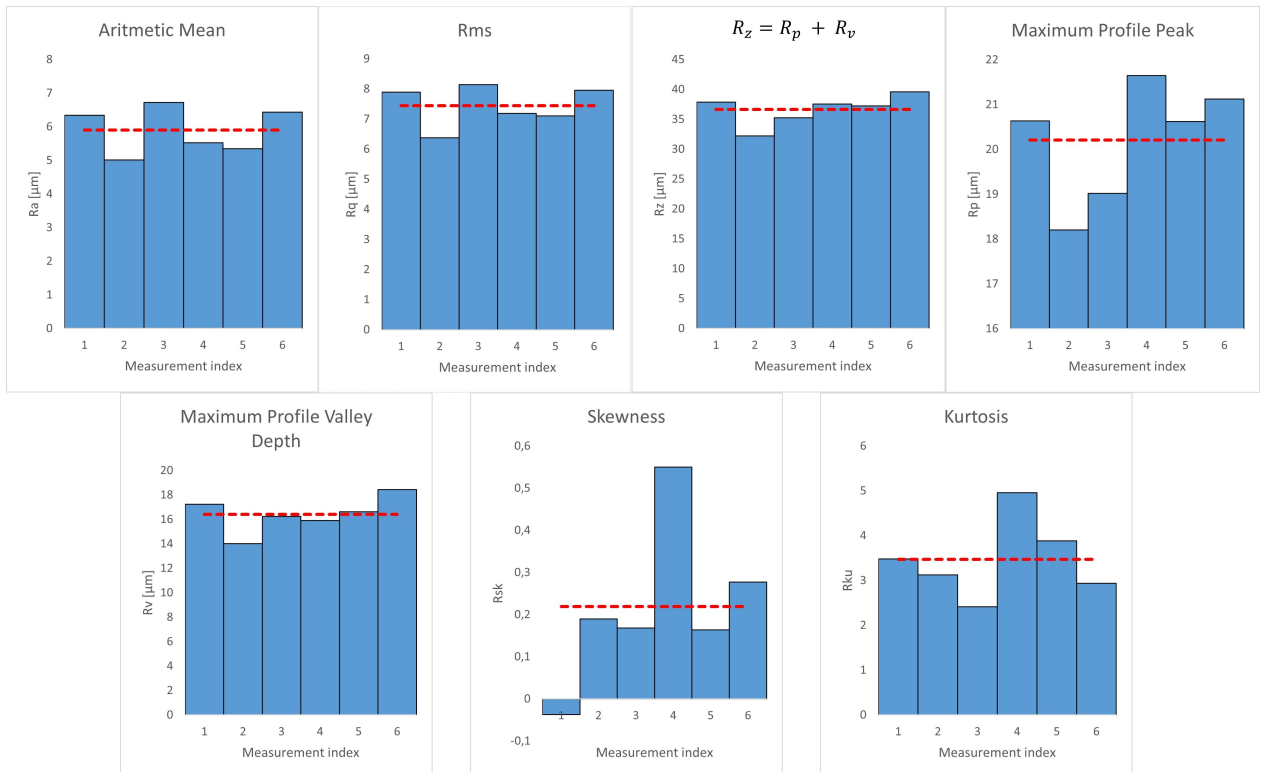


Figure 58: Measurements for each of the surface roughness parameters and average results.

After the SEM picture is evaluated, the diameters of the spherical rough elements are measured by hand using a particular scale that is shown in the Figure 56's lower right corner. To find the proper statistical distribution, all measured diameters are corrected using an upscaling factor s , and combined into a single vector.

Test	R_a [μm]	R_q [μm]	R_z [μm]	R_p [μm]	R_v [μm]	R_{sk}	R_{ku}
ERROR	11.73%	9.06%	7.00%	6.52%	9.01%	87.95%	25.49%
MEAN	5.897	7.447	36.623	20.209	16.414	0.219	3.468
STDEV	0.692	0.675	2.562	1.318	1.480	0.192	0.884

Table 10: Error, mean and standard deviation for the measured Roughness Parameters

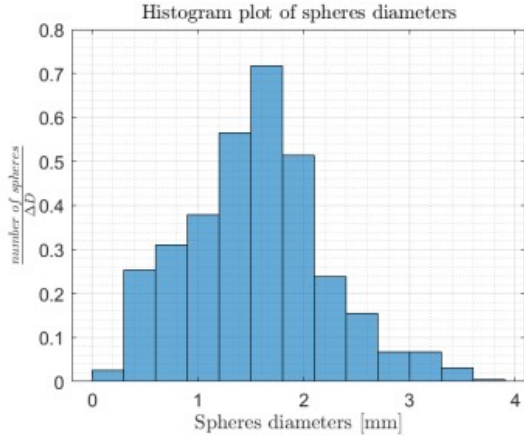


Figure 59: Measured spheres diameters

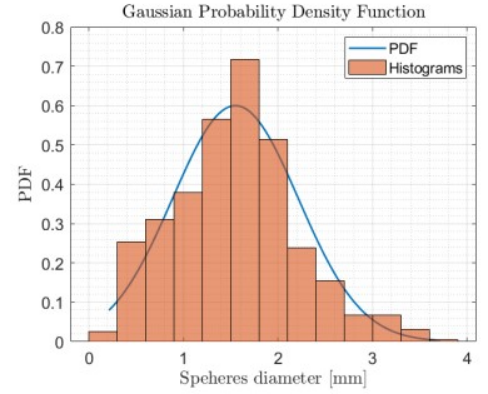


Figure 60: Normal PDF for upscaled diameters

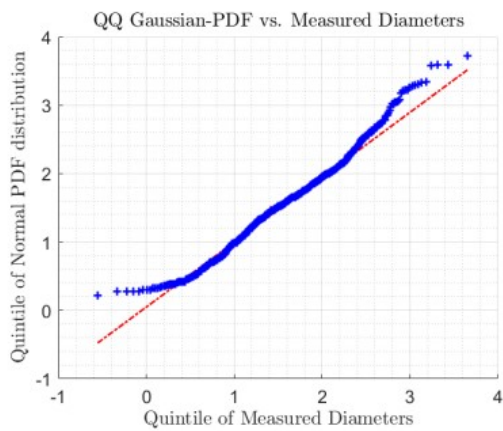


Figure 61: QQ plot Normal PDF

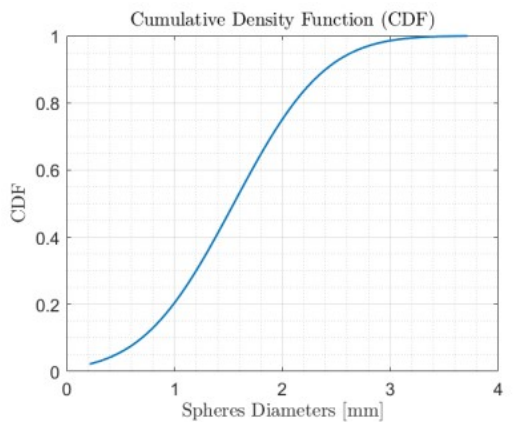


Figure 62: Cumulative density function

Figure 63: Statistical properties used to obtain the rough surface

$$S_x = \sqrt{\frac{\sum_{i=1}^N (x_i - \bar{x})^2}{N(N-1)}} = \frac{S_x}{\sqrt{N}} \quad (66)$$

The standard deviation and average values for the diameters that were measured manually are respectively $\sigma = 0.66 \text{ mm}$ and $\mu = 1.55 \pm 0.03 \text{ mm}$. The histogram shown in Figure 59 is accompanied with a Normal Probability Density Function PDF that shows the diameter distribution, as seen in Figure 60. With the exception of a few outliers at the extremes, the projected values in the Quantile-Quantile plot shown in Figure 61 nearly match the measured data, indicating an excellent fit with the Normal distribution. Furthermore, Figure 62 displays the Cumulative Density Function, which shows the likelihood that a diameter will fall inside a given range. CDF values are always non-negative, and there is about a 55% chance that a spherical rough element will have a diameter of between 1 and 2 mm. As a result, this range contains more than half of the spheres on the analogue rough surface.

4.3. Uncertainty results for the Particle Image Velocimetry rig

PIV measurements may include errors at different phases along the measurement chain, such as the particular flow facility employed, the experimental equipment setup, the image recording procedure, and the data assessment methods selected as the Figure 64 shows. Errors occur because of installation and alignment and

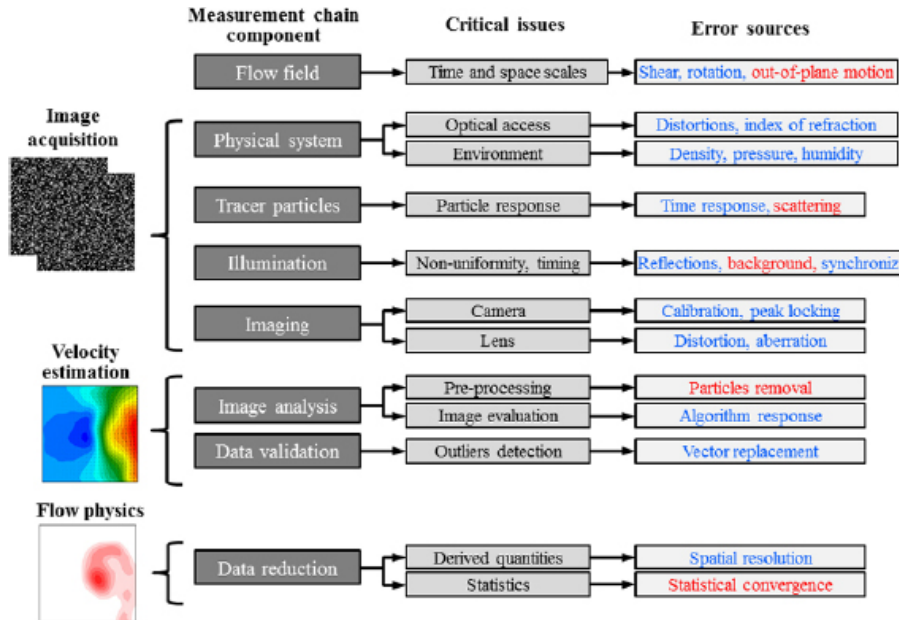


Figure 64: Schematics of the primary PIV measurement chain elements and the most important sources of uncertainty.

they have a huge impact because the planar PIV measures the projection of the flow velocity vector onto the measuring plane. Systematic errors result from the velocity projection not matching the flow components of interest if the measurement plane is not correctly aligned with the intended flow direction. Moreover, improperly calibration procedure bring inaccuracies into the calibration process. In the examined case the calibration is done manually considering the test section parallel to the wall and taking a picture of a ruler and processing it in the OpenPIV software. A comprehensive study of the timing problems with a variety of commercially available Q-switched Nd:YAG and Nd:YLF lasers was carried out by Bardet et al. [58]. All of the examined lasers' timing problems were discovered to be primarily systematic, with very little random error; a system's error up to 50 nanoseconds. For measurements in low-speed flows, like the one in our system, these timing inaccuracies may be regarded as insignificant. The measurement of the laser pulse separation uncertainty, $U_{\Delta t}$, is often dependent on data supplied by the manufacturer or specialized experiments. It cannot be derived from data statistics on repeated observation [58] so it can be specified by the manufacturer. In most cases, $U_{\Delta t}$ is in the order of 1 nanoseconds and in our case is equal to 0.5ns [59], which is insignificant relative uncertainty for most experiments. In this instance, the manual states is equal to 0.00002. Local flow velocity (u) at a point (x, y) is calculated by measuring the displacement (ΔX) of a set of tracer particles over a brief time interval (Δt). This displacement can be expressed using the magnification factor M , which enables the conversion of the object space displacement (Δx) to the image plane displacement (ΔX):

$$u = \frac{\Delta x}{\Delta t} = \frac{\Delta X}{M \Delta t} \quad (67)$$

Using Taylor series propagation, the predicted velocity's uncertainty is calculated with M , Δt , and ΔX acting as independent variables [60]:

$$\left(\frac{U_u}{u} \right)^2 = \left(\frac{U_{\Delta X}}{\Delta X} \right)^2 + \left(\frac{U_{\Delta t}}{\Delta t} \right)^2 + \left(\frac{U_M}{M} \right)^2 \quad (68)$$

The magnification uncertainty $U_{\Delta M}$ was recently evaluated in greater detail by Campagnole dos Santos et al [61]. They calculated the magnification uncertainty as the sum of four contributions: (i) the uncertainty of the dot position and size due to the calibration plane's manufacturing limits; (ii) the image distortion caused by perspective errors; (iii) the misalignment between the calibration plate and measurement plane; and (iv) the misalignment between the calibration plate and camera plane. However, when the calibration is done correctly,

the displacement element in equation $U_{\Delta X}$ dominates the overall uncertainty, making the magnification and calibration errors negligible. We require an uncertainty model that shows how any SNR(signal-to-noise ratio) measurements relate to the standard uncertainty. Therefore, the fitting parameters of the following equation are determined in order to compute the estimated standard uncertainty:

$$u^2 = \left(M \exp \left(-\frac{1}{2} \left(\frac{\phi - N}{s} \right)^2 \right) \right)^2 + (A\phi^B)^2 + (C)^2 \quad (69)$$

In order to account for the uncertainty caused by invalid measurements, the first term is a Gaussian function, where the distribution of the real velocity within the sampled flow field and the range of potential velocity measurements both affect the precise value of M. N is the theoretical lowest value of the measured metric, and the $(\phi-N)$ term enables the uncertainty to increase quickly when the metric's value gets closer to a tiny number. We can calculate the appropriate value of N for each quantity analytically based on its specification. For PPR, the minimum value is 1 when we have a primary peak and secondary peak with the same height. Equation 69 second component, the contribution to uncertainty by the valid vectors, indicates that, if the given measurement can be guaranteed to be valid, then A would largely dictate the maximum amount of uncertainty that may be anticipated. The final element, C, represents the lowest level of uncertainty that may be attained and is a constant. The influence of background picture noise on the cross correlation plane is efficiently eliminated by subtracting the minimal correlation value from the correlation plane. The criteria of the validity of the results rely on the a new measure of the correlation signal to noise ration which is the Mutual Information(MI). The shape of the peak is dictated by the particle image self correlation and displacement distribution, and the correlation peak height is proportional to the product of the image density NI, the out-of-plane loss of correlation FO, and the in-plane loss of correlation FI. Therefore, the MI is a more general form of the product of these 3 parameters combining the effects of particle intensity and diameter. The MI is defined as the ratio of the ratio of the contribution of all correlated particle pairs and the contribution of one correlated particle pair. The MI is computed by dividing the cross-correlation's peak magnitude by the "mean" particle's autocorrelation, which is determined by the image autocorrelation's diameter [11].

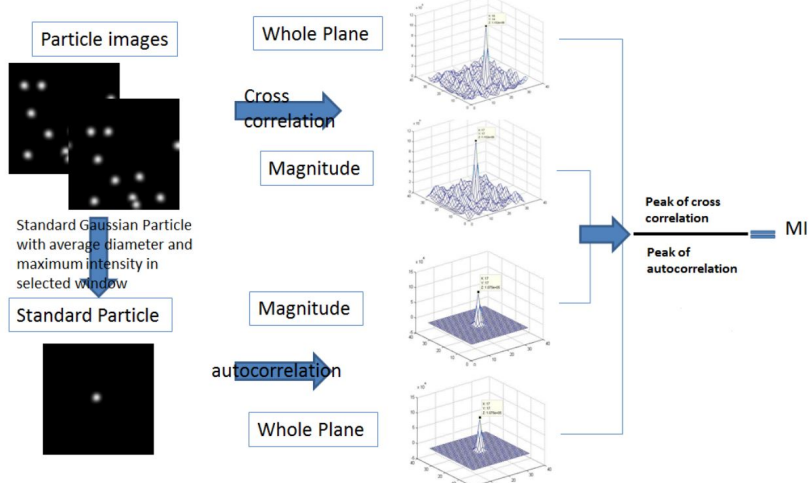


Figure 65: Scheme of MI calculation [11].

The process to calculate the MI is shown in the Figure 66. Therefore, it is possible to estimate the quantity of mutual information (MI) across consecutive frames, or the number of correlated particle pairs, as:

$$MI = \frac{C_{\max}}{A_0} = \frac{\sum_{p_c} \frac{1}{16} J_i^2 d_i^2 \pi}{\sum_{p_c} \frac{1}{16} J_0^2 d_0^2 \pi} \quad (70)$$

where J_i and J_0 correspond to the intensity of the particles and the one of the reference particle respectively and d_i and d_0 represent the diameter of the particles. A three-point Gaussian fit is often used to determine the correlation peak width for a specific correlation plane. The diameter is then computed as four times the standard deviation for that Gaussian distribution. The sub-pixel displacement estimation for the PIV measurement is based on the position of that Gaussian distribution's maximum value. This is predicated on the idea that the main peak region contains the true displacement. Therefore, the measurement should be regarded as valid since the peak corresponds to the real displacement if the error (difference) between the recorded displacement

and true displacement is less than half of the peak diameter. We determine that the measurement successfully identified the correct peak if the error is less than half of the peak diameter.

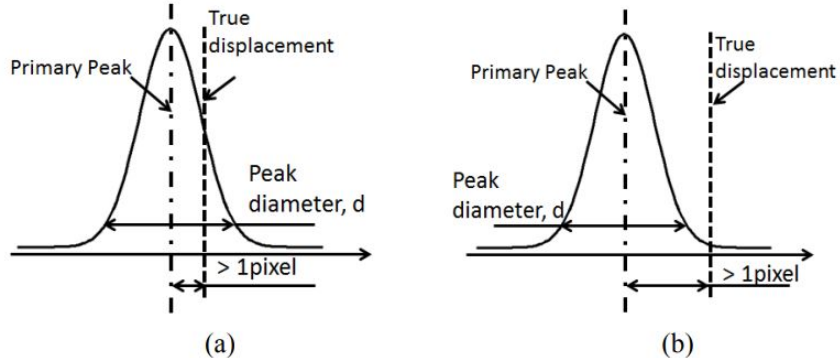


Figure 66: Examples of good measurement (a) and outlier (b) for the half peak diameter criteria [11].

The relations between the measured metrics' value and the uncertainty or error distribution were developed using synthetic picture sets with known displacement information. These images were used to create the model and the curve fitting functions using RPC (Rational Polynomial Coefficient sensor) and SCC (Signal-to-Noise Ratio Correction Mode) method shown below:

$$u_{\text{sc}}^2 = \left(\left(10.47 \exp \left(-\frac{1}{2} (PPR - 1)^2 \right) \right)^2 + (1.913 PPR^{-1.371})^2 + 2.22 \times 10^{-14} \right) \quad (71)$$

$$u_{\text{rp}}^2 = \left(\left(8.825 \exp \left(-\frac{1}{2} (PPR - 1)^2 \right) \right)^2 + (1.642 PPR^{-1.01})^2 + 2.21 \times 10^{-14} \right) \quad (72)$$

The result analyzing 10 frames of center line test with the laser sheet parallel to the smooth plates are shown in the Table 11.

Table 11: Values of uncertainty for parallel measurements on smooth plates.

Uncertainty	Value
u_{rp}^2	0.5837
u_{sc}^2	0.6405

The weighted uncertainty of the 10 frames is shown in the Figure 67 and in the Figure 68 we can see the distribution of the uncertainty for every PPR value.

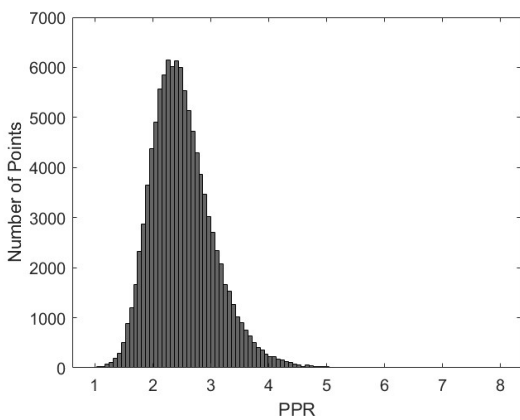


Figure 67: Histogram of uncertainty values obtained with RPC method.

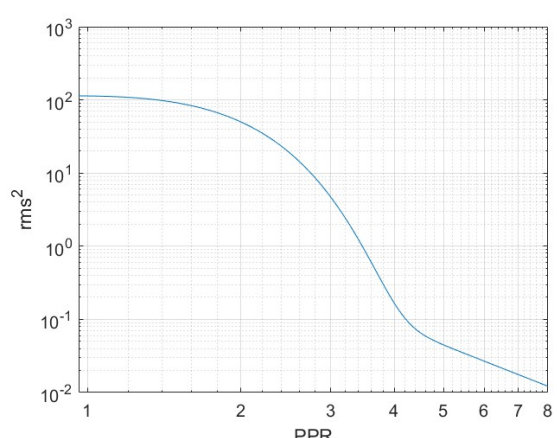


Figure 68: Uncertainty values curve.

The results depends on the reflection which could be checked doing the same procedure on results with the laser sheet perpendicular to the plates. This results can be compared to the one of the tests with the laser sheet perpendicular to the plates in Table 12. In the second case we are testing in the right corner with the plates in the left corner and the reflections should come from mainly from the plates which are painted with black painting which should be less reflective than the green wall which caused the main reflection in the parallel case described before. However, we will have more reflections from the plates due to the their position. Another issue that we have to consider is that in the boundary layer region we have less resolution due to the very low velocity we achieve and the glue presence in the right corner, which can also be another source of reflections.

Table 12: Values of uncertainty for perpendicular measurements on smooth plates.

Uncertainty	Value
u_{rpc}^2	0.3612
u_{scc}^2	0.2839

This model is been tested with single-pass method PIV, but our system employ the multi-pass method which consist in an algorithm that performs multiple passes from large size interrogation window to smaller ones providing greater resolution. Therefore, our analysis should be implemented with synthetic images created with multi-pass method and find another curve fitting function. Another parameter that can affect the results is the seeding density. Regarding the tracking particles, according to Mei [62] and Raffel et al. [63], assuming that the particle motion obeys Stoke's drag law, the slip velocity is determined by the local fluid acceleration and the particle time response, which is connected to the particle's diameter and density differential from the fluid. To maximize tracing capabilities in air flows, heavier liquid or solid tracer particles with sizes ranging from 0.01–2 μm are usually utilized. In our case the tracking particles used are smoke particles which have a diameter that ranges between 0.3 and 0.5 μm .

5. Results

5.1. Surface Roughness Heat Transfer rig

5.1.1 Smooth surfaces

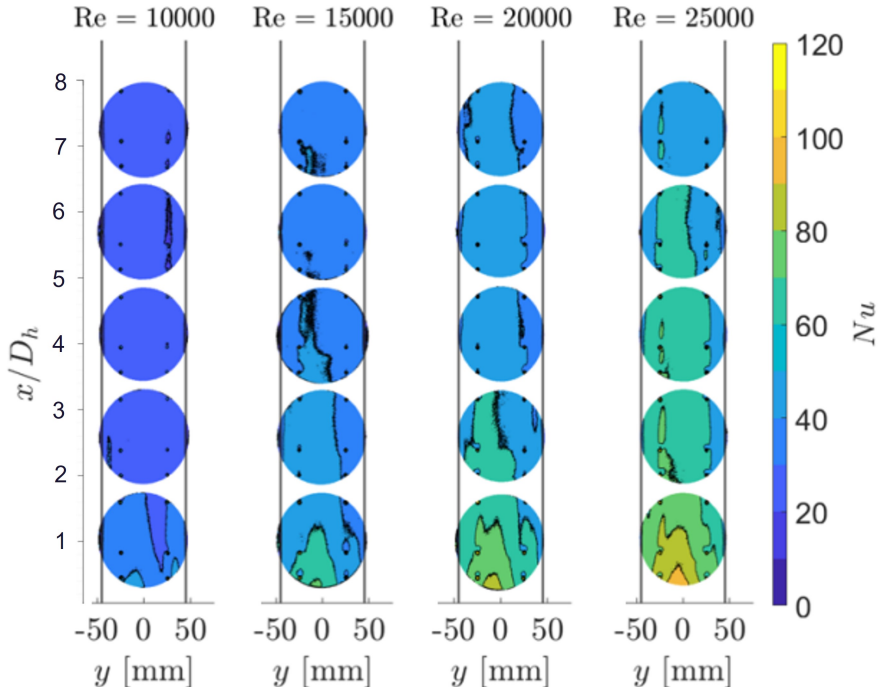


Figure 69: Contour plot over smooth surfaces

The thermal paint-coated plates characterizing the smooth channel have been tested at four distinct Reynolds numbers: 10000, 15000, 20000, 25000.

The lateral average trend in the streamwise direction and the HTC for the entire bottom surface at each window have been described. Additionally in the last window of the channel, where the thermal boundary layer is predicted to be fully developed, a comparison has been made between the Gnielinski correlation for thermally fully developed flows in smooth channels and the Nusselt number obtained by the tests. All results are given in terms of the Nusselt number since it is directly related to the HTC. With the calculations explained in Section 3.1.4, it was possible to obtain the bulk temperature and the wall temperature over the plates, allowing to calculate the HTC distribution, therefore, it has been plotted the Nusselt distribution on every window in Figure 69. The region of interest is evaluated within the channel boundaries, which are shown by the black sidelines. From the channel inlet to the exit, the Nusselt number shows a decreasing trend for a given Reynolds number. On the other hand, a higher Reynolds number corresponds to a higher Nusselt number at a particular location in the channel, suggesting improved heat transfer. This tendency is in line with Lhemann, Wen and Brogliato's previous works [53], [51], [52] and theoretical assumptions. By looking at the laterally averaged Nusselt number along the streamwise direction, as shown in Figure 70, one can see the decreasing trend of the Nusselt number down the channel. A high Nusselt number indicates increased heat transfer rates at the intake caused by the entrance region and the start of the air in flowing inside the test section. But as the thermal boundary layer develops further downstream, the Nusselt number decreases and eventually approaches a plateau. For example, the Nusselt number drops from around 85 in the first window to about 57 in the last window for a Reynolds number of 25,000. The Nusselt number stabilizes along the streamwise direction on this plateau, which represents the thermally fully developed flow condition. With an increase in Reynolds number, this plateau's location moves downstream. However, a small declining trend is noted for the HTC and Nusselt number, which seem to stabilize at $\frac{x}{D_h} = 5$. Since turbulent flow entry lengths are often about 10 diameters from the inlet, it is reasonable to believe that the average Nusselt number for the channel as a whole is close to the value for the thermally fully developed region.

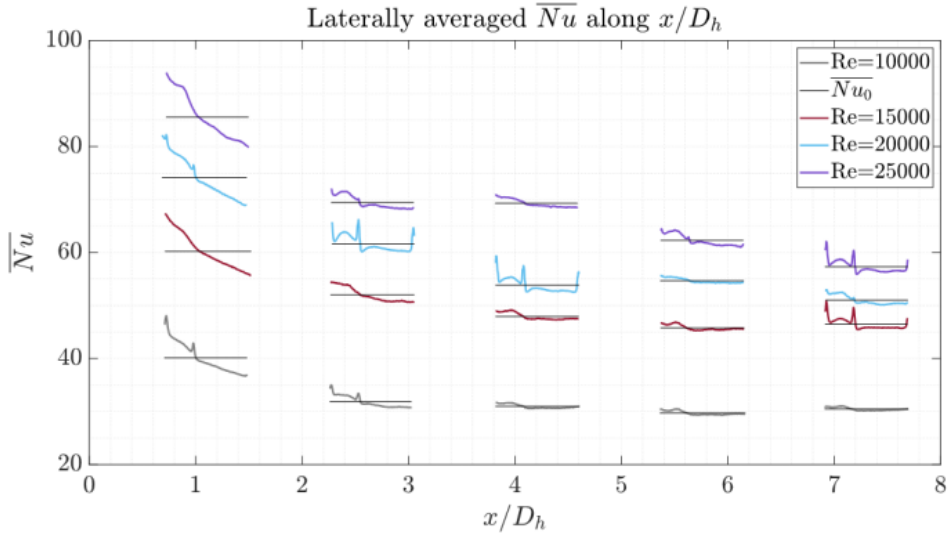


Figure 70: Laterally averaged Nusselt number along the streamwise coordinate

The modest reduction in the Nusselt number seen in the final segment of the channel may be explained by the fact that the channel length in the current investigation is insufficient to reach this fully developed region. In spite of this, the Nusselt number seems to be stable, with only a slight decline anticipated.

5.1.2 Validation of the rig

To validate the experiments, it is required to assess the accuracy of the heat transfer results for the channel in question. This has been accomplished by using the technique Mills proposed for smooth channels. The latter portion of the channel is considered to be within the thermally fully developed zone for the purposes of the analysis. Therefore, one of the well-known correlations found in literature, like Dittus-Boelter or Gnielinski, can be used to compare the globally averaged Nusselt number Nu_0 in this section. These correlations are applicable to fully developed flow conditions. Gnielinski correlation is used in the form that takes into consideration the

distance from the channel inlet:

$$Nu_{\infty} = \frac{(f/8)(Re - 1000) Pr}{1 + 12.7\sqrt{f/8}(\Pr^{2/3} - 1)} \left[1 + \left(\frac{D_h}{L} \right)^{2/3} \right] K \quad (73)$$

where the friction factor f and the coefficient K are obtained using:

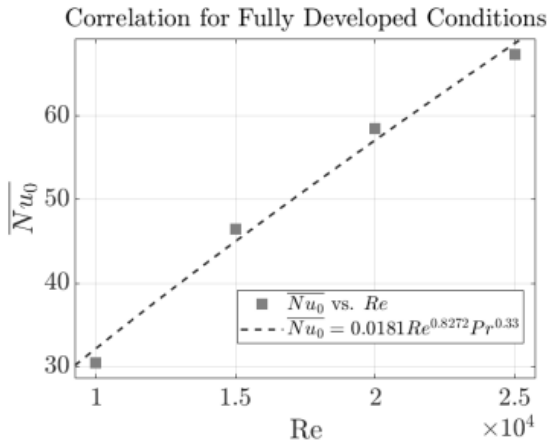
$$f = (1.84 \cdot \log_{10} Re - 1.64)^{-2} \quad (74)$$

$$K = (T_b/T_w)^{0.45} \quad (75)$$

The correctness of our conclusions concerning a channel with fully developed heat transfer conditions is thus indicated by the ratio $\frac{\overline{Nu}_0}{Nu_{\infty}}$ determined for the final segment of the channel, i.e. the last window. Within the range of the tested Reynolds numbers, our results can be considered valid, given that Gnielinski correlation has an uncertainty of approximately 25%. More specifically, the experimental data are consistently within the uncertainty interval but in general they show values that are lower than those found in Gnielinski's results. Utilizing the least squares approach outlined in equation 76, the experimental findings were fitted, producing a 3% mean deviation.

$$\overline{Nu}_0 = K \cdot Re^a \cdot Pr^b \quad (76)$$

A correlation similar to Gnielinski's could not be established since more data points were required, so this one used echoes that of Dittus-Boelter. Figure 71 shows the plot of the least square regression with $R^2 = 0.9887$. In Table 13 we can see that the comparison between an in-literature correlation and the global Nusselt average are within the uncertainties of the correlation.



Re	\overline{Nu}_0	Nu_{∞}	$\overline{Nu}_0/Nu_{\infty}[\%]$
10000	30.46	37.30	18.35
15000	46.47	51.45	9.67
20000	51.01	64.38	20.77
25000	67.40	76.53	11.94

Table 13: Comparison between globally averaged Nusselt and Gnielinski correlation

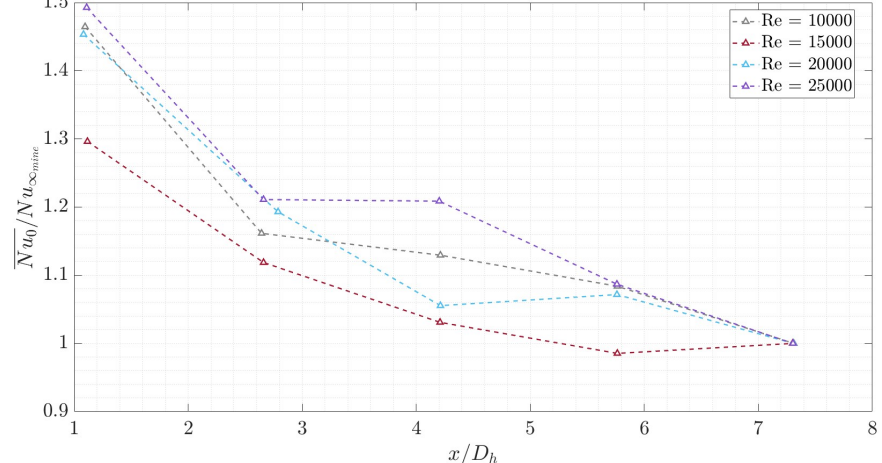


Figure 72: Normalized values along the streamwise dimensionless coordinate

The values of the constants are $K = 0.0181$, $a = 0.8272$, and $b = 0.33$. The only significant exponent is a , since the Prandtl effect is irrelevant for air due to the fact that the Prandtl number remains constant at low temperatures. Its value is consistent with other results for turbulent flows across smooth channels found in the literature, where typically $a = 0.8$ is well accepted. In order to gain a comprehensive understanding of the entrance region effect, it has been plotted for all dimensionless positions $\frac{x}{D_h}$ the ratio of $\frac{Nu_0}{Nu_{\infty \text{mine}}}$ in Figure 72. Because of the abrupt temperature shift, heat transfer is typically high at the entrance ($\frac{x}{D_h} = 0$). Proceeding downstream, the ratio $\frac{Nu_0}{Nu_{\infty \text{mine}}}$ tends to approach unity. The last segment of the channel can be legitimately considered thermally fully developed, even though there might be minor measurement mistakes, these lies within the uncertainty range provided by Gnielinski. It is important to note that the entrance region grows longer for increasing Reynolds values.

5.1.3 Rough surfaces

Thermal paint-coated rough plates have been tested for the same Reynolds numbers as the smooth ones.

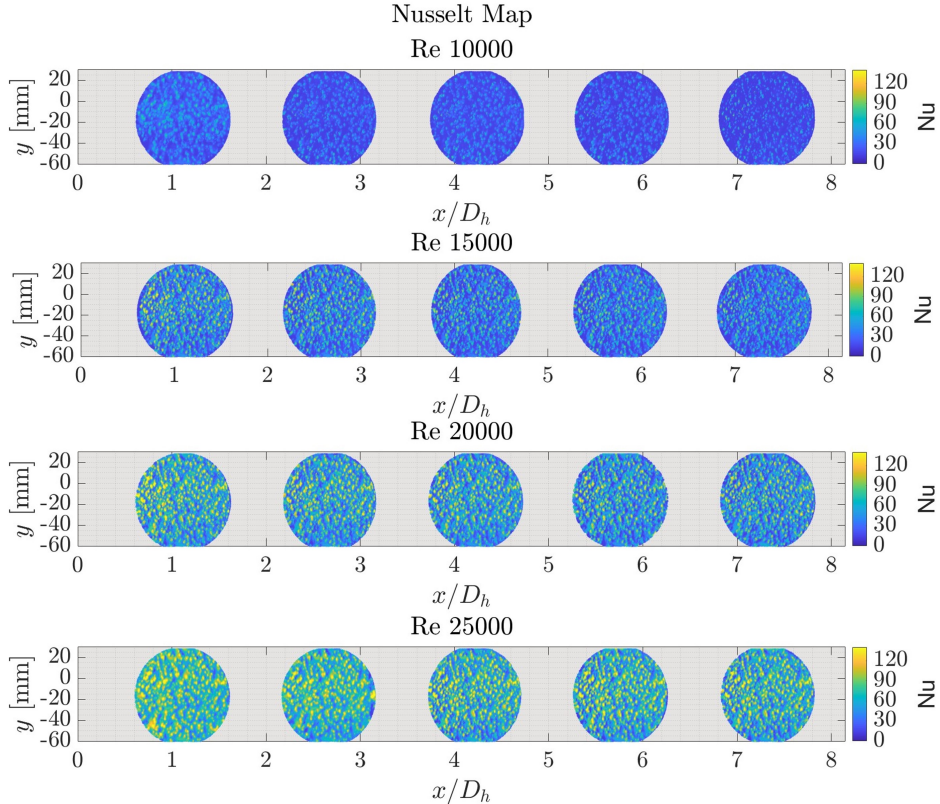


Figure 73: Local Nusselt distribution for different Reynolds number.

The first thing to notice in Figure 73 is that the Nusselt number increases with the increase of the Re . The trend of the channel is decreasing as expected and in the last two windows the Nu stabilizes to a plateau where the flow is fully developed. In the first window the Nu reaches the highest peak, this is the characterization of the entrance region effect, due to the step that the air has to go through once the hatch is opened. The presence of rough components introduces turbulence and direct impact effects, which is reflected in the significant oscillating behavior seen in the Nusselt number distribution across the plate. Comparing this results plot with the one obtained for the smooth surfaces in Figure 70, we can notice that the thermally fully developed region is reached faster thanks to the effect of the roughness. This is in line with recent studies that showed that surface roughness affects flow behavior in microchannels made using different techniques. Rougher surfaces encourage early thermal development because of higher turbulence [64]. The entry region results differ from those of the fully developed flow region. Because streamwise fluctuations in velocity and dimensionless temperature must be taken into account by both the momentum and energy equations, this region is more complicated to analyze. Solutions have been obtained when the thermal and hydrodynamic boundary layers are developing. Plotting the Nusselt number or the Stanton number $St = \frac{Nu}{Re Pr}$ against the reciprocal of the Graetz number, $Gz = \frac{D}{x} Re Pr$, is a common way to illustrate the results in this context. For example, Baehr-Stephan's correlation [65] offers a useful method for combined entry length issues with a constant surface temperature $T_s = \text{const}$ (see Equation

77). In this context, the average value over the designated region is referred to as the Nusselt number.

$$\overline{Nu} = \frac{\frac{3.66}{\tanh(2.264 Gz^{-1/3} + 1.7 Gz^{-2/3})} + 0.0499 Gz \tanh(Gz^{-1})}{\tanh(2.432 Pr^{1/6} Gz^{-1/6})} \quad (77)$$

It should be mentioned that this equation is representative of a specific case and does not directly relate to our research. Nonetheless, it might show a comparable pattern in the behavior of the entry region. We must also consider that the experimental channel in our case, with its rectangular cross-section and one wall out of four being rough, does not precisely replicate real cooling channels. For this reason it is also harder to find a feasible correlation to compare the Nusselt results with the ones of other experimental investigations, because they should have a similar experimental apparatus. One last thing to point out is that a significantly reduced oscillation is observed at a Reynolds number of 10000, the consequences of this observation will be discussed in upcoming sections of this work. The local effects given by the roughness elements can be seen in the Nusselt map reported in Figure 73.

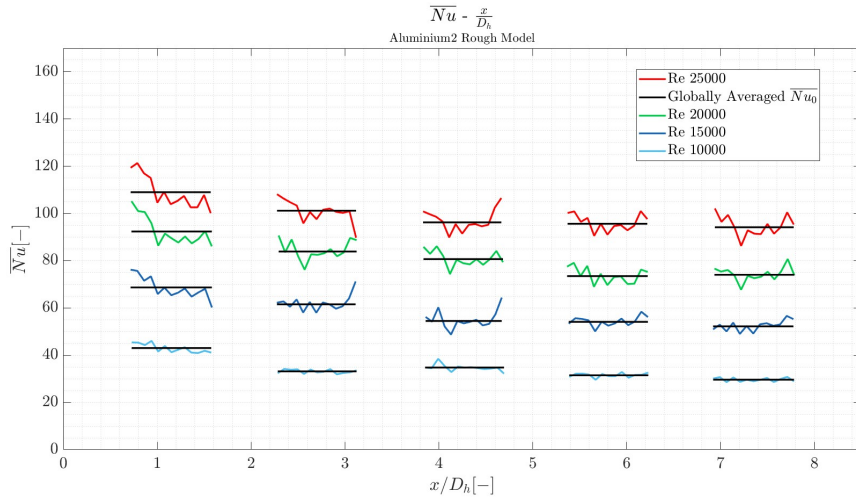


Figure 74: Laterally averaged Nusselt for all the tested flow conditions for the Aluminium2 rough surface model.

5.1.4 Comparison of the three rough surfaces

It can be interesting to compare the behavior of the three test objects provided in section 3.1.3, regarding the HTC, and therefore the Nu (Equation 46). In Table 14 the differences between the parameters quantifying the surface roughness are highlighted:

Surface	R_a [mm]	R_z [mm]	R_q [mm]	R_{sk}	R_{ku}
Smooth	0	0	0	0	0
Aluminium1	0.37	2.35	0.49	2.00	5.80
Aluminium2	0.62	2.48	0.69	0.29	3.50
Inconel939	1.10	5.74	1.30	0.94	3.157

Table 14: Surface roughness parameters for different materials in the up-scaled configuration

The surface on which this thesis focuses (Aluminium2) has a Nusselt number that generally places it in between the other two surfaces evaluated, for all the tested Reynolds except for $Re = 10000$. This intermediate result for Reynolds numbers 15000, 20000, and 25000 can be explained by Aluminium2's roughness characteristics, which are higher than those of Aluminium1 but lower than those of Inconel939, as seen in Table 14, except for R_{sk} and R_{ku} . Furthermore, (Figure 37) shows that the density of roughness components in Aluminium2 is substantially larger than that of Aluminium1. As previously mentioned, for $Re = 10000$ the behavior changes (Figure 75), resulting in the lowest average Nu out of the three. To understand why this happens a more detailed plot of the heat enhancement in the last window will be shown (Figure 76 and 77).

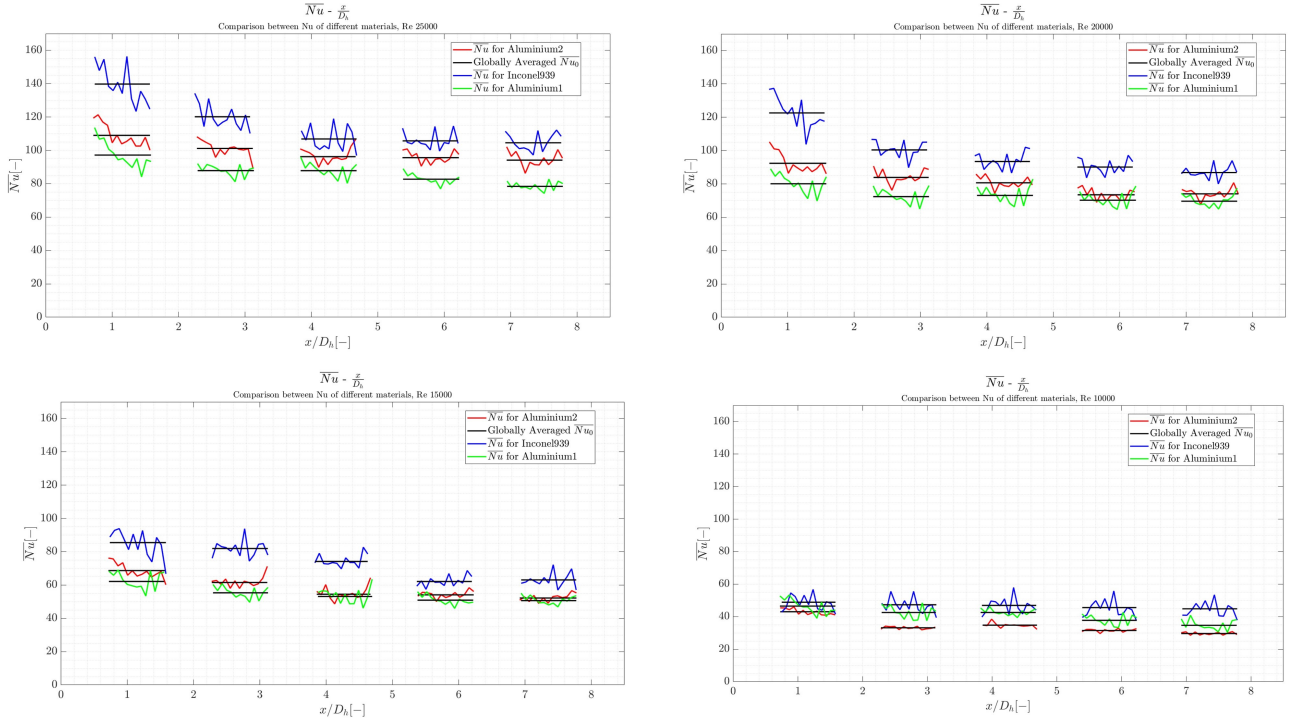


Figure 75: Three surfaces comparison for all the tested Reynolds.

According to the related graph, In939 shows the most significant enhancement in heat transfer, followed by Al2 and then Al1. The peaks coincide with the position of the roughness spheres, where heat exchange can have an increase of 4.11. A further analysis for $Re = 10000$, where there is a shift between the Al1 and Al2 behavior, is shown in Figure 77. Examining this plots, Al2 has a value closer to zero with respect to the other two, indicating behavior similar to a smooth surface. These plots allow to see how much the roughness affects the HT on a local level and the overall flow. It's clear for Al1 that in the smooth parts there is an enhancement that is most likely given by the effect of the upstream plates in the test section on the flow's velocity profile. As a result, Aluminum1's smooth regions show a heat transfer enhancement factor of 2.09, which is greater than Aluminium2's 0.43 and raises the average Nusselt number throughout the plate. The velocity profile must be investigated in order to elucidate the specific interactions near the surface roughness and the impact of the spheres on the flow, which is the major goal of the PIV rig used in this research.

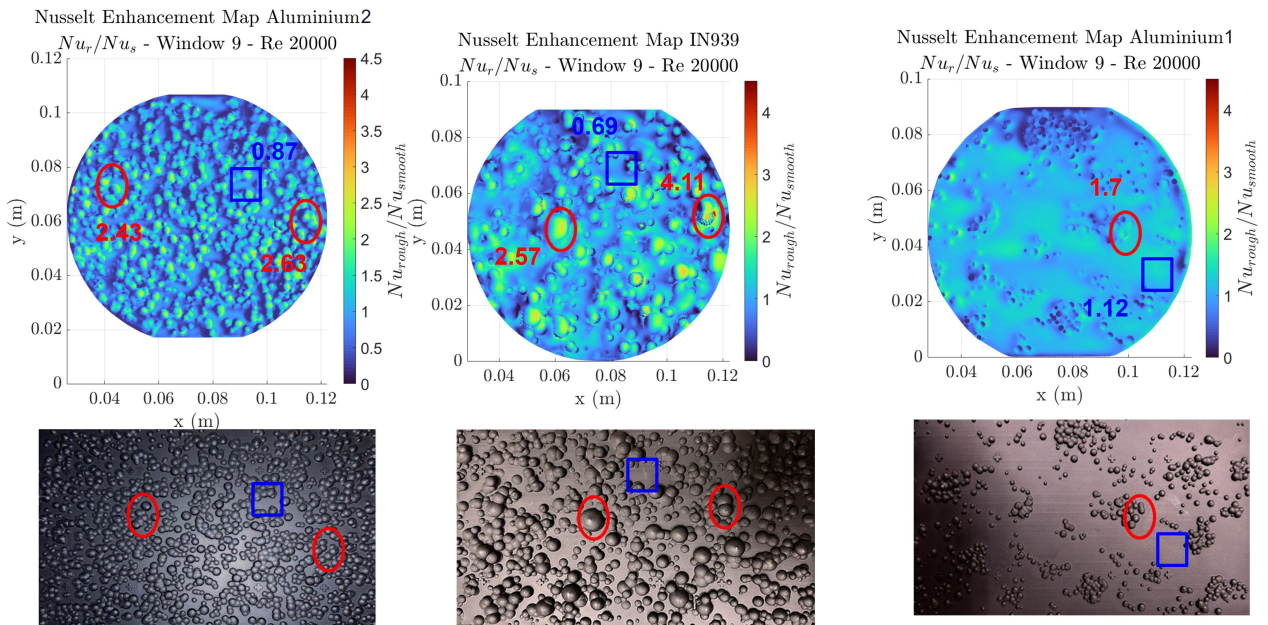


Figure 76: Nusselt enhancement in the fully developed flow comparison for Reynolds 20000.

The assumption that stands behind this behavior is that Al2's roughness, for this specific low Re, is not enough

to break the viscous sublayer (Figure 78), and that the flow may have not reached the fully turbulent region yet.

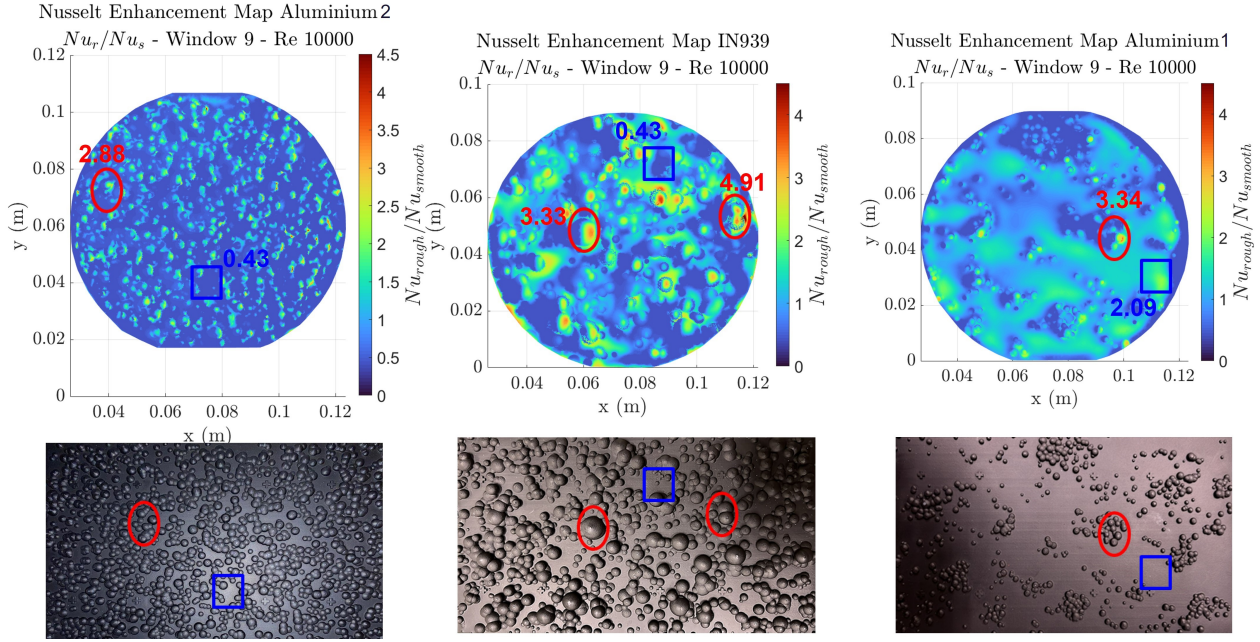


Figure 77: Nusselt enhancement in the fully developed flow comparison for Reynolds 10000.

In the Moody diagram (Figure 17) this will be somewhere in the transition region. To prove this assumption the rig should be modified and the test section enlarged in terms of channel length, the pressure losses could then be derived. Meanwhile a more simplistic explanation that refers to the study of Kadivar et al. [8] focuses on the density of the roughness elements, which can vary from D-type (high density) to K-type (low density).

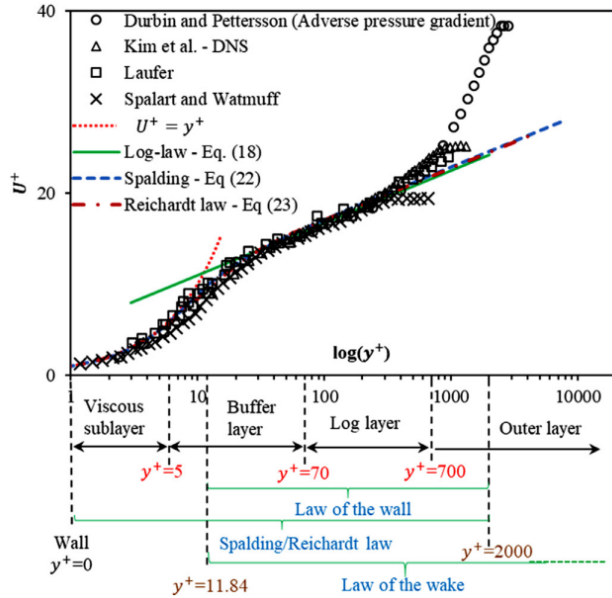


Figure 78: Variation of the dimensionless mean velocity profile of the turbulent boundary layer with the logarithmic distance from the wall.

In this case 'D-types' relates to Al2, and 'K-type' to Al1. In Aluminum2, the high-density rough components create cavities that trap the vortices caused by impact with the spheres. As a result, the flow itself and the velocity profile are untouched by the roughness, acting as if the surface were totally smooth.



Figure 79: Roughness density classification.

5.1.5 Modification of the Surface Roughness Heat Transfer rig

An additional part to add to the test section has been designed as shown in Figure 80. The main purpose of this modification would be to have a larger part where the flow is fully developed, to reach a higher accuracy for the results: the 5 mm step will weigh less on the results because the channel will be long enough to go beyond the entrance region. In order to make this possible, half of the flow straightener preceding the test section needs to be removed for spacing issues, therefore a honeycomb has been designed to be inserted into the channel, which has precisely the objective of straightening the flow. The design of the honeycomb has been obtained as explained in section 5.2.4 and the dimensions adapted for this rig, the CAD design is shown in Figure 81.

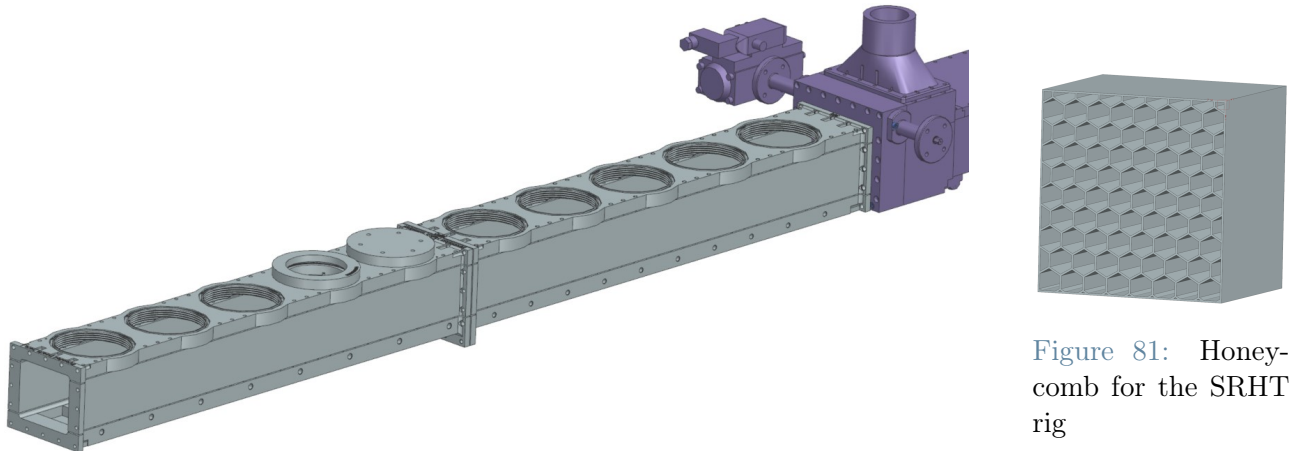


Figure 81: Honeycomb for the SRHT rig

Figure 80: NX model for the new rig

5.2. PIV rig

5.2.1 Cross-correlation coefficient

A Particle Image Velocimetry (PIV) rig's validation process is an essential step in guaranteeing the accuracy and reliability of the velocity measurements the system provides. Through a methodical evaluation of variables like measurement uncertainty, spatial resolution, and optical setup calibration, the validation process seeks to determine if the rig is able of collecting precise velocity data for fluid flow research. A crucial validation method in Particle Image Velocimetry that is essential to guaranteeing the accuracy and reliability of the velocity readings taken from the system is the cross-correlation coefficient assessment. The cross-correlation coefficient measures the degree of similarity between particle patterns in consecutive image pairings, which makes it possible to evaluate particle displacement and the accuracy of velocity measurements. A high cross-correlation coefficient confirms the integrity of the velocity field and indicates a significant correlation between the particle patterns and particle displacement estimation. This reliability metric allows researchers to address possible problems that can compromise the accuracy of the flow field data while also verifying the consistency and integrity of the velocity vectors. The value of mean correlation coefficient calculated using the formula in equation 61, depends on the resolution and the interrogation window size, so depends on the test itself. The test can be divided in boundary layer and central field of view which have different settings. The information about the test analyzed are shown in the Table 15. The results of mean cross correlation coefficient for each test sorted by day of testing in the 15, are shown in Figure 82. In the Figure is evident that the coefficient is always higher than 0,6 so we can consider the results precise enough and also analyzing the parameters in the Table 16.

Test index	Re	Δt	Interrogation window size	f-stop	Laser power
1	15054	57	16	16	70%
2	28218	30	16	16	70%
3	39211	26	19	16	70%
4	51815	27	19	16	75%
5	35220	52	16	16	75%
6	15054	37	16	16	75%
7	35220	27	16	16	75%
8	15054	27	16	16	75%
9	21846	27	16	16	75%
10	28078	27	29	16	75%
11	34520	27	19	16	75%
12	38581	67	22	16	75%
13	52515	46	24	16	75%
14	34590	36	23	16	75%
15	17575	33	24	16	75%
16	25137	28	28	16	75%
17	31509	52	16	16	75%
18	35290	28	16	16	75%
19	15194	28	24	16	75%

Table 15: Test parameters in the center position

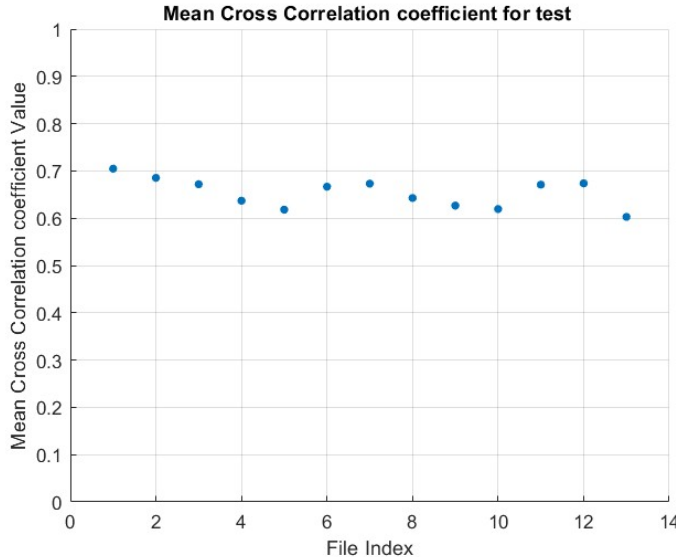


Figure 82: Cross correlation coefficient in the center position.

Statistic	Value
Mean Value	0.652
Standard Deviation	0.038
Maximum Value	0.712
Minimum Value	0.575
Difference	0.137

Table 16: Cross Correlation Coefficient Statistics

5.2.2 Turbulence intensity

Turbulence intensity is a crucial factor in determining how accurate airflow simulations are to actual circumstances during a wind tunnel validation. High levels of turbulence intensity have the potential to impact the stability and performance characteristics of models or prototypes by directly influencing the aerodynamic forces and moments they encounter in the wind tunnel. Furthermore, the impact of turbulence strength on boundary layer behavior is quite relevant. In order to ensure that the wind tunnel accurately replicates critical boundary layer phenomena, such as the laminar-to-turbulent transition and separation points, which are essential for understanding the aerodynamic performance of vehicles, aircraft, and other structures, it is imperative to check the turbulence intensity. In order to accurately simulate real-world conditions, a turbulence intensity level of 1% to 2% is often sought after for subsonic aerodynamic testing. Slightly higher turbulence intensity

levels—typically in the range of 3% to 5% may be allowed in supersonic testing.

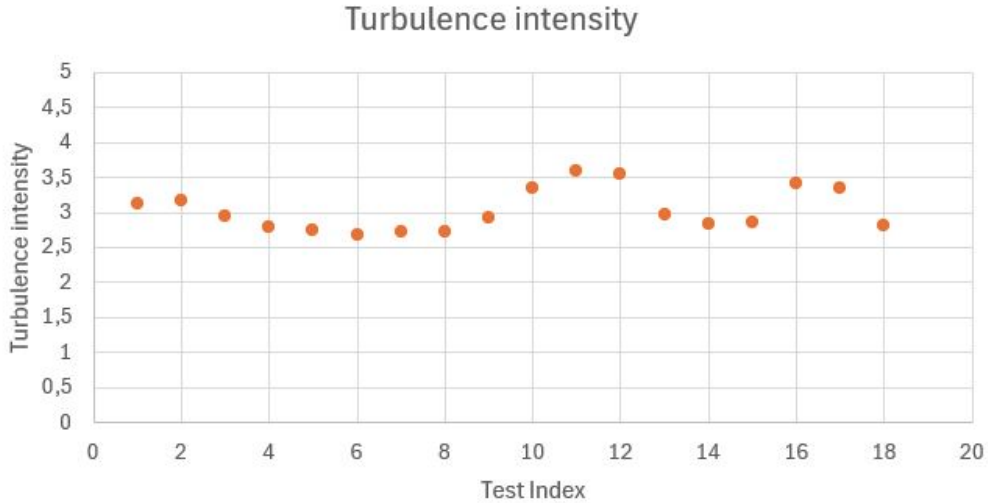


Figure 83: Turbulence intensity of measurement cases.

The turbulent intensity results of the 19 test listed in the Table 15 are shown in the Figure 83. The equations used for this calculation are:

$$I = \frac{u'}{U} \quad (78)$$

$$u' \equiv \sqrt{\frac{1}{3}(u_x^2 + u_y^2 + u_z^2)} = \sqrt{\frac{2}{3}}k \quad (79)$$

$$U \equiv \sqrt{U_x^2 + U_y^2 + U_z^2} \quad (80)$$

Turbulence intensity is calculated as the ratio of the mean square root of turbulent velocity fluctuation and the Reynolds averaged velocity of the 3 velocity components. The mean square root of turbulent velocity fluctuation is calculated from the turbulent kinetic energy k , which is derived as:

$$k = \frac{3}{4}(u_{rms}^2 + v_{rms}^2) \quad (81)$$

The results show that the values are below 4% with a maximum of 3.6% and we can state also taking into account the Table 17 that the wind tunnel correctly simulate a turbulent internal air flow without any phenomena which could affect the results.

Statistic	Value
Mean Value	3.03
Standard Deviation	0.306
Maximum Value	3.6
Minimum Value	2.67
Difference	0.927

Table 17: Turbulence Intensity Statistics

5.2.3 Velocity profile at the center-line

The validation procedure for the center position of the test section is executed comparing the experimental results with the modified power law shown in the equation 19. The velocity which is taken into account in this analysis is the time-averaged and spanwise averaged component u of the velocity profile calculated from the 2000 frames. The modified power describe the mean velocity profile along the width of the channel, where the coefficient are equal to:

$$m = 2; \quad (82)$$

$$n = 0.77 \cdot \log(Re) - 3.47; \quad (83)$$

r is the fraction of the x position and the width of the channel. The Figures 84, 85, 86 and 87 shows test 4,5,9 and 10 which describe a wide range of Reynolds number.

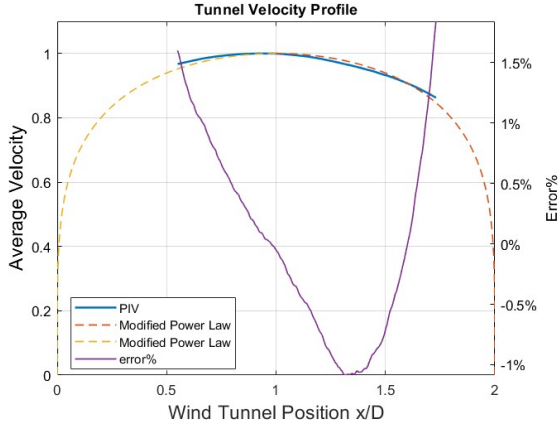


Figure 84: Velocity profile test 4 compared to the modified power law

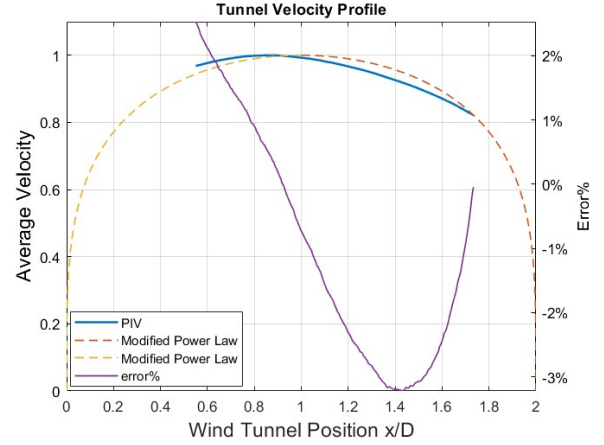


Figure 85: Velocity profile test 5 compared to the modified power law

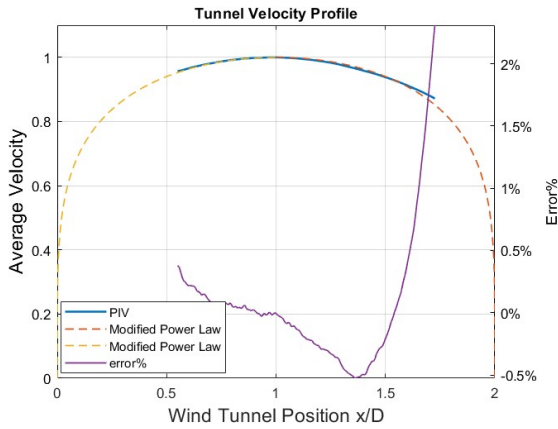


Figure 86: Velocity profile test 9 compared to the modified power law

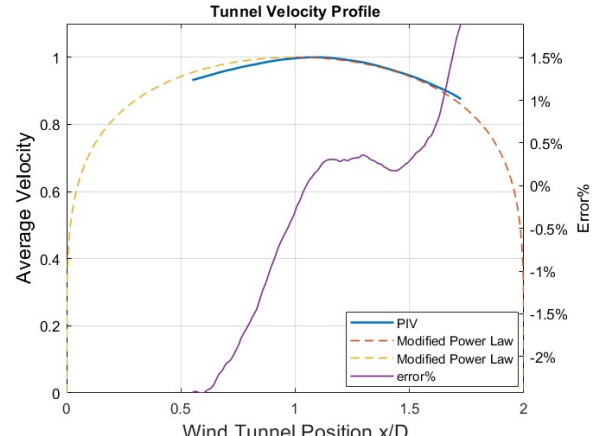


Figure 87: Velocity profile test 10 compared to the modified power law

The error of experimental velocity profile from the theoretical value is shown in the same Figures. We can observe that the error value is maximum 2% so we can consider the results reliable. The lowest error is in test 9 where it is in the range of 0.1%. The other tests do not follow perfectly the theoretical values because of a symmetry problem. The maximum velocity position does not correspond to the center-line of the channel.

	Value
SSE	0.0280
R-square	0.9422
DFE	41.0000
Adj R-sq	0.9351
RMSE	0.0262

Table 18: Quality of the polynomial function of the displacement

In Figure 88 we can observe 41 tests' velocity profiles and the displacement of the maximum velocity indicated in the graph. The displacement cannot be assumed to be a consequence of the 90 degrees elbow before the test section because it should be independent from the Reynolds number [66].

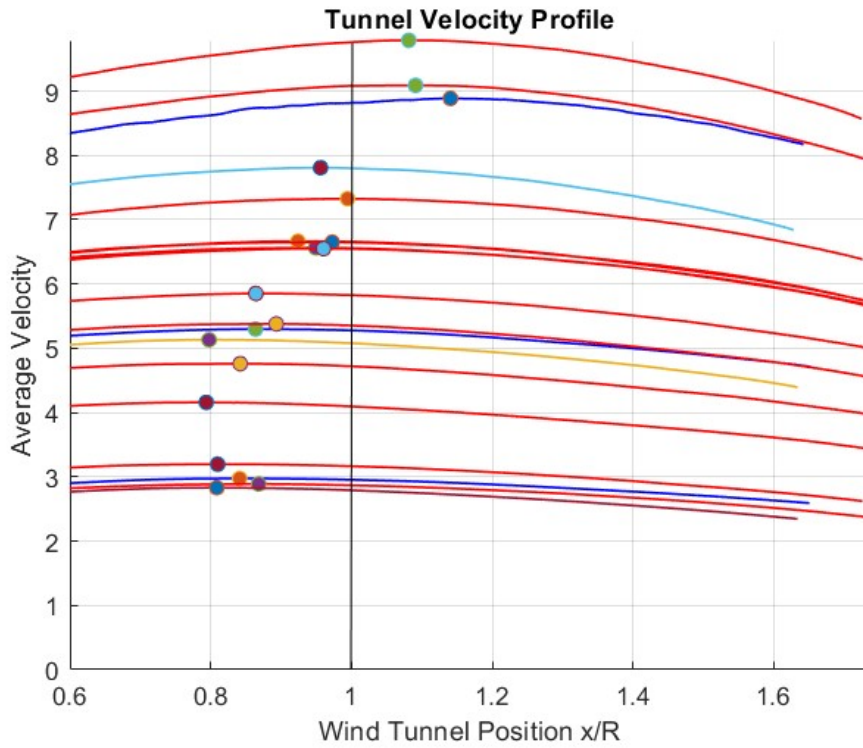


Figure 88: Maximum Velocity displacement from the center-line

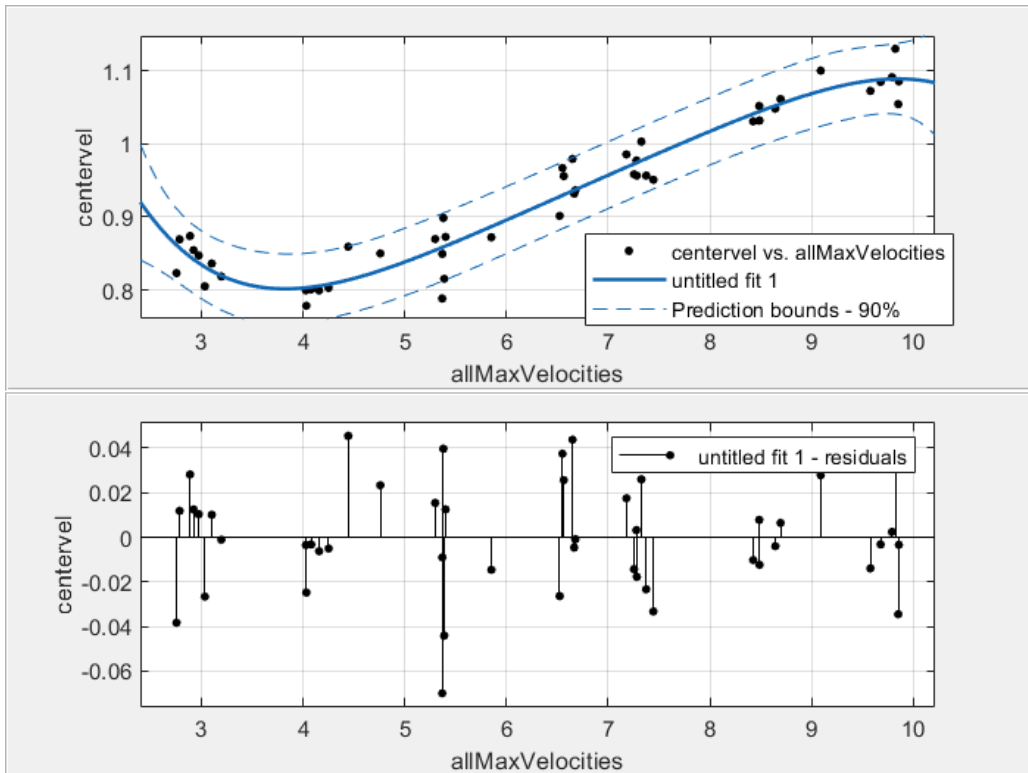


Figure 89: 4th order polynomial function of the difference of the position of the maximum velocity and the center-line velocity and residual plot

Our results presents a displacement in the left side for low Reynolds and in the right for high Reynolds. As we can see in the Figure 89 the displacement seems to follow a trend and we can predict the function of the displacement in respect to the center-line with a polynomial function of 4th order with the help of the curve fitter app of Matlab. Since it is impossible to determine the exact cause of these oscillations, the order of the

polynomial function was selected for accuracy's purpose. 41 tests were used to create the polynomial function; these tests were created by repeating all of the prior tests under the identical circumstances in order to detect any human error. The quality of the polynomial function is shown in Table 18. The polynomial function has the goal to distinguish the displacement of the velocity profile due to the rough plates and the one due to the channel structure.

5.2.4 Honeycomb solution

The flow-conditioning section of most wind tunnels includes a settling duct, screens, and a honeycomb. The honeycomb reduces up larger-scale flow instability and aligns the flow with the tunnel's axis. In order to avoid turbulence, the honeycombs should have a hexagonal cross section and a cell size ratio of 7 to 10 [67], which is equivalent to a length to hydraulic diameter ratio of 7 to 10. Pope [68] further states that the porosity, or the ratio of the covered mesh area to the overall area, should be between 0.5 and 0.8. The purpose of the honeycomb is to eliminate the components of flow velocity that are normal to the walls and to entirely guide the flow as much in the direction of the duct axis as possible. Honeycombs are often positioned just before the test chamber and, hence, before the start of the session. In our case the honeycomb will be positioned right after the elbow before the test section. The squared wind tunnel has a dimension of 97 mm and so the cross sectional area is 9409 mm². To calculate the length and the porosity needed we have to following steps. Due to the 3D printer's specifications, we chose to employ a thickness of 0.8 mm. The Figure 92 shows the main geometric characteristics. The hydraulic diameter and the external honeycomb cell length are calculated as:

$$d_{honey} = 2 \cdot \sin(60^\circ) \cdot l_{honey} \quad (84)$$

$$l_{ghoney} = l_{honey} + \frac{2 \cdot s_{honey}}{\tan(60^\circ)} \quad (85)$$

Using these 2 parameters we can calculate the solid area of the honeycomb as:

$$S_{Solid} = \Delta S = \frac{3\sqrt{3}}{2} \cdot (l_{ghoney}^2 - l_{honey}^2) \quad (86)$$

The total solid area needs the number of divisions horizontally n_h and vertically n_v which can be derived using the solid sheet division length z_{honey} , all these parameters are calculated in the equations below:

$$z_{honey} = 2 \cdot (l_{honey} + l_{ghoney}) \quad (87)$$

$$n_h = \frac{h_{sc}}{z_{honey}} \quad (88)$$

$$n_v = \frac{2 \cdot L_{SC}}{s_{honey} + d_{honey}} \quad (89)$$

Finally the total solid sheet area can be evaluated as:

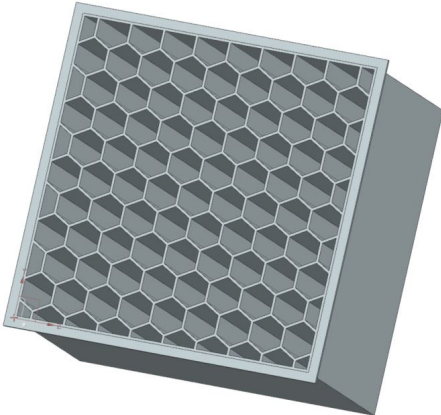
$$A_{solid} = 2 \cdot S_{hex} \cdot n_h \cdot n_v \quad (90)$$

The porosity β_h and the hydraulic diameter can be calculated:

$$\beta_h = 1 - \sigma_h = 1 - \frac{A_{solid}}{A_{tot}} \quad (91)$$

$$D_{honey} = d_{honey} \cdot \sqrt{\frac{6}{\pi \cdot \sqrt{3}}} \quad (92)$$

The honeycomb's length acts as a settling distance where heat is released from small-scale turbulence. The maximum test section velocity is decreased, though, if a honeycomb section is too long because the boundary layer in each honeycomb cell expands and the wind tunnel system faces significant pressure loss. According to Bradshaw and Mehta [69], honeycombs with shorter axial lengths are preferable. They create less turbulence and cause the system to lose less pressure. The length of the honeycomb should be calculated multiplying 7 to the hydraulic diameter. In our case the optimum values where found with a try and error method and the final results are listed in the Table 19and in the Figure 90:



Variable	Value
$d_h[\text{mm}]$	10
$D_h[\text{mm}]$	10.5
$A_{solid}[\text{mm}^2]$	1579.460
β_h	0.83213
Length [mm]	73.5

Table 19: Honeycomb characteristics.

Figure 90: Honeycomb design for PIV system.

The position of the honeycomb is a very critical because it can affect the results. Downstream of the honeycomb, the several channel profiles progressively merge into a single, consistent velocity profile. The velocity fluctuations rise in parallel with this development, rising and then gradually decline. The Reynolds number determines the location and size of the turbulence intensity peak [12]. The position of the turbulence intensity peak approaches the honeycomb as the Reynolds number rises, until the flow within the honeycomb cell becomes turbulent.

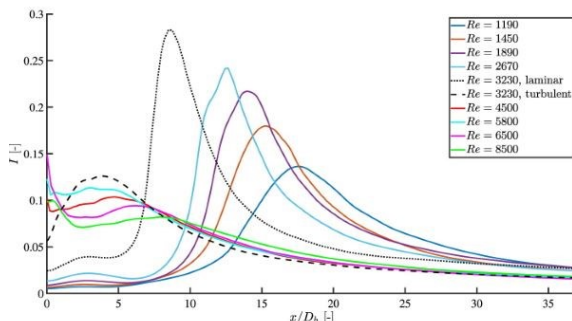


Figure 91: Turbulence intensity downstream of a honeycomb varying the Reynolds numbers [12].

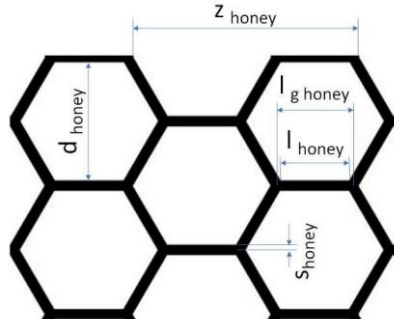


Figure 92: Honeycomb hexagonal structure geometry [13].

The turbulence intensity peak is moving away from the honeycomb as the Reynolds number increases, as seen in Figure 91. It may be presumed that the honeycomb should be at least 20 times the distance of the hydraulic diameter; in our instance, it should be placed at 200.5 to be certain. We may conclude from the graph that $15D_h$ is sufficient, or 157.5 mm, since our test reached the maximum velocity at $Re=52515$. The elbow of the wind tunnel construction is at least two meters away from the test section, hence the honeycomb is positioned far enough to avoid any effects on the results. The cell size should be smaller than the smallest lateral wavelength of the velocity change, according to Mehta and Bradshaw (1979). The velocity field inside a flow can change over time and space in fluid dynamics. The distance between consecutive peaks or troughs of the horizontal velocity fluctuation across the flow is referred to as the lateral wavelength. The shortest distance at which the velocity field shows significant lateral direction fluctuations is represented by the smallest lateral wavelength. In a dataset, the highest frequency component derived from the Fourier analysis corresponds to the smallest wavelength of variation. The smallest wavelength in the context of a velocity profile along the x-axis is the shortest distance over which the velocity variation completes one complete oscillation cycle. I have selected 4 tests from Table 15 and performed the Fast Fourier transformation to the mean velocity profile. Then I identified the index of the minimum amplitude in the first half of the amplitude spectrum (up to the Nyquist frequency) and extracted the frequency corresponding to the minimum amplitude. The smallest lateral wavelength is the inverse value of the minimum frequency. The results are shown in the Table 20.

Test Index	λ_s [m]
11	0.030
12	0.015
13	0.025
14	0.021

Table 20: Test Index and Corresponding smallest lateral wavelength values.

The characteristic dimension of the honeycomb is the hydraulic diameter which in our case is equal to 0.0105 m. Comparing the values of the 4 test in analysis it can be stated that the smallest later wavelength is higher than the honeycomb dimensions. The final check we may perform is the pressure drop created by the presence of the honeycomb which can affect the volume flow measurement of the wind tunnel. The inertia and viscous resistances are affected when airflow flows through the porous material. The viscosity and inertia loss of the flow field under various honeycomb parameters should be investigated in order to examine the rectifying impact of various honeycomb parameters. The following is an expression of its relationship:

$$\frac{\Delta P}{\Delta \delta} = -S = \frac{\mu}{\alpha} v + \frac{C_2}{2} \rho v^2 \quad (93)$$

where ΔP denotes the pressure differential between the porous material's two ends and $\Delta \delta$ denotes the material's thickness.

Porosity	Velocity (m/s)	Pressure Drop (Pa)	Fitting Equation	Viscous	Inertial
0.9118	5	11.6659	$\frac{\Delta P}{\Delta \delta} = 4.091v^2 + 25.2388v$	0.0014	6.3426
	10	32.5798			
	15	65.1635			
	20	107.287			
	25	159.259			
0.8702	5	12.5922	$\frac{\Delta P}{\Delta \delta} = 4.7474v^2 + 27.2264v$	0.0015	7.3602
	10	36.8041			
	15	74.0126			
	20	122.629			
	25	182.02			
0.8339	5	13.8446	$\frac{\Delta P}{\Delta \delta} = 5.9966v^2 + 25.437v$	0.0014	9.2971
	10	41.9094			
	15	86.5913			
	20	145.894			
	25	218.701			
0.8004	5	15.5627	$\frac{\Delta P}{\Delta \delta} = 7.0467v^2 + 27.8077v$	0.0015	10.9252
	10	48.1755			
	15	100.464			
	20	169.51			
	25	254.356			
0.7666	5	17.4075	$\frac{\Delta P}{\Delta \delta} = 8.4313v^2 + 31.1299v$	0.0017	13.0717
	10	56.163			
	15	118.335			
	20	200.297			
	25	301.177			

Figure 93: Pressure loss coefficient for different honeycomb designs [14].

S stands for momentum, μ for viscosity, v for velocity, ρ for air density, $\frac{1}{\alpha}$ for viscous resistance coefficient, and C_2 for inertial resistance coefficient. Hexagonal honeycombs incur the lowest pressure losses and are the most efficient for wind tunnel turbulence reduction [70]. Tian et al [14] design a low-speed wind tunnel and obtained the pressure drop and flow field velocity on both side of the honeycomb structure. The design is comparable with our system and the values of the resistance coefficient in Figure 93 can be employed. Analyzing the 4 tests (test 11 to 14) the velocity range in our wind tunnel are from 2.5 to 8.22. Hence, I chose to employ the fitting curve of the results for the design with 0.833 porosity which is very close to the value of our design. The expected pressure drops are shown in Table 21.

Test Index	v [m/s]	α	C_2	$\frac{\Delta P}{\Delta \delta}$ [Pa/m]	ΔP [Pa]
11	5.49	0.0014	9.297	16.876	1.240
12	2.79	0.0014	9.297	4.357	0.320
13	3.99	0.0014	9.297	8.910	0.655
14	5.00	0.0014	9.297	13.999	1.029

Table 21: Expected pressure drops due to the honeycomb structure.

The values of the pressure drop gradient are been multiplied to the length of the honeycomb in analysis and we can state that the pressure drop caused by the presence of the honeycomb is negligible. Following the honeycomb installations, 13 tests were conducted; the results are shown in Table 22.

Test Index	Re	Δt	Interrogation window size	f-stop	Laser Power
1	14914	52	16	16	75%
2	27448	28	16	16	75%
3	34520	26	19	16	75%
4	45163	26	24	16	75%
5	52725	27	29	16	75%
6	14914	52	16	16	75%
7	27448	28	16	16	75%
8	34520	26	19	16	75%
9	45163	26	24	16	75%
10	52725	27	29	16	75%
11	10503	76	16	16	75%
12	19326	33	16	16	75%
13	24997	27	16	16	75%

Table 22: Experimental Data after the honeycomb installation.

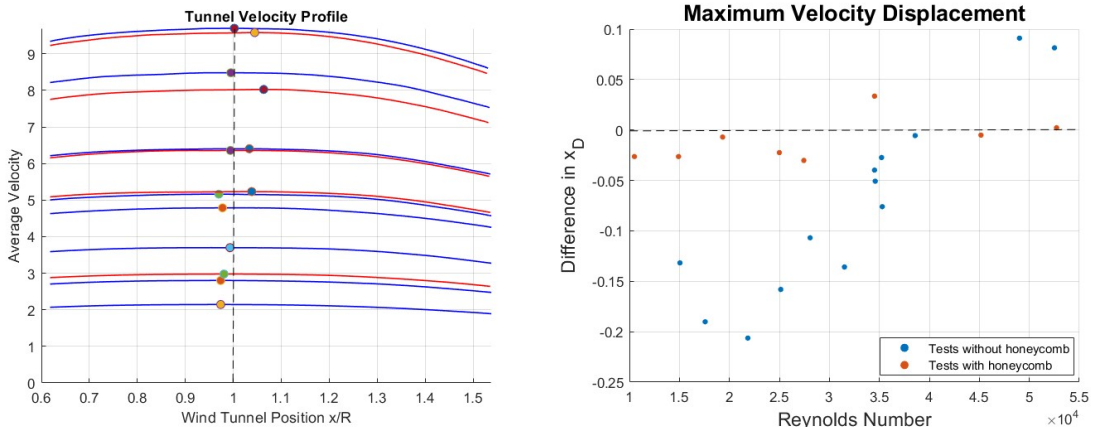


Figure 94: Average velocity profile after the honeycomb installation.
Figure 95: Position displacement of the maximum velocity profile comparison.

Figure 94 displays the velocity profile results following the installation of the honeycomb. The maximum velocity is located quite near the channel center and is obviously more uniform than it was previously. We can state that the honeycomb structure had a positive impact to the maximum velocity displacement, which before reached almost 10% of the characteristic length. The results considered for the comparison are the tests from 4 to 16 of the Table 15.

5.2.5 Reynolds stresses

Another validation of the data can be done comparing the Reynolds stressed with DNS data found in the article "Direct numerical simulation of turbulent channel flow up to $Re_\tau = 590$ [71]. The DNS data at $Re_\tau = 180$ were compared with the test which had a value of $Re_\tau = 168$ in Figure 96:

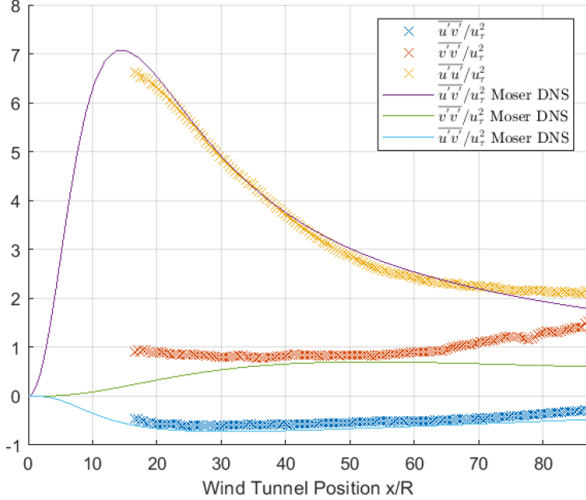


Figure 96: Reynolds stresses comparison with DNS data at $Re_\tau = 180$

The results $u'u'$ and $u'v'$ followed the DNS data but the behaviour of $v'v'$ could be explained by the symmetry problems or calibration errors. The DNS data at $Re_\tau = 587$ were compared with the test which had a value of $Re_\tau = 864$ in Figure 97. The values followed more the trend even if the Re_τ is different and this can be caused by the displacement of velocity profile.

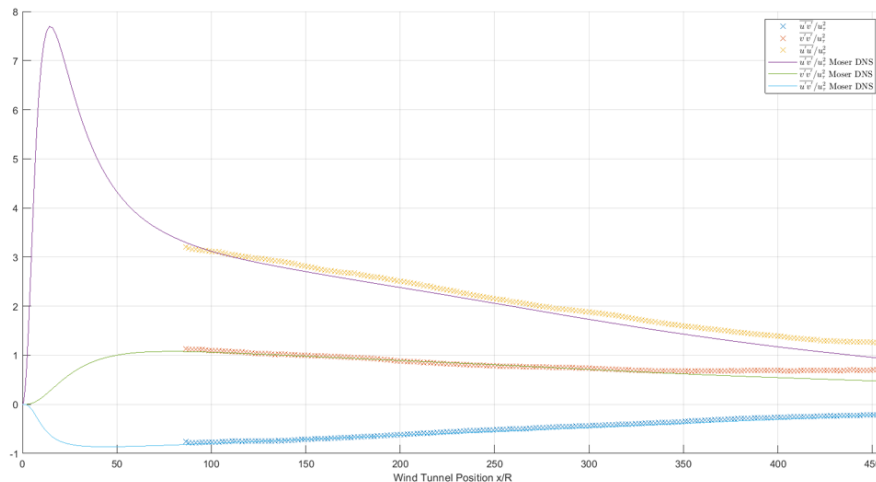


Figure 97: Reynolds stresses comparison with DNS data at $Re_\tau = 587$

The whole trend of the Reynolds stresses can be considered reliable due to the general behaviour of the experimental results.

5.2.6 Boundary layer velocity profile

The boundary layer results have been compared to the theoretical law called log law shown in equation 26 which describe the velocity profile in the log layer. The calculation of friction velocity employed the Clauser chart method. The simplest way to calculate the friction velocity is using the friction factor and the the velocity given by the mass flow measurement of the wind tunnel or the center-line value of the velocity profile:

$$u_* = \langle u \rangle \sqrt{\frac{f_D}{8}} \quad (94)$$

However this method has its limits and the Clauser chart method is a better method to get a better fit of the log law near the walls. The method used is described in the experimental work of F.H. Clauser [72]. By using direct measurements of the free stream velocity U_∞ and the mean velocity profile $U(y)$, where y is the normal distance from the wall, the friction velocity is extrapolated with the Clauser chart method. The methodology relies on the assumption that the velocity profile in the boundary layer overlap region follows an universal logarithmic law. Assuming that the coefficient of friction C_f is defined as $C_f = 2(\frac{u_\tau}{U_{infty}})^2$, the Clauser chart equation can be written in the following form:

$$\frac{U(y)}{U_\infty} = \left[\frac{1}{\kappa} \sqrt{\frac{C_f}{2}} \right] \ln \left(\frac{y U_\infty}{\nu} \right) + \left[\frac{1}{\kappa} \sqrt{\frac{C_f}{2}} \ln \left(\sqrt{\frac{C_f}{2}} \right) + B \sqrt{\frac{C_f}{2}} \right] \quad (95)$$

The experimental data may be roughly represented by this approach in the range $y^+ > 50$. The literature frequently contains variations of the von Kármán constant κ and additive constant B, such as κ variations of $0.38 < \kappa < 0.45$ and B variations of $4.5 < B < 6.1$ [73]. For our case the value chosen for these 2 constants were $\kappa = 0.38$ and $B = 5$, which fitted the most the plane-channel in analysis. We will analyse 2 cases, one before the honeycomb modification and one after. The parameters of these 2 tests are shown in the Table 23.

Test index	Re	Δt	Interrogation window	f-stop	Laser power
1	28988	44	16	16	50%
2	14144	34	16	16	50%

Table 23: Experimental parameters of boundary layer tests.

The results of u_τ using the moody diagram and the Clauser method are listed in the Table 24.

Test index	u_τ moody	u_τ clauser
1	0.2717	0.2939
2	0.1540	0.1470

Table 24: Comparison of Shear Velocities calculated with moody diagram and Clauser-Chart method.

We can visually compare the theoretical and experimental results in Figure 98 and 100 and we can state from the error curve that the rig can be considered validated also for the boundary layer behaviour and the honeycomb did't affect the region near the wall. The error is shown in the Figure 99 and 101.

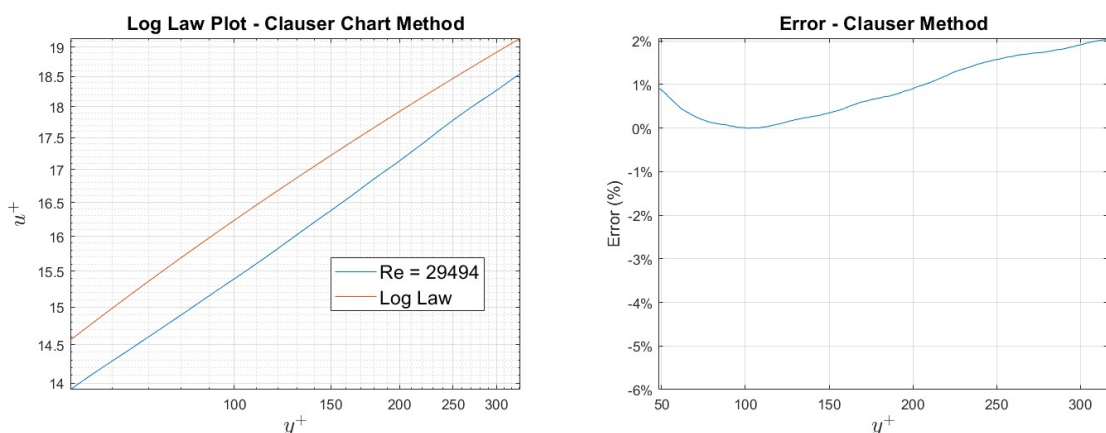


Figure 98: Log law comparison between theoretical and experimental curve for test 1.

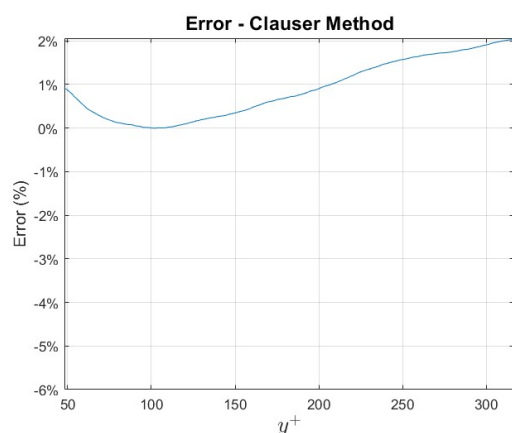


Figure 99: Error curve for Clauser Chart method log law results for test 1.

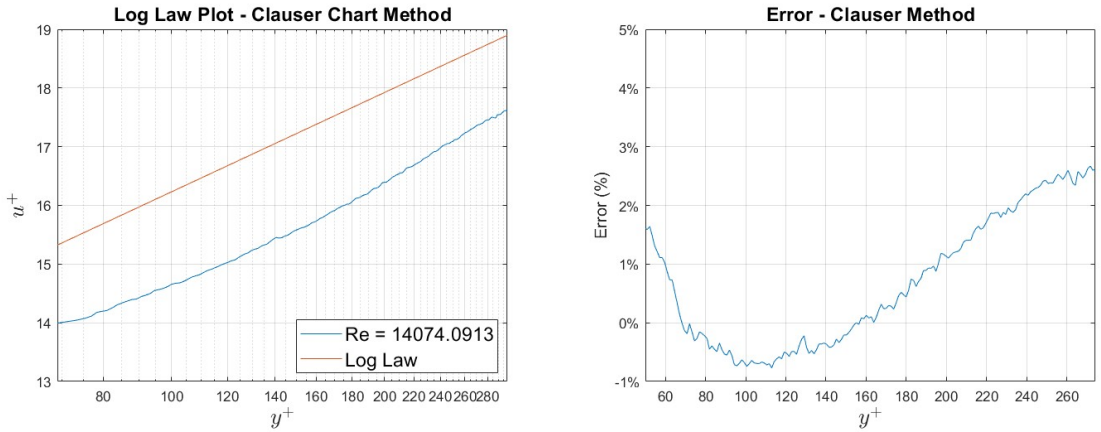


Figure 100: Log law comparison between the theoretical and experimental curve for test 2.

Figure 101: Error curve for Clauser Chart method log law results for test 2.

We cannot consider the data below $y^+ = 50$ to be legitimate since the test system can reach the log layer but not the region below because of reflections and the glue in the corner.

5.2.7 Rough plates Particle Image Velocimetry tests

After the rough plates were positioned, experiments were carried out to examine the velocity profile in the channel's center while the laser sheet was positioned at various distances from the rough plates.

Test Index	Re	Δt	Interrogation window size	f-stop	Laser Power	Distance from the plates [mm]
1	30	33	16	16	55%	43
2	31	33	16	16	55%	23
3	30	60	16	19	50%	15.5
4	30.6	60	16	19	40%	8
5	29	60	16	19	40%	7

Table 25: Experimental Data with rough plates with distance from plates.

The velocity profile of the tests listed in Table 25 are shown in the Figure 103. We can observe how the presence of the spheres are influencing the profile comparing the results with the photo of the camera's field of view of the rough plates in Figure 102.

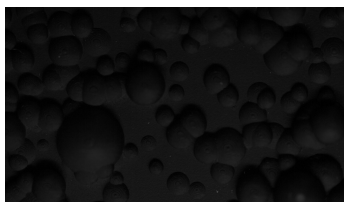


Figure 102: Camera field of view of the rough plates tests IN939.

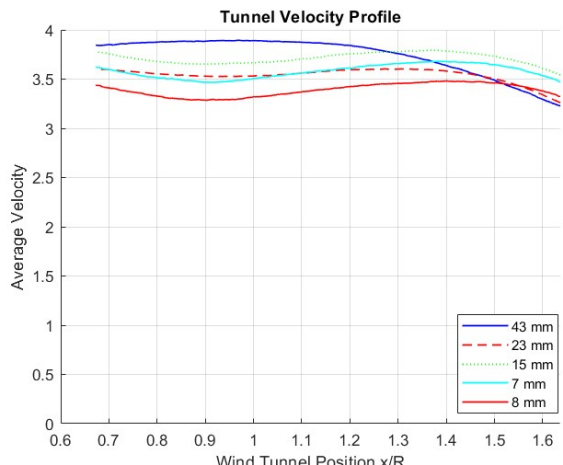


Figure 103: Velocity profiles in different distances from the rough plates.

To see the influence of the spheres we can analyze the mean velocity profile distribution of test 5 in Figure 104 which is the closest to the spheres.

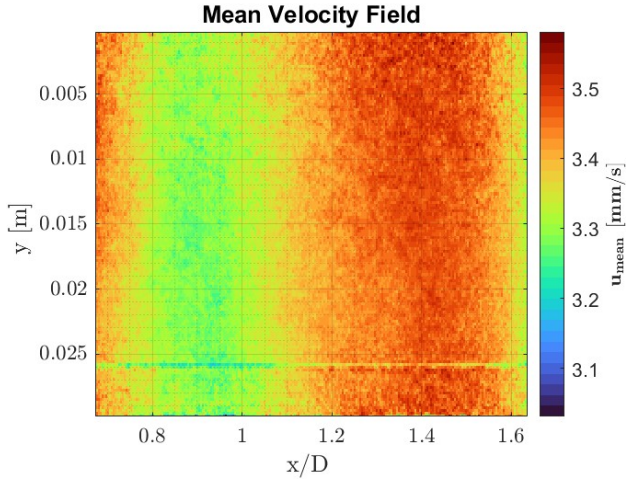


Figure 104: Mean velocity profile of test 5 on rough plates.

The big sphere on the left has a more noticeable impact, causing a decrease in the velocity profile. This could occur because of recirculation after the spheres. By comparing the roughness Reynolds number values, we can determine the roughness region. We must compute the k_s parameter in order to accomplish that. We attempted to compute it with two different methods. We assume k_s to be equal to the R_z parameter in the first method. We utilized the Colebrook-White correlation to get the friction factor, taking into account that ϵ equals R_z . The second approach makes advantage of the revised correlation that Boyle and Stripf [74] suggested, in which C_{sk} is a constant that is marginally more than one:

$$k_s = 4.3R_q (1 + C_{sk}S_k) \quad (96)$$

The correlation is valid for irregular random roughness with $R_{sk} > 0$. The final results are shown in the Table 26:

Method	k_s	k_s^+
1	0.0055	68.55
2	0.0083	104.23

Table 26: sand-grain equivalent roughness constant and roughness reynolds number results.

The values are comparable to the packed spheres bed roughness Reynolds number limits proposed by Moffat and Ligrani [75] which calculated $k_{\text{Rough}}^+ = 50$. The results in Table 26 are above this limit so we can state than our data is in the fully rough regime. This indicates that, as Figure 103 shows, the logarithmic profile shifts downward. The significant turbulence mixing caused by roughness components completely destroys the viscous sublayer in this flow regime. The IN939 can be classified as D-type rough surface because of the high density of the rough elements. For closely spaced d-type roughness, Coleman et al. [57] found that the entire cavity between ribs is occupied by stable separated eddies, with only slight disruption of the outer flow. However, the big spheres have a slightly high influence in the velocity profile. In literature we have the example of the results conducted by Djennidi et al. [76] and Leonardi et al. [77] where for d-type roughness vortex shedding into the flow has been documented but less severe than for k-type roughness. As seen in Figure 79, Jiménez [78] described the behavior of d-type roughness as having the capacity to maintain stable recirculation vortexes that separate the external flow from the roughness. D-type roughness is particularly important for heat transfer applications and can lower drag by trapping fluid pockets between roughness components. The vortex shedding effects can be found in the Nu distribution of the window 9 at $\text{Re}=20000$ results of the rig shown in Figure 105 because we can see the decreasing of the heat enhancement after the big sphere in analysis. The effect of the big sphere is also present in the velocity profile shown in Figure 104 where we can see how the velocity profile is similar to a vortex shedding behind a cylinder. The flow cannot be consider 2D because of the sphere is in contact with the surface and for this reason have 3D phenomena that cannot be ignored. Since these are all presumptions based on five preliminary experiments, we are unable to definitively identify the cause of this impact in the velocity profile, more testing would be required.

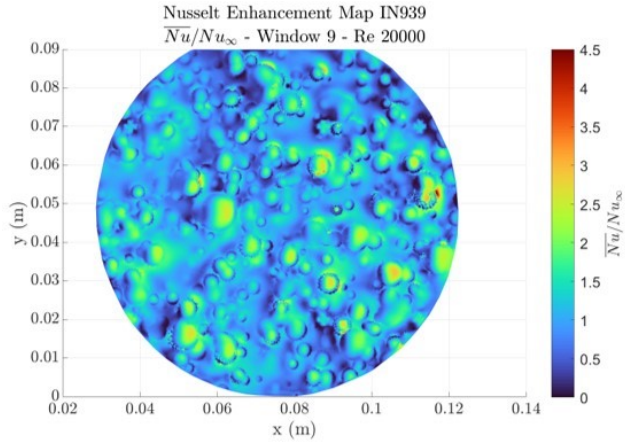


Figure 105: Nu enhancement IN939 Re=20000 window 9.

5.2.8 Modification of the test section

The wind tunnel's test section has a lot of limitations. First of all, the glue on the Plexiglas joints makes it challenging to approach the boundary layer. The glue creates a layer of particles that the OpenPIV lab is unable to detect since it is very reflecting and opaque, which cause very low cross-correlation coefficients. The outer layers are also affected by the glue, which results in several reflections. This issue has been resolved by designing a new test section in which the Plexiglas is adhered to the bed plates inside, preventing the glue from getting in the way of the laser sheet. Another modification has been made to make it easier to remove and replace the plates; this can now be done by simply inserting the hand inside rather than dismounting every component. The Plexiglas is not separated from the bed plates since the single pieces are now two instead of three, which makes plate replacement easier.



Figure 106: New test section design.

6. Conclusions and Future Works

The results of this thesis show that in cooling channels made via additive manufacturing, surface roughness has a major impact on fluid flow behavior and heat transfer. The experimental study shown that the rough surface topologies produced by L-PBF methods and the turbulent flow structures interacted in a complex way. The data for 3 different materials were collected, providing a solid starting point to evaluate the effects given by different parameters describing the surface roughness. From the results it was possible to see that the impact on the local Nusselt enhancement changed also based on the different parameters optimized. As seen from the results from the IR rig tests, aluminum 2 plates behave differently from the other 2 test objects. We may mention the R_{sk} and R_{ku} weights more than the other parameters regarding heat transfer. We attempted, by making assumptions based on a few available papers about turbulent flow over rough surfaces, to identify the reasons for the unexpected behavior at low Reynolds numbers of the local Nusselt number that the experimental investigation revealed. It is crucial to emphasize that the assumption is predicated on a particular flow behavior that is also influenced by the Reynolds number and the unique features of the rig in use; as such, it requires more research. If for the fully developed flow section a quantitative comparison was made with correlations in the literature (such as Gnielinski and Dittus Boelter), for the entrance region and the subsequent development

section recent experimental research might offer tailored correlations or modifications for specific cases, given that the transition region is highly sensitive to factors like roughness, geometry, and flow conditions. Therefore, it is more difficult to conduct a quantitative analogy, nevertheless the trend obtained for this specific section of the channel replicates the expected decreasing trend shown by in-literature correlations. We can supplement our findings with additional data using the PIV rig experiments. A working PIV rig was designed and constructed. The center-line velocity profile was used to validate the system comparing it with the Modified Power Law. It was clear that the maximum velocity was not positioned in the center of the channel, therefore the system was optimized by designing and testing a honeycomb structure. Afterwards, the boundary layer analysis was completed, and the data was used to extract the friction velocity using the Clauser Chart approach, resulting in an u^+ profile that closely matched the theory. The experiments were only able to get the log layer, despite efforts to approach the wall. We were able to test the Inconel939 plates after the validation. The roughness created a decrease in the streamwise velocity in correspondence with the big spheres in the testing plates. We attempted to explain some of the impacts by comparing the velocity profile from the PIV rig to the data from the infrared camera. The results demonstrated the influence of the roughness on the velocity profile which will be further investigated in the future.

Regarding possible future works the two experimental techniques may require several improvements. For both the PIV and SRHT rigs, a new test section structure was designed. For the SRHT rig, the modification in the design has been presented, the new rig would allow Future students to carry out this research, giving them access to a larger dataset on fully developed flow. This improvement will strengthen the understanding attained so far, improve the results, upgrade the quality of the data, it will increase the reliability of the conclusions and will provide further material for the validation of the rig itself. This change is needed to increase our understanding of this subject. To get additional data and repeatability, the tests on the three available test objects must be repeated. The test objects can also be modified. It can be developed another upscaled AM rough plate for a different material that is used in cooling channels. Since in addition to learning how and why increased surface roughness can improve heat transfer efficiency, the goal is also to identify the roughness parameters that have the greatest impact on HT enhancement a design of a fictitious material can be created by changing these parameters taking into consideration how they differently affect HT. The PIV rig needs more structural modifications. It could be feasible to apply fluorescent paint on the plates, which would change the laser's green light into orange light. The reflections might then be filtered by a filter in the camera lens. The glue should not be present in the boundary layer measurements in the new test section design, which might greatly reduce the reflections issue as well. A Venturi system can be used to determine the bulk velocity instead of relying on the volume measurement that has been placed in the wind tunnel. To eliminate the laser waist and provide a more uniform laser light sheet, a third lens can be inserted after the spherical one. To have a faster synchronizer, employ smaller interrogation windows in the boundary layer measurements, and maximize the results in that region, the Arduino board must be replaced. The center-line tests may show fewer reflections if a suitable laser dump is designed and installed on the wall. Lastly, the second frame's blurry appearance might be avoided by lowering the noise levels.

7. Bibliography and citations

References

- [1] W. F. Cope, "The friction and heat transmission coefficients of rough pipes," *Proc. - Inst. Mech. Eng.*, vol. 145, pp. 99–105, June 1941.
- [2] D. F. Dipprey and R. H. Sabersky, "Heat and momentum transfer in smooth and rough tubes at various prandtl numbers," *Int. J. Heat Mass Transf.*, vol. 6, pp. 329–353, May 1963.
- [3] S. Energy, "Sgt-800 industrial gas turbine." <https://www.siemens-energy.com/global/en/offerings/power-generation/gas-turbines/sgt-800.html>, 2023. [Online].
- [4] S. M. e. a. Pratt & Whitney, East Hartford, "Determination of surface heat transfer and film cooling effectiveness in unsteady wake flow conditions," *AGARD Conference Proceedings*, vol. 527, 1992.
- [5] R. Clifford, "Rotating heat transfer investigations on a multipass cooling geometry," *Lakshminarayana, B.: Fluid Dynamics and Heat Transfer of Turbomachinery. Chapter 7*, vol. pp. 597–721., 1985.
- [6] H. Gladden and R. Simoneau, *Review and assessment of the database and numerical modeling for turbine heat transfer, in Toward Improved Durability in Advanced Aircraft Engine Hot Sections.* ASME Turbo Expo, 1988.

- [7] L. Jiao, Z. Y. Chua, S. K. Moon, J. Song, G. Bi, and H. Zheng, “Femtosecond laser produced hydrophobic hierarchical structures on additive manufacturing parts,” *Nanomaterials (Basel)*, vol. 8, p. 601, Aug. 2018.
- [8] D. T. Mohammadreza Kadivar and G. McGranaghan, “A review on turbulent flow over rough surfaces: Fundamentals and theories,” *International Journal of Thermofluids*, vol. Vol.10, p. 100077, 2021.
- [9] T. L. Bergman, A. S. Lavine, F. P. Incropera, and D. P. D. Witt, *Fundamentals of Heat and Mass Transfer*. John Wiley and Sons, Inc., 2011.
- [10] A. L. Hadar Ben-Gida, Roi Gurka, “Openpiv-matlab — an open-source software for particle image velocimetry; test case: Birds’ aerodynamics,” *SoftwareX*, vol. 12, p. 100585, 2020.
- [11] Z. Xue, J. J. Charonko, and P. P. Vlachos, “Signal-to-noise ratio, error and uncertainty of piv measurement,” 2013.
- [12] L. C. Thijs, R. A. Dellaert, S. Tajfirooz, J. C. H. Zeegers, and J. G. M. Kuerten, “Honeycomb-generated reynolds-number-dependent wake turbulence,” *J. Turbul.*, vol. 22, pp. 535–561, Sept. 2021.
- [13] S. Mauro, “Small-scale open-circuit wind tunnel : Design criteria , construction and calibration,” 2017.
- [14] H. Tian, T. Hao, C. Liu, H. Cao, and X. Shan, “Investigation of a portable wind tunnel for energy harvesting,” *Aerospace*, vol. 8, p. 386, Dec. 2021.
- [15] L. F. Moody, “Friction factors for pipe flow,” *Journal of Fluids Engineering*, vol. 66, pp. 671–678, Nov. 1944.
- [16] H. Darcy, *Recherches Hydrauliques Enterprises, Volumes 1-2*. Legare Street Press, Oct. 2022.
- [17] C. F. Colebrook and C. M. White, “Experiments with fluid friction in roughened pipes,” *Proceedings of the Royal Society of London. Series A, Mathematical and Physical Sciences*, vol. 161, no. 906, pp. 367–381, 1937.
- [18] W. Nusselt, “Die oberflachenkondensation des wasserdampfes,”
- [19] S. W. Churchill and M. Bernstein, “A correlating equation for forced convection from gases and liquids to a circular cylinder in crossflow,” *J. Heat Transfer*, vol. 99, pp. 300–306, May 1977.
- [20] B. S. Petukhov, “Heat transfer and friction in turbulent pipe flow with variable physical properties,” in *Advances in Heat Transfer*, Advances in heat transfer, pp. 503–564, Elsevier, 1970.
- [21] V. Gnielinski, “New equations for heat and mass transfer in turbulent pipe and channel flow,” 1976.
- [22] J. Nikuradse, “Strömungswiderstand in rauhen rohren,” *Z. Angew. Math. Mech.*, vol. 11, pp. 409–411, Jan. 1931.
- [23] M. D. Donne and L. Meyer, “Turbulent convective heat transfer from rough surfaces with two-dimensional rectangular ribs,” *International Journal of Heat and Mass Transfer*, vol. 20, pp. 583–620, 1977.
- [24] H. R. et al., “Heat transfer study of enhanced additively manufactured minichannel heat exchangers,” *International Journal of Heat and Mass Transfer*, vol. 161, p. 120271, 2020.
- [25] T. A. S. John-Mark Clemenson and S. T. McClain, “A novel method for constructing analog roughness patterns to replicate ice accretion characteristics,” *2018 Atmospheric and Space Environments Conference*, p. 3015, 2018.
- [26] E. G. et al., “Roughness parameters,” *Journal of materials processing Technology*, vol. Vol.123.1, pp. 133–145, 2002.
- [27] K. A. Flack and M. P. Schultz, “Review of hydraulic roughness scales in the fully rough regime,” *Journal of materials processing Technology*, 2010.
- [28] D. R. H. et al., “Flow in a scaled turbine coolant channel with roughness due to additive manufacturing,” *Turbo Expo: Power for Land, Sea, and Air. American Society of Mechanical Engineers*, vol. Vol. 58653, p. V05BT21A004, 2019.
- [29] R. J. Adrian, “Multi-point optical measurements of simultaneous vectors in unsteady flow—a review,” *Int. J. Heat Fluid Flow*, vol. 7, pp. 127–145, June 1986.

- [30] J. Kompenhans, M. Raffel, C. Willert, M. Wiegel, C. Kähler, A. Schröder, B. Bretthauer, H. Vollmers, and B. Stasicki, “Investigation of unsteady flow fields in wind tunnels by means of particle image velocimetry,” in *Three-Dimensional Velocity and Vorticity Measuring and Image Analysis Techniques*, ERCOFTAC series, pp. 113–127, Dordrecht: Springer Netherlands, 1996.
- [31] J. Westerweel, “Digital particle image velocimetry - theory and application,” 01 1993.
- [32] J. Kompenhans and J. Reichmuth, “Particle imaging velocimetry in a low turbulent windtunnel and other flow facilities,” 1986.
- [33] M. Machacek, “A quantitative visualization tool for large wind tunnel experiments,” 2002.
- [34] R. Höcker and J. Kompenhans, “Application of particle image velocimetry to transonic flows,” 1991.
- [35] K. Hinsch, W. Arnold, and W. Platen, “Flow field analysis by large-area interrogation in particle image velocimetry,” *Opt. Lasers Eng.*, vol. 9, pp. 229–243, Jan. 1988.
- [36] W. W. Hunter and C. E. Nichols, “Wind tunnel seeding systems for laser velocimeters,” 1985.
- [37] N. J. Lawson and J. Wu, “Three-dimensional particle image velocimetry: experimental error analysis of a digital angular stereoscopic system,” *Meas. Sci. Technol.*, vol. 8, pp. 1455–1464, Dec. 1997.
- [38] C. Willert, B. Stasicki, M. Raffel, and J. Kompenhans, “Digital video camera for application of particle image velocimetry in high-speed flows,” in *Optical Techniques in Fluid, Thermal, and Combustion Flow* (S. S. Cha and J. D. Trolinger, eds.), Sept. 1995.
- [39] M. Raffel, C. E. Willert, F. Scarano, C. J. Kähler, S. T. Wereley, and J. Kompenhans, “Image evaluation methods for PIV,” in *Particle Image Velocimetry*, pp. 145–202, Cham: Springer International Publishing, 2018.
- [40] H. Ben-Gida, R. Gurka, and A. Liberzon, “OpenPIV-MATLAB — an open-source software for particle image velocimetry; test case: Birds’ aerodynamics,” *SoftwareX*, vol. 12, p. 100585, July 2020.
- [41] H. T. Huang, H. E. Fiedler, and J. J. Wang, “Limitation and improvement of PIV,” *Exp. Fluids*, vol. 15, pp. 168–174, Aug. 1993.
- [42] T. Astarita and G. Cardone, “Analysis of interpolation schemes for image deformation methods in PIV,” *Exp. Fluids*, vol. 38, pp. 233–243, Feb. 2005.
- [43] S. Y. Son, K. D. Kihm, and J.-C. Han, “PIV flow measurements for heat transfer characterization in two-pass square channels with smooth and 90° ribbed walls,” *Int. J. Heat Mass Transf.*, vol. 45, pp. 4809–4822, Nov. 2002.
- [44] P. Singh, W. Li, S. V. Ekkad, and J. Ren, “Experimental and numerical investigation of heat transfer inside two-pass rib roughened duct (AR = 1:2) under rotating and stationary conditions,” *Int. J. Heat Mass Transf.*, vol. 113, pp. 384–398, Oct. 2017.
- [45] T. Tsuji, T. Miyauchi, S. Oh, and T. Tanaka, “Simultaneous measurement of particle motion and temperature in twodimensional fluidized bed with heat transfer,” *Kona Powder and Particle Journal*, vol. 28, pp. 2–2, 2010.
- [46] S.-H. Lee, J. H. Kim, and H. J. Sung, “PIV measurements of turbulent boundary layer over a rod-roughened wall,” *Int. J. Heat Fluid Flow*, vol. 29, pp. 1679–1687, Dec. 2008.
- [47] S. D. Je-Chin Han and S. Ekkad, *Gas turbine heat transfer and cooling technology*. CRC Press, 2013.
- [48] J. Baptiste and J. Fourier, “The analytical theory of heat,” *The University Press*, 1878.
- [49] H. Schlichting, “Experimentelle untersuchungen zum rauhigkeitsproblem,” *Ing. Arch*, vol. 7, pp. 1–34, Feb. 1936.
- [50] M. P. Schultz and K. A. Flack, “Outer layer similarity in fully rough turbulent boundary layers,” *Exp. Fluids*, vol. 38, pp. 328–340, Mar. 2005.
- [51] K. Wen, “Investigation of roughness effects on heat transfer of upscaled additively manufactured channels in the turbulent region using infrared thermography,” Master’s thesis, KTH Royal Institute of Technology, 2023.

- [52] A. Brogliato, "Investigation of the impact of surface roughness induced by additive manufacturing on local heat transfer characteristics," Master's thesis, Politecnico di Torino, 2024.
- [53] P. Lehmann, "Investigation of the local heat transfer characteristics on additively manufactured surfaces using infrared thermography," Master's thesis, Technical University of Munich, 2023.
- [54] D. E. Metzger and D. E. Larson, "Use of melting point surface coatings for local convection heat transfer measurements in rectangular channel flows with 90-deg turns," *J. Heat Transfer*, vol. 108, pp. 48–54, Feb. 1986.
- [55] H. J. S. Byoung Jae Kim, "A further assessment of interpolation schemes for window deformation in piv," *Experiments in Fluids*, vol. 43, no. 5, pp. 763–780, 2007.
- [56] R. J. Moffat, "Describing the uncertainties in experimental results," *Exp. Therm. Fluid Sci.*, vol. 1, pp. 3–17, Jan. 1988.
- [57] H. W. Coleman and W. G. Steele, *Experimentation, Validation, and Uncertainty Analysis for Engineers*. Hoboken, New Jersey: John Wiley & Sons, Inc., 2018.
- [58] P. Bardet, M. André, and D. Neal, "Systematic timing errors in laser-based transit-time velocimetry," <https://resolver.tudelft.nl/uuid:93f94a5a-d3d3-40d6-ba27-0b0f8e7e0425>, 2013.
- [59] L. Lasers, *Nano PIV Series User Manual*.
- [60] H. W. Coleman and W. G. Steele, *Experimentation, validation, and uncertainty analysis for engineers*. John Wiley & Sons, 2018.
- [61] A. A. C. dos Santos, M. Childs, T. D. Nguyen, and Y. Hassan, "Convergence study and uncertainty quantification of average and statistical piv measurements in a matched refractive index 5×5 rod bundle with mixing vane spacer grid," *Experimental Thermal and Fluid Science*, vol. 102, pp. 215–231, 2019.
- [62] R. Mei, "Velocity fidelity of flow tracer particles," *Experiments in fluids*, vol. 22, no. 1, pp. 1–13, 1996.
- [63] M. Raffel, C. E. Willert, F. Scarano, C. J. Kähler, S. T. Wereley, and J. Kompenhans, *Particle image velocimetry: a practical guide*. Springer, 2018.
- [64] J. M. Acosta-Cuevas, M. A. García-Ramírez, G. Hinojosa-Ventura, Á. J. Martínez-Gómez, V. H. Pérez-Luna, and O. González-Reynoso, "Surface roughness analysis of microchannels featuring microfluidic devices fabricated by three different materials and methods," *Coatings*, vol. 13, p. 1676, Sept. 2023.
- [65] S. Ali, J. Faraj, and M. Khaled, "A correlation for u-value for laminar and turbulent flows in concentric tube heat exchangers," *International Journal of Thermofluids*, vol. 23, p. 100797, Aug. 2024.
- [66] P. Dutta, S. K. Saha, N. Nandi, and N. Pal, "Numerical study on flow separation in 90° pipe bend under high reynolds number by $k - \varepsilon$ modelling," *Engineering Science and Technology, an International Journal*, vol. 19, pp. 904–910, 2016.
- [67] L. Cattafesta, C. Bahr, and J. Mathew, *Fundamentals of Wind-Tunnel Design*. Chichester, UK: John Wiley & Sons, Ltd, Dec. 2010.
- [68] J. B. Barlow, W. H. Rae, and A. Pope, *Low-Speed Wind Tunnel Testing*. John Wiley & Sons, 3rd ed., 1999.
- [69] R. D. Mehta and P. M. D. Bradshaw, "Design rules for small low speed wind tunnels," *The Aeronautical Journal (1968)*, vol. 83, pp. 443 – 453, 1979.
- [70] C. Qi, F. Jiang, and S. Yang, "Advanced honeycomb designs for improving mechanical properties: A review," *Compos. B Eng.*, vol. 227, p. 109393, Dec. 2021.
- [71] R. D. Moser, J. Kim, and N. N. Mansour, "Direct numerical simulation of turbulent channel flow up to $Re\tau=590$," *Phys. Fluids (1994)*, vol. 11, pp. 943–945, Apr. 1999.
- [72] F. H. Clauser, "The turbulent boundary layer," *Advances in Applied Mechanics*, vol. 4, pp. 1–51, 1956.
- [73] E.-S. Zanoun, F. Durst, and H. Nagib, "Evaluating the law of the wall in two-dimensional fully developed turbulent channel flows," *Phys. Fluids (1994)*, vol. 15, pp. 3079–3089, Oct. 2003.

- [74] R. J. Boyle and M. Stripf, “Simplified approach to predicting rough surface transition,” *J. Turbomach. Trans. ASME*, vol. 131, p. 041020, Oct. 2009.
- [75] P. M. Ligrani and R. J. Moffat, “Structure of transitionally rough and fully rough turbulent boundary layers,” *J. Fluid Mech.*, vol. 162, p. 69, Jan. 1986.
- [76] L. Djenidi, R. A. Antonia, and F. Anselmet, “LDA measurements in a turbulent boundary layer over a d-type rough wall,” *Exp. Fluids*, vol. 16, pp. 323–329, Apr. 1994.
- [77] S. Leonardi, P. Orlandi, L. Djenidi, and R. A. Antonia, “Structure of turbulent channel flow with square bars on one wall,” *Int. J. Heat Fluid Flow*, vol. 25, pp. 384–392, June 2004.
- [78] J. Jiménez, “Turbulent flows over rough walls,” *Annu. Rev. Fluid Mech.*, vol. 36, pp. 173–196, Jan. 2004.

8. List of symbols

8.1. Latin symbols

A	$[m^2]$	heat transfer area at the generic location inside the domain
a	$[m]$	tracer particle radius
A_0	$[m^2]$	reference particle area
$Al1$	$[-]$	Aluminium 1
$Al2$	$[-]$	Aluminium 2
C	$[-]$	proportionality constant
C_1	$[-]$	first integration constant
C_2	$[-]$	second integration constant
C_F	$[-]$	Friction coefficient
C_H	$[-]$	Heat transfer coefficient
C_{max}	$[m]$	primary peak height of the cross correlation plane
c_p	$[J \cdot kg^{-1} K^{-1}]$	specific heat capacity at constant pressure
C_f	$[-]$	friction coefficient Clauser Chart method
C_s	$[-]$	cross-correlation coefficient
C_u	$[-]$	cross-correlation coefficient for u component of velocity
C_v	$[-]$	cross-correlation coefficient for v component of velocity
D	$[-]$	characteristic length of the wind tunnel
d_τ	$[m]$	resulting particle's diameter
d_{diff}	$[m]$	particle image's diffracted diameter
d_{geom}	$[m]$	particle image's diameter
d_{honey}	$[m]$	hydraulic diameter of the honeycomb cell
D_{honey}	$[m]$	hydraulic diameter of the honeycomb structure
d_i	$[m]$	image distance
d_m	$[m]$	minimum focus distance
d_o	$[m]$	object distance
d_p	$[m]$	tracer particle diameter
d_p	$[m]$	particle's diameter in reality
E	$[W \cdot m^{-2}]$	emissive power
E_λ	$[W \cdot m^{-3}]$	Radiation intensity of a real body
$E_{\lambda b}$	$[W \cdot m^{-3}]$	Radiation intensity of a blackbody
E_b	$[W \cdot m^{-2}]$	blackbody emissive power
f	$[-]$	Friction factor
$f\#$	$[-]$	f-stop
F_b	$[N]$	buoyancy force
F_i	$[N]$	inertia force
F_{ik}	$[-]$	view factor under which surface \mathbf{i} sees surface \mathbf{k}

F_{ki}	$[-]$	view factor unde which surface \mathbf{k} sees surface \mathbf{i}
F_v	$[N]$	viscous force
f_{eq}	$[m]$	equivalent focal length
$F_{S \rightarrow T}$	$[-]$	Transformation from radiometric signal to temperature
$F_{T \rightarrow S}$	$[-]$	Transformation from temperature to radiometric signal
f_1/f_2	$[m]$	Focal length
G	$[W \cdot m^{-3}]$	power generation per unit volume
g	$[m \cdot s^{-2}]$	gravity acceleration
Gr	$[-]$	Grashoff number
H	$[m]$	height
h	$[W \cdot m^{-2} \cdot K^{-1}]$	heat transfer coefficient
h_{SC}	$[m]$	height of the honeycomb structure
H_w	$[m]$	height of the interrogation window
I	$[-]$	turbulence intensity
$In939$	$[-]$	Inconel939
J	$[W \cdot m^{-2}]$	radiosity
J_0	$[0]$	intensity of the reference particle
J_i	$[0]$	intensity of the particle i
k	$[W \cdot m^{-1} \cdot K^{-1}]$	thermal conductivity
k	$[m]$	Roughness height
k^+	$[-]$	roughness Reynolds number
k_{rough}^+	$[-]$	roughness Reynolds number limit for rough
k_{smooth}^+	$[-]$	roughness Reynolds number limit for smooth
k_s	$[m]$	equivalent sand-grain roughness
Km	$[-]$	probe flow rate constant
ℓ	$[m]$	turbulent length scale
L	$[m]$	characteristic length
l_{ghoney}	$[m]$	external honeycomb cell length
l_{honey}	$[m]$	honeycomb cell length
L_c	$[m]$	characteristic length
L_{SC}	$[m]$	length of the honeycomb structure
ℓ_m	$[m]$	Prandtl's mixing length scale
\dot{m}	$[g \cdot s^{-1}]$	mass flow rate
m	$[-]$	exponent
m	$[-]$	exponent of modified power law
M	$[-]$	image magnification
$M(\cdot)$	$[-]$	order of magnitude
n	$[-]$	outward normal vector
n	$[-]$	exponent of modified power law
\mathbf{n}_a	$[-]$	unit vector perpendicular to the heat transfer area
\mathbf{n}_r	$[-]$	unit vector along heading in the positive direction of the spatial coordinate
Nu	$[-]$	Nusselt number
\bar{P}	$[Pa]$	time-avaraged pressure
Pe	$[-]$	Peclet number
Pr	$[-]$	Prandtl number
\mathbf{q}	$[W \cdot m^{-2}]$	heat flux
Q	$[W]$	thermal power
$Q_{i \rightarrow k}$	$[W]$	fraction of the thermal power leaving surface i and reaching surface k
Q_i	$[W]$	thermal power leaving surface i
Q_{ik}	$[W]$	net power transferred between surface i and surface k
$Q_{k \rightarrow i}$	$[W]$	fraction of the thermal power leaving surface k and reaching surface i
Q_v	$[l/s]$	volume flow rate
r	$[m]$	spatial coordinate
R	$[K \cdot W^{-1}]$	thermal resistance

R_{cd}	$[K \cdot W^{-1}]$	conductive thermal resistance
R_{ct}	$[K \cdot W^{-1}]$	contact thermal resistance
R_{cv}	$[K \cdot W^{-1}]$	convective thermal resistance
$R_{g,ik}$	$[m^{-2}]$	geometrical resistance between surface i and surface k
R_{ku}	$[-]$	roughness heights Kurtosis
R_s	$[m^{-2}]$	surface resistance
R_{sk}	$[-]$	roughness heights skewness
R_a	$[\mu m]$	average absolute deviation from the mean line
R_q	$[\mu m]$	roughness heights standard deviation
R_z	$[\mu m]$	maximum peak to valley distance
Ra	$[-]$	Rayleigh number
Re	$[-]$	Reynolds number
Re_τ	$[-]$	friction Reynolds number
Re_L	$[-]$	Reynolds number depending on the length scale L in the flow direction
Re_y	$[-]$	Reynolds number at a y distance from the wall
Ri	$[-]$	Richardson number
S_Φ	$\left[\frac{\text{kg}}{\text{m}^3} \right]$	source term in the scalar transport equation for RANS
S_{Mx}	$\left[\frac{\text{kg}}{\text{m}^3 \cdot \text{s}^2} = \text{N/m}^3 \right]$	source term in x direction for RANS
S_{Mx}	$\left[\frac{\text{kg}}{\text{m}^3 \cdot \text{s}^2} = \text{N/m}^3 \right]$	source term in z direction for RANS
S_{My}	$\left[\frac{\text{kg}}{\text{m}^3 \cdot \text{s}^2} = \text{N/m}^3 \right]$	source term in y direction for RANS
s	$[m]$	domain thickness
S	$[-]$	Radiometric signal
s	$[-]$	Upscaling factor
S_μ	$[K]$	Sutherland costant
s_{honey}	$[m]$	honeycomb cell thickness
S_{Solid}	$[m^2]$	solid area of the honeycomb cell
S_{det}	$[-]$	Detected radiometric signal
S_{hex}	$[m^2]$	area of the hexagonal shape of the honeycomb
S_{hex}	$[m^2]$	area of the hexagonal shape of the honeycomb
S_k	$[-]$	Stokes number
St	$[-]$	Stanton number
T_∞	$[K]$	fluid temperature
T_s	$[K]$	surface temperature
T_b	$[K]$	Bulk temperature
T_w	$[K]$	Wall temperature
\bar{U}	$[ms^{-1}]$	time-avaraged velocity component x
\tilde{U}	$[ms^{-1}]$	density weighted velocity component x
U	$[m \cdot s^{-1}]$	Flow velocity
u	$[j \cdot m^{-1}]$	internal energy
u'	$[ms^{-1}]$	fluctuating velocity component x
u^+	$[-]$	velocity normalized using friction velocity
u_τ	$[m^2 s^{-1}]$	friction velocity
u_{rms}	$[m/s]$	rms value of the velocity u
u_{rpc}	$[m]$	uncertainty value calculated with RPC method
u_{scc}	$[m]$	uncertainty value calculated with SCC method
u_m	$[m \cdot s^{-1}]$	mean flow velocity
U_M	$[-]$	magnification uncertainty
\bar{V}	$[ms^{-1}]$	time-avaraged velocity component y
\tilde{V}	$[ms^{-1}]$	density weighted velocity component y
V	$[m^3]$	volume
v'	$[ms^{-1}]$	fluctuating velocity component y
v_{rms}	$[m/s]$	rms value of the velocity v
\bar{W}	$[ms^{-1}]$	time-avaraged velocity component z

\tilde{W}	$[ms^{-1}]$	density weighted velocity component z
W	$[m]$	width
w	$[m]$	Laser sheet waist
W	$[m/s]$	wind tunnel velocity
w'	$[ms^{-1}]$	fluctuating velocity component z
x	$[mm]$	Streamwise coordinate
$x_{fd,x}$	$[m]$	hydrodynamic entrance region
y^+	$[-]$	distance from the wall normalized using friction velocity
z_{ghoney}	$[-]$	solid sheet division of the honeycomb

8.2. Abbreviation

AM	Additive Manufacturing
BB	Blackbody
CAD	Computer-Aided Design
CCD	Charge-Coupled device
CCIR	Comité Consultatif International pour la Radio
CDF	Cumulative Density Function
CMOS	Complementary Metal-Oxide Semiconductor
DAS	Data Acquisition System
FFT	Fast Fourier Transform
FFT	Discrete Fourier Transform
FI	in-plane loss of correlation
FO	out-of-plane loss of correlation
FOV	field of view
FT	Fourier Transform
HGA	Harmonic Generation Assembly
HT	Heat Transfer
HTC	Heat Transfer Coefficient
I	interrogation window
IEA	International Energy Agency
IGT	Industrial Gas Turbines
IR	Infrared
IRW	Infrared Window
LBGT	Land-Based Gas Turbines
L-PBF	Laser Powder Bed Fusion
LUCi	Litron Universal Control interface
MCM	Monte Carlo Method
MI	Mutual Informargion
PDF	Probability Density Function
PIV	Particle Image velocimetry
PPR	Primary Peak Ratio
PWM	Pulse Width Modulation
QSSHT	Quasi Steady State Heat Transfer
RANS	Reynolds Averaged Navier Stokes
RIT	Rotor Inlet Temperature
ROI	Region Of Interest
RPC	Signal-to-Noise Ratio Correction Mode
S/N	signal to noise ratio
SCC	Rational Polynomial Coefficient
SEM	Scanning Electron Microscope
SLA	Stereolithography
SR	Surface Roughness
SRHT	Sourface Roughness Heat Transfer
STL	Standard Triangle Language
TBC	Thermal Barrier Coating
TIT	Turbine Inlet Temperature
TSM	Taylor Series Method

8.3. Greek symbols

α	$[m^2 \cdot s^{-1}]$	thermal diffusivity
β	$[K^{-1}]$	isobaric thermal expansion coefficient
β_h	$[-]$	porosity
$\Delta(\dots)$	$[-]$	absolute uncertainty of a quantity
δ	$[m]$	boundary layer thickness
$\delta(\dots)$	$[-]$	relative uncertainty of a quantity
δ	$[-]$	Kroneker delta
ϵ	$[-]$	emissivity
ϵ_λ	$[-]$	spectral emissivity
ϵ_{CS}	$[-]$	calibration source emissivity
ϵ_{paint}	$[-]$	paint emissivity
η_{th}	$[-]$	Efficiency of the cycle
γ	$[-]$	Specific heat ratio (c_p/c_v)
Γ_Φ	$[m^2 s^{-1}]$	Diffusion coefficient for the dissipation function
γ_h	$[-]$	solidity
κ	$[-]$	Von Kármán constant
λ	$[-]$	friction factor; wavelength
λ_s	$[m]$	smallest later wavelength
μ	$[kg \cdot m^{-1} \cdot s^{-1}]$	dynamic viscosity
ν	$[m^2 \cdot s^{-1}]$	kinematic viscosity (momentum diffusivity)
Φ	$[W \cdot m^{-3}]$	dissipation function
ϕ	$[-]$	cross-correlation function
$\bar{\rho}$	$[kg \cdot m^{-3}]$	time averaged density
ρ	$[kg \cdot m^{-3}]$	density
ϱ_{IRW}	$[-]$	reflectivity of the infrared window
ϱ_{paint}	$[-]$	reflectivity of the paint
ρ_f	$[kg \cdot m^{-3}]$	density fluid
ρ_p	$[kg \cdot m^{-3}]$	density seeding particles
ρ_s	$[kg \cdot m^{-3}]$	density of the rough elements
σ	$[W \cdot m^{-2} \cdot K^{-4}]$	Stephan Boltzman constant ($\sigma = 5.67 \cdot 10^{-8} W \cdot m^{-2} \cdot K^{-4}$)
τ	$[N \cdot m^{-2}]$	viscous stress
τ_{IRW}	$[-]$	transmissivity of the infrared window
τ_w	$[m^2 s^{-1}]$	wall shear stress
τ_{xx}	$[m^2 s^{-1}]$	normal Reynolds stress in the x coordinate
τ_{xy}	$[m^2 s^{-1}]$	shear Reynolds stress in the xy plane
τ_{xz}	$[m^2 s^{-1}]$	shear Reynolds stress in the xz plane
τ_{yy}	$[m^2 s^{-1}]$	normal Reynolds stress in the y coordinate
τ_{yz}	$[m^2 s^{-1}]$	shear Reynolds stress in the yz plane
τ_{zz}	$[m^2 s^{-1}]$	normal Reynolds stress in the z coordinate
τ_f	$[s]$	characteristic flow time scale
τ_p	$[s]$	particle time response

Abstract in lingua italiana

In questa tesi vengono esaminate le proprietà termiche e di flusso delle superfici prodotte in modo additivo tramite stampanti 3D, con particolare attenzione alla rugosità della superficie e al modo in cui essa influisce sulla fluidodinamica e sul trasferimento di calore nei canali di raffreddamento. Il lavoro si concentra sui metodi di fusione laser a letto di polvere, comunemente impiegati nella produzione di complessi condotti di raffreddamento per turbine a gas. Sebbene aumenti la libertà di progettazione, l'elevata rugosità superficiale di questi componenti genera alcune problematiche quali transizioni precoci dello strato limite e maggiori perdite di quantità di moto che compromettono le prestazioni termiche e aerodinamiche. Al fine di massimizzare l'efficienza del raffreddamento nelle applicazioni delle turbine a gas, questo lavoro indaga l'effetto della rugosità sul trasferimento di calore utilizzando apparati sperimentali che utilizzano la termografia a infrarossi e la tecnica Particle Image Velocimetry. Nell'ambito degli sforzi di Siemens Energy AB per fornire soluzioni energetiche sostenibili, i risultati contribuiscono a migliorare le procedure di produzione additiva e l'efficienza termica complessiva delle turbine a gas stazionarie.

Parole chiave: Produzione Additiva, Rugosità superficiale, Trasferimento di calore, Fluidodinamica, Turbine a Gas, Termografia a infrarossi, Particle Image Velocimetry, numero di Nusselt, Profilo di Velocità, Strato Limite

Acknowledgements

We would like to express our gratitude to everyone who has supported us during our months at Siemens Energy, in Finspång.

We want to start by thanking to our manager and mentor, Alessio Bonaldo, for his constant support and direction.

For his help in the lab and throughout the experimental part of our study, we are also incredibly grateful to Mats Kinell. His practical assistance and technical expertise have been essential to the accomplishment of our research.

Finally, we want to express our sincere gratitude to Javier Soriano Lluch for his generosity and invaluable assistance during our journey. His encouragement and support during difficult moments gave us the willpower to keep going.



POLITECNICO
MILANO 1863